Memristive Ag_2S Synapses: towards Artificial Neural Networks

Catarina Dias

Thesis submitted to the
Faculty of Sciences of the University of Porto
in partial fulfillment of the requirements
for the degree of
Master in Physics Engineering

Supervisor: Prof. João Oliveira Ventura
co-Supervisor: Prof. João Pedro Araújo

Department of Physics and Astronomy
Faculty of Sciences of the University of Porto
September 2013

To my mother, grandparents and uncle.

Acknowledgments

First and above all, I would like to thank my supervisor, Professor João Oliveira Ventura for his dedication, motivation and patience. I am truly thankful to him, for believing in my work more than me and for providing me this opportunity. Without him none of this would be possible. I have learned enormously and I look forward to continue to improve with him.

Thanks to my co-supervisor, Professor João Pedro Araújo, for accepting me as his student and for his early morning sympathy.

To Gonçalo Pimentel for all the help with software that made my work easier and to Luís Guerra for his detailed overview of my thesis. But mainly, for their patience having me as a partner. I could not see better persons to start my investigations with.

A special acknowledgment for Paulo Aguiar, of CMUP, for his share of knowledge and interest demonstrated in the work performed.

To members of IFIMUP-IN for the sympathy, interest and great work environment. A special thanks (in order of appearance) to Mariana Proença for the time spent with electrodeposition, to Arlete Apolinário for her lunch hours passed in SEM, to Francisco Carpinteiro for his wide knowledge and support and to Professor Joaquim Agostinho Moreira for his interest in my work.

From CEMUP, also to Professor Carlos Sá for his critical thinking and, sincerely, to Rui Rocha for his great professionalism and patience during so many EDS hours.

To the INESC-MN for the collaboration and specially to Dr. Susana Freitas for her availability, suggestions and helpful share of knowledge, and to João Pereira for the guidance.

I would also like to thank for the opportunity to benefit from an ANICT masters grant for the development of my masters thesis in "Memristive Ag_2S Synapses: towards Artificial Neural Networks".

In this five years of journey, thanks to my colleagues for the admiration and confidence. To my friends an apology for my crankiness and absence this last year. A special word for my other half for all the serenity, comprehension and support, and for suffering stay up late, nights, weekends and holidays in the faculty.

To my family, they are the reason I am here.

Thank you all.

Associação Nacional de Investigadores em Ciência e Tecnologia

Resumo

As capacidades de processamento dos computadores actuais estão a tornar-se numa limitação na resposta às necessidades tecnológicas modernas. Assim, abordagens em alternativa à arquitectura computacional de von Neumann são imperativas, sendo o funcionamento e estrutura do cérebro modelos verdadeiramente apelativos. Os memristors são caracterizados por uma relação não linear entre o histórico de corrente e a tensão e foi demonstrado que apresentam propriedades semelhantes às das sinapses biológicas. Aqui discutimos o uso de dispositivos memresistivos baseados em estruturas metal-isolador-metal em redes neuronais capazes de simular as capacidades de aprendizagem e de adaptação existentes nos cérebros humanos.

A primeira parte deste trabalho (Capítulo 3) passou pela fabricação das amostras através de diversos métodos (deposiçao por feixe iónico, *annealing* térmico, eletrodeposição e submersão em soluções) no sentido de optimizar os processos e escolher o mais apropriado. Fomos capazes de controlar a estequiometria do Ag_2S e de caracterizar as amostras usando técnicas como difracção por raio-X (XRD), espectroscopia de Raman, espectroscopia de infravermelhos (FTIR), espectroscopia de energia dispersiva (EDS) e espectroscopia por varrimento electrões (SEM), todas descritas no Capítulo 2, bem como efectuar medidas de resistividade eléctrica.

Medidas de transporte eléctrico foram realizadas nas amostras obtidas (Capítulo 4). O comportameno esperado de mudança de resistência associado ao sistema modelo de Ag_2S foi obtido e diferentes comportamentos de mudança de resistência foram observados nos dispositivos: curvas memresistivas do tipo I e II, comportamentos bipolar e unipolar, para os quais tanto o processo de escrever e como o de apagar foram observados para tensões negativas ou positivas em diferentes ciclos, e mudança resistiva complementar. Além disso, a dependência da resistência eléctrica no tempo foi estudada, estudos estatísticos foram realizados e ainda foram observadas modificações dependentes da actividade. Estes efeitos foram atribuídos à formação de um filamento metálico no interior da camada dieléctrica devido a electromigração.

Abstract

Present computer processing capabilities are becoming a restriction to meet modern technological needs. Therefore, approaches beyond the von Neumann computational architecture are imperative and the brain's operation and structure are truly attractive models. Memristors are characterized by a nonlinear relationship between current history and voltage and were shown to present properties resembling those of biological synapses. Here we discuss the use of metal-insulator-metal-based memristive devices in neural networks capable of simulating the learning and adaptation features present in human brains.

The first part of this work (Chapter 3) consisted in the fabrication of the samples using diversified methods (ion beam deposition, thermal annealing, electrodeposition and dipping in solutions) in order to optimize the processes and select the appropriate one. We were able to control the Ag_2S stoichiometry and to characterize the samples using techniques such as X-ray Diffraction (XRD), Raman Spectroscopy, Fourier Transform Infrared Spectroscopy (FTIR), Energy Dispersive Spectroscopy (EDS) and Scanning Electron Microscopy (SEM), all described in Chapter 2, as well as electrical resistivity measurements.

Transport measurements were then performed in the obtained samples (Chapter 4). The expected resistive switching behavior associated with the Ag_2S model system was obtained and different switching behaviors were observed in the devices: memristive types I and II curves, bipolar and unipolar behavior, in which both set and reset were seen at negative or positive voltages for different cycles, and complementary resistive switching. Furthermore, dependence of the electrical resistance with time was studied, statistical studies were performed and activity-dependent modifications were also observed. These effects were attributed to the formation of a metallic filament due to electromigration inside the dielectric layer.

Contents

List of Tables

List of Figures

Nomenclature

Ag	Silver
Ag2S	Silver sulfide
Al	Aluminium
ANN	Artificial neural network
ATR	Attenuated total reflectance
Au	Gold
bcc	Body-centered cubic
BSE	Backscattered electrons
CF	Conductive filament
CMOS	Complementary metal oxide semiconductor
DC	Direct current
DMSO	Dimethyl sulfoxide
EDS	Energy dispersive spectroscopy
EPVC	Electrochemical photovoltaic
FTIR	Fourier transform infrared spectroscopy
FWHM	Full width at half maximum
HRS	High resistive state
IBD	Ion beam deposition
IR	Infrared
ISI	Interspike interval
LRS	Low resistive state
LTD	Long-term depression
LTM	Long-term memory
LTP	Long-term potentiation
MIEC	Mixed ionic-electronic conductor
MIM	Metal-insulator-metal
NDR	Negative differential resistance
ReRAM	Resistive random access memory
RS	Resistive switching

S	Sulfur
SCLC	Space-charge-limited conduction
SE	Secondary electrons
SEM	Scanning electron microscopy
SM	Sensory memory
SPICE	Simulation program with integrated circuit emphasis
STDP	Spike timing dependent plasticity
STM	Short-term memory
TEM	Transmission electron microscopy
VLSI	Very large scale integration
W	Tungsten
XPS	X-ray photoelectron spectroscopy
XRD	X-ray diffraction

'HAPPY THESISMAS'

Chapter 1
Introduction

The extraordinary rise in processing power, speed and storage capacity of computers is coming to a stall. There is thus an enormous opportunity to completely rethink the foundations of the present information age and open new paths into alternative forms of computation. In particular, computational architectures departing from the present von Neumann paradigm are being intensively sought after. For example, *memory* and *adaptation* are essential building blocks in learning and decision-making in biological systems [13]. Von Neumann systems rely on a deterministic approach in which learning and adaptation to new environments cannot be captured, whereas biological systems rely on an indeterministic approach with massive parallelism of simple processing units (neurons). This results in huge power efficiency, adaptation and resilience to unit failure [14, 5].

Artificial systems in which processing and memory functions are located in the same level have been a long scientific dream, since they promise large improvements in performance along with the opportunity to design and build brain-like systems. This has moved a step closer following recent investigations of so-called memristive devices, which are two-terminal devices characterized by nonlinear relationships between histories of current and voltage [23]. Their dynamics and small size have suggested their use as synapses and have inspired the neuromorphic community to explore the potential for building low-power intelligent machines [24].

1.1 Learning and Adaptation in Biological Systems

1.1.1 Brain Architecture and Operation

Two fundamental units of the human brain, the neuron and the synapse (Fig. 1), play essential roles in learning and in the formation of memory. Neurons are electrically excitable cells and are able to respond to stimuli, to conduct impulses and to link to other neurons of the neural network. Synapses are specialized junctions in-between neurons that allow the rapid transmission of electrical and chemical signals so that neurons can communicate with each other [1]. Thus, they are responsible for providing a neuron with a converted input that is proportional to the importance of the output signal from another neuron. When an action potential generated by a neuron reaches a pre-synaptic terminal, a cascade of events leads to the release of neurotransmitters that give rise to a flow of ionic currents into or out of the post-synaptic neuron.

Figure 1(b) illustrates two neurons connected by a synapse. The pre-synaptic neuron sends a pre-synaptic spike $V_{mem-pre}$ through one of its axons to the synaptic junction, while the post-synaptic neuron receives a post-synaptic spike $V_{mem-pos}$. Neural spikes are voltages from the outside of the cellular membrane V_{pre+}/V_{pos+} with respect to the inside V_{pre-}/V_{pos-} [Fig. 1(c)]. Large spikes (hundreds of mV) make selective membrane channels to open (or close) allowing for ionic substances to flow (or not) through the membrane. Neurotransmitters released from pre- contribute to a change in the post-synaptic membrane's conductivity [3].

1.1.2 Learning and Memory

Learning and memory in human brains is the capability to gain new information, store it and be able to recall it. It is now generally accepted that information is stored in the synaptic strength, with learning being accomplished by modifying (either increasing or decreasing) the strength of the synapses [25]. Such synaptic plasticity makes possible to store information and to react to inputs based on past knowledge [26].

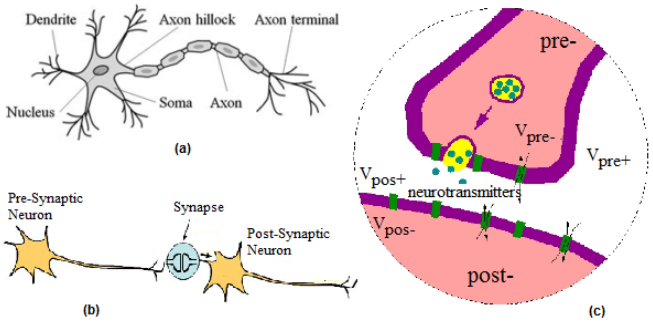

$$V_{mem-pre} = V_{pre+} - V_{pre-}$$
$$V_{mem-pos} = V_{pos+} - V_{pos-}$$

Figure 1: (a) Structure of a biological neuron (taken from Ref. [1]). (b) Simplified diagram of a biological synapse interconnecting two neurons (taken from Ref. [2]). (c) Detail of a synaptic junction (adapted from Ref. [3]).

Hebbian Learning. Objects once experienced together tend to become associated, so that when any one of them is thought of, the others are likely to be thought of also, in the same order of coexistence as before [25]. One of the most famous experiments related to associative memory is Pavlov's experiment whereby salivation of a dog is first set by the sight of food. Then, if the sight of food is accompanied by a sound (bell) over a certain period of time, the dog learns to associate the sound with the food, and salivation can be triggered by the sound alone [24]. In 1949, D. Hebb addressed this learning postulate at the neural level: "neurons that fire together, wire together" [3]. Thus, when two connected neurons are active at the same time, the weight of the connecting synapse increases to reinforce that correlation. This learning rule is not complete, since it provides a rule for increasing synaptic weight but not for decreasing it and does not specify the effective time window between pre- and post-synaptic activity that will result in potentiation.

Spike Timing Dependent Plasticity. Spike timing dependent plasticity (STDP) is an experimentally verified biological phenomenon in which the precise timing of spikes affects the sign and magnitude of changes in synaptic strength. STDP can be divided into long-term potentiation (LTP) and long-term depression (LTD). In the former, synapses increase their efficiency as a pre-neuron is activated momentarily before a post-neuron, while in the latter synapses decrease their efficiency as a post-neuron is activated momentarily before a pre-neuron [27]. As depicted in Fig. 2, the interspike interval (ISI) between action potentials in the pre- and post-synaptic cells modulates STDP. The smaller the timing between pre- and post-synaptic spikes, the larger plasticity change is induced in both LTP and LTD. On the other hand, longer intervals (above 50 ms) produce little or no change in synaptic strength [26, 4] The relative synaptic conductance change $\Delta G = (G_{after} - G_{before})/G_{before}$, where G_{before} (G_{after}) is the conductance before (after) the pre- and post-spike pair, has a range of $[0, +\infty[$ for potentiation and $[-1, 0]$ for depression [5, 26]. The importance of STDP relies on the fact that it addresses both questions left open by Hebb: it establishes a critical time window in which pre- and post-synaptic activity must occur to produce long-term changes in synaptic strength, and it provides a simple learning rule that decreases synaptic strength.

Short- and Long-Term Potentiation. Memory is believed to occur in the human brain as a result of two types of synaptic plasticity: short-term potentiation (STP) and long-term potentiation (LTP). Here, synaptic plasticity refers to changes that occur in the organization of the brain as a result of experience. STP is achieved through the temporal enhancement of a synaptic connection, which then quickly decays to its initial state. However, repeated stimulation can cause a permanent change in the connection to reach LTP and shorter repetition intervals enable efficient LTP formation from fewer stimuli [25, 9, 28].

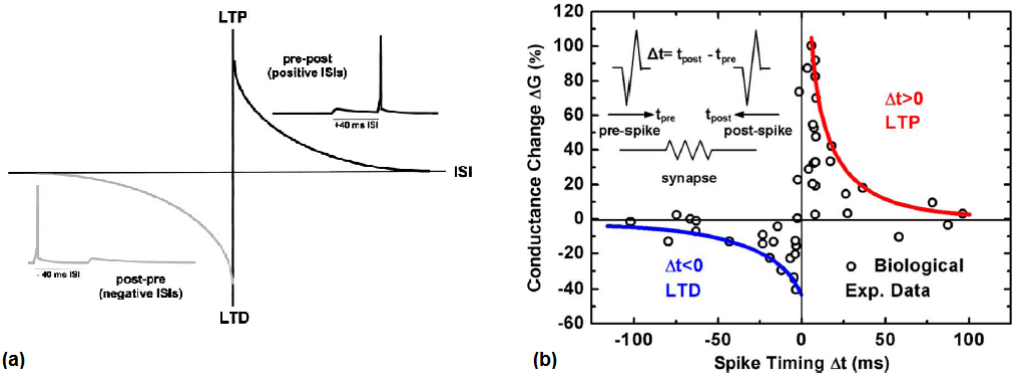

Figure 2: (a) STDP schematics. Maximal plasticity is produced by short negative or positive interspike intervals. Representative traces from the models of pairings at negative (gray inset) and positive ISIs (black inset) (taken from Ref. [4]). (b) Experimental STDP data of a biological synapse (taken from Ref. [5]).

1.2 Artificial Neural Networks

Several attempts have been made to mimic the biological learning rules in artificial synapses and to construct artificial networks capable of performing complex functions. In most neural network models, synapses are dynamical two-terminal entities that connect a pre- (source) to a post-synaptic neuron (sink). The source emits an analog signal that is modified by a synaptic transfer function and delivered to the sink. The sink has a state variable that partially depends upon the history of incoming signals received from synapses that drive it. This variable, along with the source signal, determine the evolution of the synaptic state variable.

A radical approach in the construction of artificial neural networks (ANNs) is to use analogue very large scale integration (VLSI) to implement directly in silicon the required computational model of a neural system. In neuromorphic implementations, the key challenge is to design circuits with large time constants while keeping the neuronal structure simple, occupying small silicon area and using only one electronic device as an artificial synapse. However, the silicon area occupied by the synaptic circuit can vary significantly, as it depends on the choice of layout design solutions and more conservative solutions use large number of transistors.

Implementing the large connectivity of the brain with transistors on a single chip is a huge challenge, since a large number of transistors is needed [1, 27]. Therefore, the electronic conventional implementation is not practical at all and a simple resistive switching device to emulate synaptic functions is required [27]. Such device must have a continuous resistance whose evolution depends on the history of the input signals, mimicking the gradual potentiation (or depression) of biological synapses [26, 27]. As we will see, the memristor displays such properties, making it the most promising candidate to be used in scalable neural networks.

1.3 Memristors and Memristive Systems

In 1971, Chua theoretically introduced the concept of the memristor (abbreviation of memory-resistor) as the fourth basic circuit element alongside the resistor, the capacitor, and the inductor [29]. Chua postulated that there are four fundamental circuit variables (voltage V, current I, charge q and magnetic flux φ) which can be combined two at a time in six possible ways, corresponding to Eqs. (1)-(6) [see Fig. 3(a)]:

$$Definition\,of\,current:\ dq = Idt \quad (1)$$

$$Faraday's\,law:\ d\varphi = Vdt \quad (2)$$

$$Resistor:\ dV = RdI \quad (3)$$

$$Capacitor:\ dq = CdV \quad (4)$$

$$Inductor:\ d\varphi = LdI \quad (5)$$

$$Memristor:\ d\varphi = M(q)dq\,, \quad (6)$$

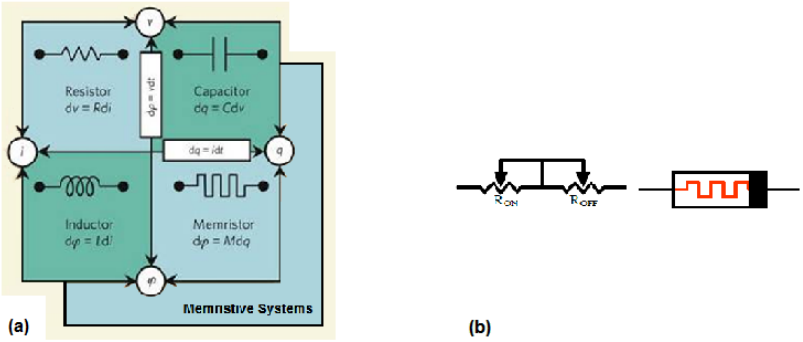

Figure 3: (a) The four electric variables (q, φ, i, v) can be combined in six possible ways: two of them correspond to fundamental relationships, and four correspond to the canonical two-terminal passive circuit elements (taken from Ref. [6]). (b) Equivalent circuit (left; R_{ON} and R_{OFF} are the minimum and the maximum memristance) and symbol of the memristor (right; polarity indicated by a black bar - the memristance is decreased/increased when current flows from the left/right to the right/left).

where R, C, L, M and t are resistance, capacitance, inductance, memristance and time, respectively. In short, there exists the resistor, in the linear case, and the memristor to relate flux and charge.

The experimental realization of a memristor device was only recently achieved, with the pioneering work of Strukov *et al.* [6]. They showed that a sinusoidal voltage produces a pinched-hysteretic I(V) characteristic in $Pt/TiO_2/Pt$ nanostructures due to the motion of charged dopants. Since its experimental realization, the memristor has become one of the most promising candidates for the post-complementary metal oxide semiconductor (CMOS) era. In 1976, Kang and Chua [30] further extended their previous analysis to *memristive systems* and showed that diverse groups such as thermistors, Josephson junctions and ionic transport in neurons are special cases of memristive systems [30, 31].

1.3.1 Theory

An ideal current-controlled *memristor* [equivalent circuit and symbol shown in Fig. 3(b)] is defined by:

$$V(t) = R_M(q(t))\, I(t) = R_M\left[\int_{-\infty}^{t} dt' I(t')\right] I(t), \tag{7}$$

where the proportionality function, $R_M(q(t))$, has the dimensions of a resistance (memristance) and $q(t)$ is the charge that flows in the system. If $R_M(q(t))$ is independent of time, Eq. (7) reduces to the Ohmic form. An ideal voltage-controlled memristor is defined by the relation [32]:

$$V(t) = R_M\left[\int_{-\infty}^{t} dt' V(t')\right] I(t). \tag{8}$$

The memristor belongs to a more complex class of dynamical systems [23, 32]. It was then generalized that the state variable that determines the state of the system at a given time could be other than the charge and then a *memristive system* is defined instead. So, let one define x as the set of n possible state variables (related with a particular device) with the time evolution:

$$\frac{dx}{dt} = f(x, I, t), \tag{9}$$

where $f(x, I, t)$ is a continuous n-dimensional vector function. As the state variable of a memristor is not a bias but an integration of the total current, the memristor can also work as a multi-state memory [9]. The

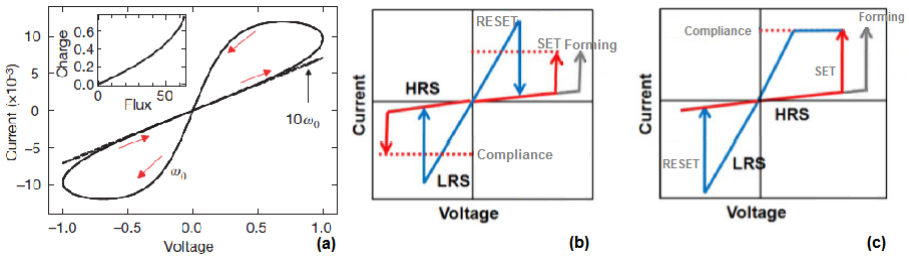

Figure 4: (a) I(V) curves and hysteresis collapse with a ten fold increase in sweep frequency (taken from Ref. [6]). I(V) curves with forming for (b) unipolar and (c) bipolar switching (adapted from Ref. [7]).

functions defining a current-controlled and a voltage-controlled *memristive system* are then:

$$V(t) = R_M(x, I, t)\, I(t)\,, \qquad (10) \qquad\qquad V(t) = R_M(x, V, t)\, I(t)\,. \qquad (11)$$

Hysteretic Loop. The response of a memristive system to a periodic current (or voltage) input is a "pinched hysteretic loop" [Fig. 4(a)], which is one of the most important properties of these systems, as hysteresis is a typical signature of memory devices. With respect to the periodic stimulus, for very high frequencies, a memristive system operates as a typically linear resistor since the state variable is not able to follow the stimulus in each oscillation, while for low frequencies it operates as a non-linear resistor, in which the state variable is given enough time to adjust. A variety of I(V) characteristics based on the frequency [31] and depending on the voltage time history are possible [23].

1.3.2 Metal-Insulator-Metal Memristors

The simplest nanostructure displaying resistive switching (RS) and memristive properties is the metal-insulator-metal (MIM) junction. A MIM device is simply an insulator material sandwiched between electrochemically active and/or inert metallic electrodes in a capacitor structure [7, 12, 33, 8]. The recent large interest in these structures aims at a new class of memories called resistive random access memories (ReRAMs), since their switching is fast, non-volatile and can result in large ON/OFF ratio. Furthermore, MIM structures are the only where both unipolar and bipolar switching (defined below) can be observed, depending on the dielectric/electrode interfacial properties [7]. Interestingly, Choi *et al.* also demonstrated that a single MIM structure successfully stores the biological synaptic weight variations without any external storage node or circuit [26].

1.3.2.1 Resistive Switching

The most appealing property in *memristive systems* (for memory applications) is their RS between a low resistive state (LRS; R_{ON}) and a high resistive state (HRS; R_{OFF}), upon the application of an external voltage or current. The HRS to LRS switching is called set (or write), while the reverse is called reset [or erase; Figs. 4(b) and (c)] [34]. For some devices based on filamentary switching (see below), an electroforming step is needed before the first set. When the switching direction does not depend on the polarity of the applied bias, but just on its amplitude, the switching is called unipolar. Thus, set and reset can occur for the same polarity [Fig. 4(b)]. When it depends on the polarity, the switching is called bipolar and reset can only occur at the reverse polarity of the set process [Fig. 4(c)] [7]. V/I sweeps are frequently used for the identification of switching behavior, whereas pulses are useful for the quantitative investigation of switching kinetics. The state can be retrieved by measuring the electrical current when a small read voltage is applied [35].

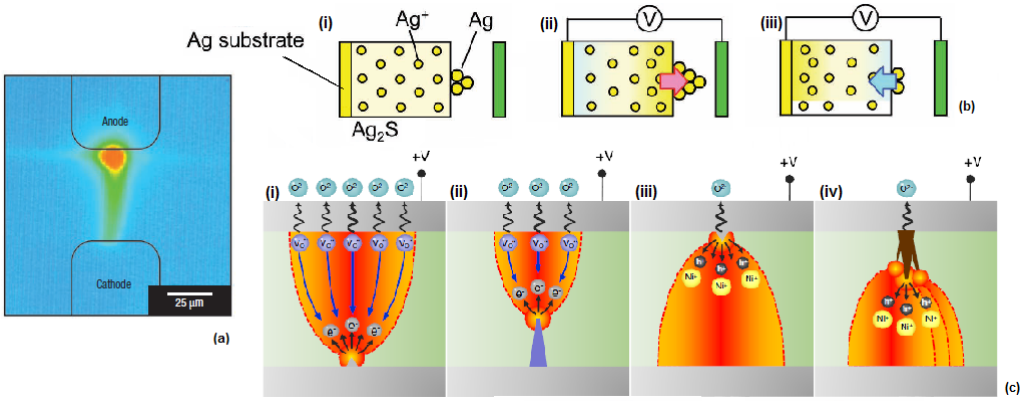

Figure 5: (a) Infrared thermal micrograph of a planar Cr-doped $SrTiO_3$ single-crystal (Colors represent room and elevated temperatures; taken from Ref. [8]). (b) The mechanisms of Ag nanowire growth and shrinkage. (i) Without any external bias, (ii) Positive bias at Ag_2S causes Ag^+ diffusion towards the surface, (iii) Negative bias causes Ag^+diffusion towards the bottom, re-dissolving into it (taken from Ref. [9]). (c) Schematic of a detailed CF formation process in TiO_2. (i) Oxygen vacancies are dragged to an electron injection area; (ii) Stable nuclei facilitates CF growth. (iii) and (iv) show the subsequent thermo-chemical reactions (taken from Ref. [10]).

Electroforming. An electroforming step is often a pre-requisite for RS in these type of devices. Electroforming denotes an electrochemical process for metallic structures formation during which metal ions or particles are injected into the dielectric and cause semi-permanent structural modifications inside the otherwise insulating medium [11]. As soon as one conductive filament is formed, the resistance of the structure is dramatically reduced, which results in the drop of both the current and electrical field across the dielectric. This prevents the formation of further filaments, self-limiting the process ("winner-take-all procedure") [8, 34, 10]. The associated high current overshoot can cause significant local self-heating (reaching several hundred kelvin) and dielectric breakdown effects. The current must then be limited by a current compliance [35].

Filamentary Switching. A conducting filament (CF) that acts as a circuit switch between two electrodes is believed to be responsible for most RS phenomena. Such CF formation occurs during the electroforming and set processes and can be described by a nucleation and growth process. The filament initial growth is mostly an electric-field-driven phenomenon and the power dissipation by the sudden current flow causes heat generation and makes the filament stronger. The applied voltage imparts directionality to the CF nucleation and growth [10]. The distribution of the winning filaments is non-uniform over the pad area, so the LRS has only a slight dependency on the cell area, whereas the HRS increases as the inverse of the cell area, roughly following Ohm's law. Thus the HRS/LRS ratio benefits from device scaling [7, 8]. Waser *et al.* confirmed the confinement of the current path and showed a "hot spot" near the electrode, where the CF touches the anode [Fig. 5(a)]. Most of the observed filamentary switching-driven phenomena are related with ionic motion [8]. Ionic RS effects involve the transport and electrochemical reactions of cations or anions [34]. Note that in many oxides, especially transition metal oxides, oxygen ions or vacancies are much less mobile than cations, since, owing to their relatively large size, their diffusion coefficient and corresponding mobility is very low, and memristive effects are appreciable only at the nanoscale [31, 34, 10].

Cation migration. The resistance change in cation-based devices is due to the electrochemical formation and dissolution of metallic filaments [34]. In this class, the set process involves the following steps: (1) anodic dissolution of the electrochemically active electrode (such as Ag or Cu; surface oxidation of the

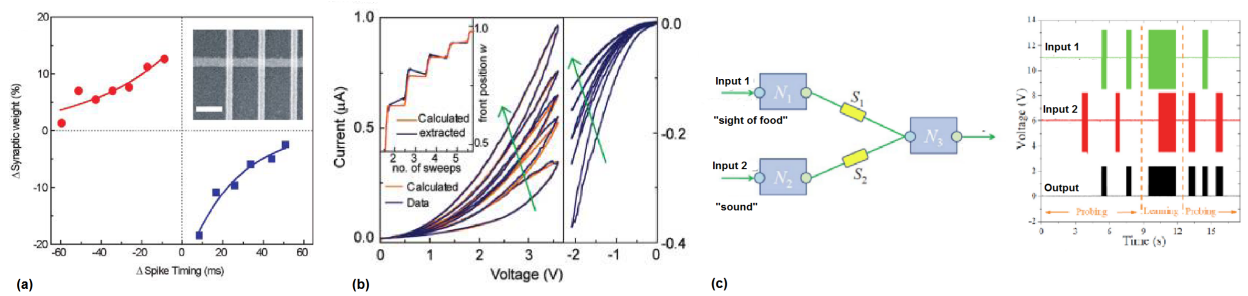

Figure 6: (a) Memristor synaptic weight versus the relative timing of the neuron spikes. Inset: SEM image of the crossbar array (scale: 300 nm). (b) Measured (blue) and calculated (orange) I(V) characteristics (taken from Ref. [11]). (c) Two memristive synapses (S_1 and S_2), two input (N_1 and N_2), and one output (N_3) neurons. In the initial probing phase, output only fires when input 1 fires. In the learning phase, S_2 is adjusted such that, in the probing phase, the output fires when either input 1 or input 2 fires (taken from Ref. [12]).

electrochemically active electrode metal): $M \rightarrow M^{z+} + ze^-$; (2) drift of the cations M^{z+} across the solid electrolyte (ion-conducting layer) under the applied electrical field; (3) cathodic reaction at the inert electrode (e.g., Au or Pt) by the nucleation and growth of metallic electrodeposits: $M^{z+} + ze^- \rightarrow M$, which form a highly conductive filament in the ON state of the cell. When the polarity of the applied voltage is reversed, an electrochemical dissolution of the CF takes place, resetting the system into the OFF state [Fig. 5(b)] [8, 34].

Anion migration. A second class in this category operates through the migration of anions, typically oxygen ions/vacancies, towards the anode/cathode. An electrochemical reaction (redox processes) occurs at the electrode and RS takes place [Fig. 5(c)] [34]. The dominant migration driving force is the electrostatic potential gradient applied through the oxide and the accompanying Joule heating effect facilitates the redox reaction at the anodic interface over the area where electrons flow [10]. The anodic interface serve as an oxygen vacancy source, while the cathodic one influences the oxygen vacancies distribution [34, 10]. The set process recovers the electrical conductivity of the locally ruptured part of the CF by the milder electric-field-assisted migration of oxygen ions [10]. During reset of a bipolar device, oxygen ions migrate back to the bulk either to recombine with the oxygen vacancies or to oxidize the metal precipitates. For unipolar reset, thermal dissolution (Joule heating) or re-oxidation (oxygen diffusion) of a CF is the most important factor [7, 10]. RS devices involving anions are usually composed of metal oxides, particularly transition metal oxides, and some lanthanide series metal oxides. In particular, HfO_x, AlO_x, NiO_x, TiO_x, and TaO_x have drawn the most attention and have been extensively studied in the last years [7, 34].

1.4 Neuromorphic Properties of Memristors

1.4.1 Spike Timing Dependent Plasticity

To relate memristance to biological STDP, one requires a voltage/flux controlled bipolar memristor with voltage threshold, below which no variation of the resistance is observed, and an exponential behavior beyond threshold to be able to increment and decrement the conductance [3]. Jo *et al.* were the first to demonstrate STDP in nanoscale Si-based memristors in a crossbar structure [Fig. 6(a)]. The conductance continuously increases (decreases) during the positive (negative) voltage sweeps, and the I(V) slope of each subsequent sweep picks up where the last sweep left off [Fig. 6(b)] [11]. It was also found that the strength of STDP learning in memristors can be modulated by changing the amplitudes (or shapes) of the electric spikes, i.e., the

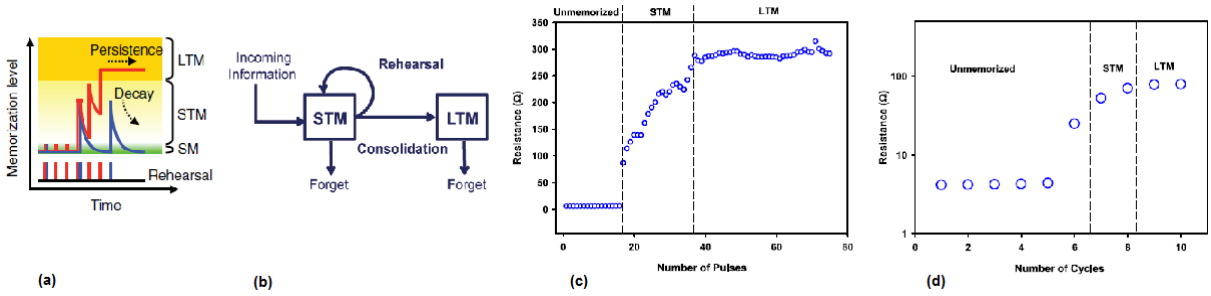

Figure 7: (a) New information (sensory memory; SM) stored in STM for short time, while repeated rehearsals result in LTM. At higher repetition rates, rehearsal before complete decay forms LTM (red line). Rehearsal at lower repetition rates cannot form LTM (blue line; taken from Ref. [9]). (b) Schematic of the multi-store memory model (taken from Ref. [13]). Resistance of a Au/Ti/NiO/Au/Ni device (c) as a function of the number of pulses and (d) evolution of the device resistance with cycling in the backward sweeping mode (taken from Ref. [14]).

conductivity can be tuned depending on the precise timing between the post- and pre-synaptic spikes and the learning window by changing the shape of the pulses [3]. Choi *et al.* fabricated $Pt/Cu_2O/W$ MIM structures and experimentally demonstrated the successful storing of biological synaptic weight variations. They also showed the reliability of plasticity by varying the amplitude and pulse-width of the input voltage signal matched to the biological plasticity [26]. Pavlov's experiment was implemented using memristive synapses in a two-input, one-output system [Fig. 6(c)] [12]. The output is initially only triggered by one input but after a "learning step" in which both inputs fire, the output can be triggered by either input.

1.4.2 Short-Term Memory and Long-Term Memory

Depending on the input voltage pulses, different memorization behaviors were observed in memristive devices: short-term memory (STM) for low and long-term memory (LTM) for high repetition rates [33] (STP and LTP are terms used in neuroscience, whereas STM and LTM are terms used to describe psychological phenomena [28]). STM can only be sustained by constantly rehearsing the same stimulus, while LTM, despite the presence of natural forgetting, can be maintained for a longer period of time without follow-up stimuli. The transition from STM to LTM also happens through repetitions (rehearsal) but involves a much more intricate process with structural changes [consolidation; Figs. 7(a) and (b)] [13, 28]. As shown in Fig. 7(c), three memory stages (unmemorized, STM and LTM) were observed in a Ni-rich nickel oxide device by Liu *et al.* Figure 7(d) shows that memorization from STM to LTM can also be obtained by repeated forward and backward voltage sweepings [14]. Tsuruoka *et al.* found LTM in an $Ag/Ta_2O_5/Pt$ cell under voltage bias for high repetition rates of input pulses, which is analogous to the behavior of biological synapses [33]. Wang *et al.,* noted that when the applied voltage is removed a spontaneous decay of synaptic weight occurs. The experimental values obtained for such amorphous InGaZnO memristor were comparable to those of the activation energy and of the diffusion coefficient of oxygen ions already reported. The decay rate is very large at the initial stage and then gradually decreases, which is consistent with the human "forgetting curve". Their results further indicate that in synaptic devices with "learning-experience", re-learning is easily achieved. They further showed that, with increasing number of stimulations, the relaxation time increases from several seconds to tens of seconds and tends to saturate beyond 100 stimulations, indicating a decreasing forgetting rate [25].

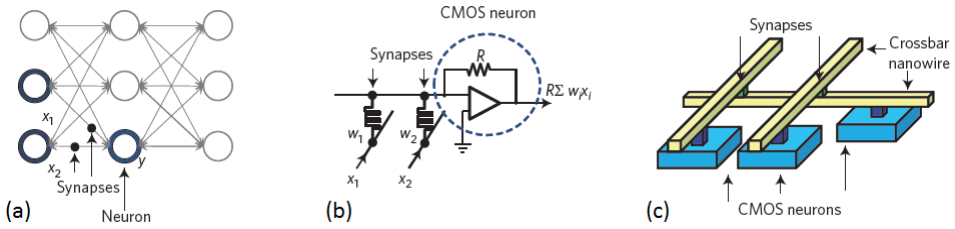

Figure 8: Bio-inspired and mixed-signal information processing: hybrid CMOS/memristor circuits may also enable efficient analogue dot-product computation, which is a key operation in artificial neural networks and many other information processing tasks. In the simplest model, artificial neural networks can be represented by a graph with nodes corresponding to neurons and graph edges that correspond to synapses (taken from Ref. [15]).

1.4.3 Artificial Network Systems

The network model is based on the transmission of events from one source node (neuron) to multiple by edges (synapse; see examples in Fig. 8). To facilitate the communication between the neurons, the action potential is propagated as a digital pulse [36]. The output of a neural network node is a function of the sum of all input signals [12]. For a very large number of synapses, a practical implementation of an artificial network allows the weights to be updated in parallel, by multiplying the logic value of the input ('1' and '0') by the memristance value, due to the high interconnectivity [12, 37, 38]. When a node is in spiking mode, it ignores all incoming spikes mimicking the "refractory period" seen in biological neurons [39].

Many different learning laws have been proposed for edges [39]. Adjustable edge weights are the defining characteristic of neural networks and are the origin of their broad adaptive functionality [12]. An edge's conductance changes as a function of the voltage drop across the edge induced by forward spikes from the source node and back spikes from the sink node [39]. Using memristive nanodevices to implement edges, conventional analog and digital electronics to implement nodes, and pairs of bipolar pulses, called "spikes", to implement communication, it is possible to develop fully electronic neuron emulators [39]. It should be noted that, for ANN systems, the density of the memristive devices is the most important property. Also, ANNs are much more resilient to variations in synapses and neurons [37]. For example, instead of a single pulse, the average effect on hundreds of parallel synapse inputs into one neuron determines whether the neuron will fire or not. Therefore, there is no need to completely eliminate the randomness of the RS [5].

One of the possible applications of memristor-based ANNs is to carry out position detection. This is simulated in Ref. [40], using ANNs that combine winner-take-all and STDP learning rules. Random nanowire networks [NWNs; Fig. 9(a)-(f)], where placement is not important and differences in properties are averaged out, also presented I(V) memristive-like behavior. So, the electrical properties of the NWN can be modeled as a leaky resistor-capacitor network with randomly distributed junctions, taking into account the distribution of breakdown voltages across individual junctions [16].

Bridge. Memristor Bridge Synapses have been proposed [1, 41], which employ several identical memristors (typically four) to construct a single synapse and have advantages over a single-memristor synapse. They allow for zero, negative and positive weights and can still be compact due to the fact that the bridge is controlled by the same input via time-sharing. The basic model for a Memristor Bridge Synapse is presented in Fig. 9(g). The output voltage of the memristor bridge is the voltage difference between A and B, given by:

$$V_{out} = V_A - V_B = \left(\frac{M2}{M1 + M2} - \frac{M4}{M3 + M4} \right) V_{in} \,, \tag{12}$$

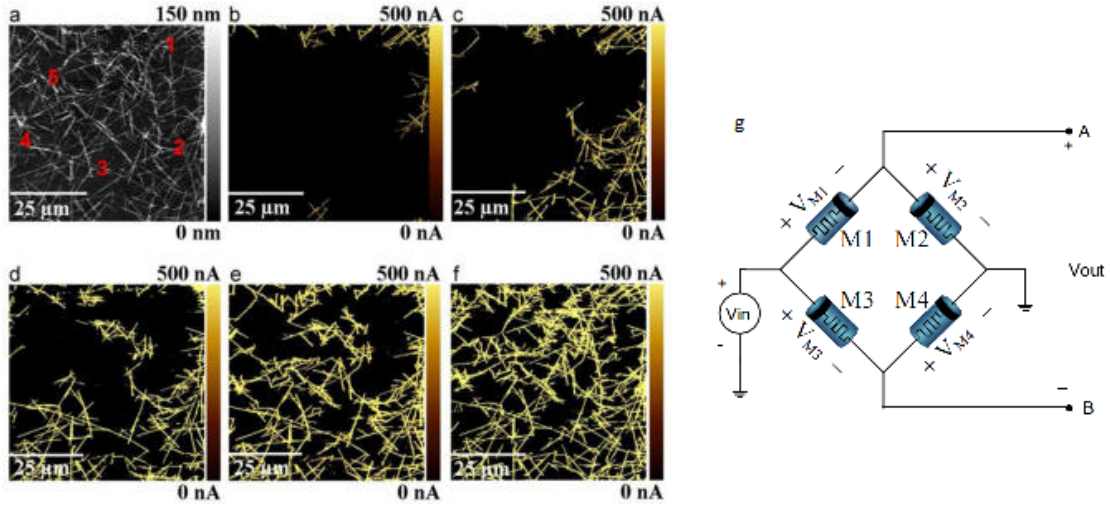

Figure 9: (a) Topography of a random network of Ag nanowires. A metal coated atomic force microscope tip was used to locally activate sites in the network by applying a voltage pulse. The current maps shown in (b)-(f) are the result of applying the voltage pulses at selected regions (marked 1-5 on the topographic map; taken from Ref. [16]). (g) Memristor bridge circuit. It is assumed that M1 and M4 are decrementally biased memristors while M2 and M3 are incrementally biased memristors (taken from Ref. [1]).

which can be seen as a relationship between synaptic weight and input signal. When a positive or negative strong pulse is applied at the input terminal of the memristor bridge synapse, the memristance of each memristor is increased or decreased depending on its polarity. For a positive pulse at the input terminal, the memristances M1 and M4 (decrementally-biased) decrease and the memristances M2 and M3 (incrementally-biased) increase. The two serially-connected memristors with opposite polarities operate complementarily. The total memristance of two serial memristors is constant and the output is the linear multiplication between the input pulse and weighting factor. Thus, the memristor bridge circuit acts as a synapse [1, 41]. In addition, the bridge circuit acts as a multiplier circuit, which can be used to replace the conventional nonlinear analog multipliers [1].

Crossbar Arrays. Passive crossbar memory arrays are the simplest conceivable matrices consisting only of "bit" and "word" lines and a resistive switch at each junction, as shown in Fig. 8(c) [35, 42]. In a crossbar structure, a two-terminal memristor synapse is formed at each crosspoint and connects pre- and post-synaptic neurons. Every neuron in the "pre-neuron" layer of the crossbar configuration is directly connected to every neuron in the "post-neuron" layer [35, 11]. Obviously, higher memory density can be achieved in crossbar architectures than in CMOS architectures and, with 3D stacking, the memory density can be further increased [34]. During electroforming, writing, erasing and reading a voltage applied to each cell in the array will be different so that miswriting and misreading easily take place unless the difference between writing and erasing voltages and R_{OFF}/R_{ON} are large enough. Uniform electroforming of switching cells in a crossbar array becomes more difficult with further scaling down because the higher resistance and voltage drop along the lines hinder application of the same electroforming voltage to each cell [43].

1.5 Silver Sulfide

Silver sulfide (Ag_2S) is a binary chalcogenide semiconducting (0.9 eV band gap) material, composed of a chalcogen element from the group VI of the periodic table (S) and an electropositive element (Ag). Its

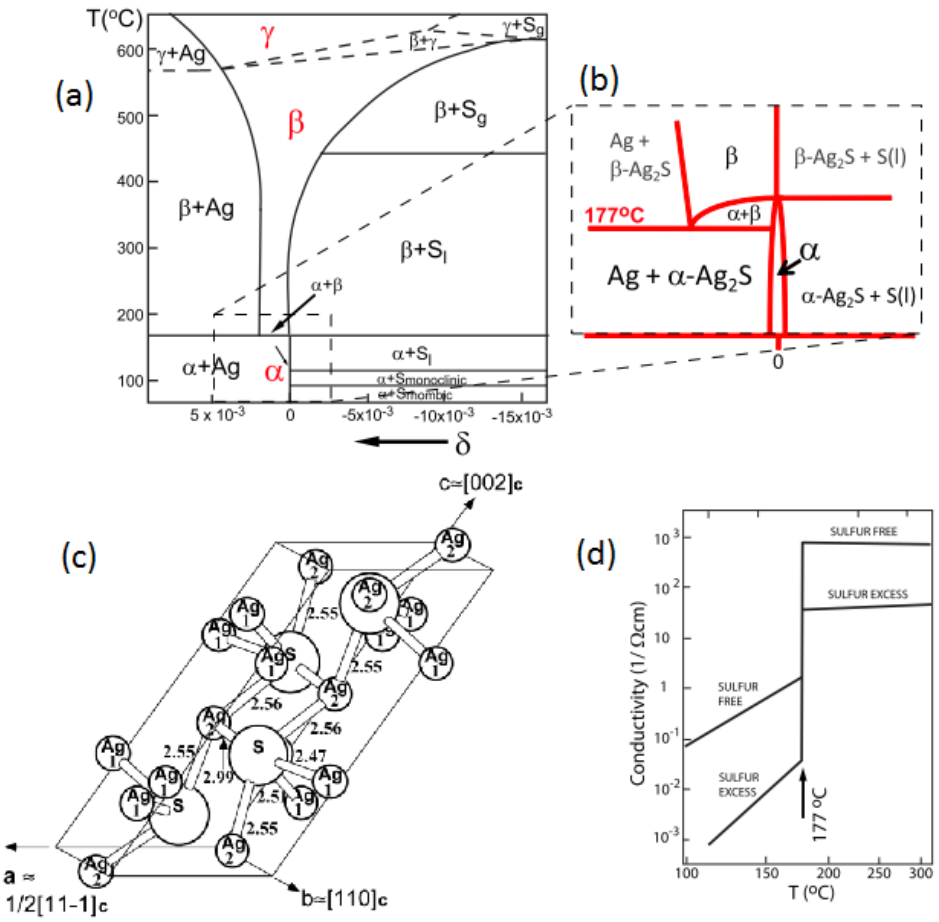

Figure 10: (a) Phase diagram of the Ag-S binary system, (b) zoom-in of the phase diagram at the α - β transition region (taken from Ref. [17]), (c) crystal structure of α-$Ag_{2+\delta}S$ (taken from Ref. [18]) and (d) electrical conductivity of Ag_2S versus temperature; the upper curves marked S-free and the lower curves marked S-excess represent the upper and lower limiting conductivities corresponding to equilibrium with Ag and S, respectively; the temperature of 177 °C represents the transition from the β-phase (below) to the α-phase (above; taken from Ref. [19]).

properties have called the attention of solid state scientists since the times of Faraday because they can be easily modified by small changes in temperature, pressure or other external parameters (e.g. voltage). It has potential applications in electronic devices, solar, fuel cells, batteries and memories. In particular, the use of Ag_2S in electrochemical photovoltaic (EPVC) storage cells has increased the current storage efficiency to about 90% [44]. Ag_2S is also an extremely good solid electrolyte due to its high ionic mobility, making it particularly interesting for the study of resistive switching effects [45].

The silver rich $Ag_{2+\delta}S$ (with $10^{-3} < \delta < 2.5 \times 10^{-3}$ [46]) composition is a mixed ionic-electronic conductor (MIEC), with a total conductivity due to the transport of both Ag^+ ions and electrons. Ag_2S presents a good chemical stability and exists in three stable phases: α, β and γ, in order of increasing temperature. The low temperature phase (α-$Ag_{2+\delta}S$), also called acanthite, is only stable within the narrowest range of non-stoichiometry [Fig. 10(b)] with a composition range ($\delta_\alpha{}^{max}$) in the order of 10^{-6} [17]. At 177 °C, Ag_2S transforms to β-$Ag_{2+\delta}S$, the high temperature phase, called argentite. The range of non-stoichiometry of the β-phase is much broader than that of the α phase [Fig. 10(a)], with $\delta_\beta{}^{max}$ in the order of 10^{-3}. The crystal structure of the low temperature phase α-$Ag_{2+\delta}S$ is monoclinic (space group P21/c, with a = 4.231 Å, b =

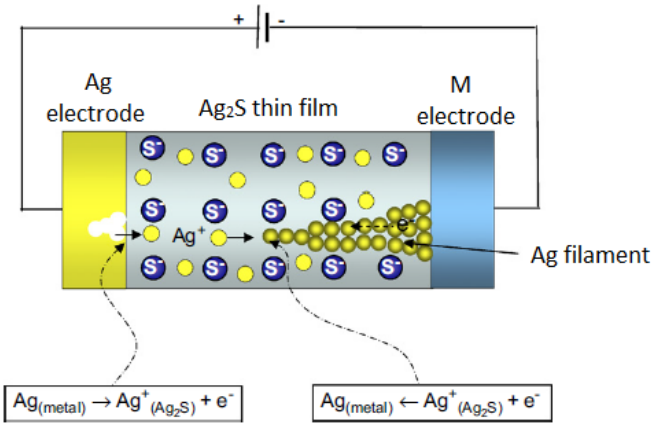

Figure 11: Local solid-state electrochemical process for the growth of an Ag filament inside an Ag_2S mixed conductor (taken from Ref. [20]).

6.930 Å, c = 9.526 Å and $\beta = 125.48^{o}$). This superstructure is composed of a slightly distorted body-centered cubic (bcc) lattice, formed by covalently bonded S atoms. The Ag^+ ions are distributed in octahedral and tetrahedral positions in the lattice. Since the number of available octahedral and tetrahedral sites is much larger than the number of Ag^+ ions, there are always lattice sites available for them to move into. This is what gives rise to the high ionic mobility of Ag_2S [Fig. 10(c)] [17, 47].

As shown in Fig. 10(d), in the low temperature phase, the total conductivity ($\sigma_{total} = \sigma_{e^-} + \sigma_{Ag^+}$) exponentially increases with temperature, presenting a semiconductor behavior. The conductivity in the β phase varies only slightly with temperature, showing a metallic behavior. The contribution of the electronic conductivity to the total conductivity is, in both phases, higher than the ionic contribution [45].

Ag_2S has a potential use in resistive electrical switches and has been recently studied for $Ag/Ag_2S/M$ (M - inert metal) junctions, where, above a certain voltage critical value (threshold), a metallic connection between the electrodes can be formed. It is generally accepted that the Ag electrode is oxidized, providing a constant feed of Ag^+ ions which, at negative bias, travel through the Ag_2S structure to be reduced at the other end of the junction (M electrode) via the formation of a conductive Ag filament (ON state), as shown in Fig. 11. At positive bias, the Ag metallic contact dissolves into the Ag_2S matrix, which is seen by a large increase of the resistance (OFF state) [48].

For Ag nucleation inside the Ag_2S film to occur, allowing conductance switching due to filament formation, a critical supersaturation of Ag^+ ions inside the Ag_2S layer is required [49]. By increasing the voltage, one increases the Ag concentration gradient, until supersaturation reaches a critical value and metallic Ag precipitates at the Ag_2S/M interface. This is even more critical when there is no additional supply of Ag^+ ions into the Ag_2S layer, as reported by Kundu *et al.* [50].

Kundu *et al.* reported an Ag_2S gapless-type resistance switch [50] and the operation of a photo-assisted memory has been demonstrated using Ag_2S as an ionic and electronic mixed conductor [51]. Furthermore, Ohno *et al.*, reported that Ag_2S can emulate the synaptic functions of STP and LTP through the use of input pulse repetition time [52] and observed the formation of STM for the same type of structures [53]. They can thus function as "inorganic synapses", a memory kernel by the atomic ionic structure [54, 55]. Avizienis *et al.*, reported an hardware-based platform comprised of over a billion interconnected Ag_2S synapses embedded in a network of silver nanowires. Also, emergent behaviors akin to brain function were observed using Ag_2S structures, namely spatially distributed memory, recurrent dynamics and the activation of feedforward subnetworks [54]. Then, Ag_2S devices demonstrate different learning abilities, which are controlled by the

unique behavior of solid-state electrochemical reactions when confined to the nanometer scale, without the need of external pre-programming. This will enable the hardware implementation of artificial neural networks without the need of software and the problematic non-scalable wiring [52, 55].

For all these possibilities, we have chosen to study here the Ag_2S system, to develop and optimize a model presenting activity-dependent modifications and offering the possibility to be implemented in artificial neural networks.

1.6 Conclusion

The performance of present day computers is a limiting factor in the progress of computational neuroscience research. It is envisaged that the understanding of the biological brain will lead to the building of brain-like computer systems, and that the overall architecture and principles of operation of these future computing devices could be closely modeled on biology. Considering memory an essential building block in learning and decision-making, the demonstration of such functionalities in a nanoscale memristor synapse is crucial to emulate neuromorphic systems and artificial neural networks [13]. Memristor technology has the potential to revolutionize computing and scientific research in the coming decades.

'EXPERIMENTAL SETBACKS'

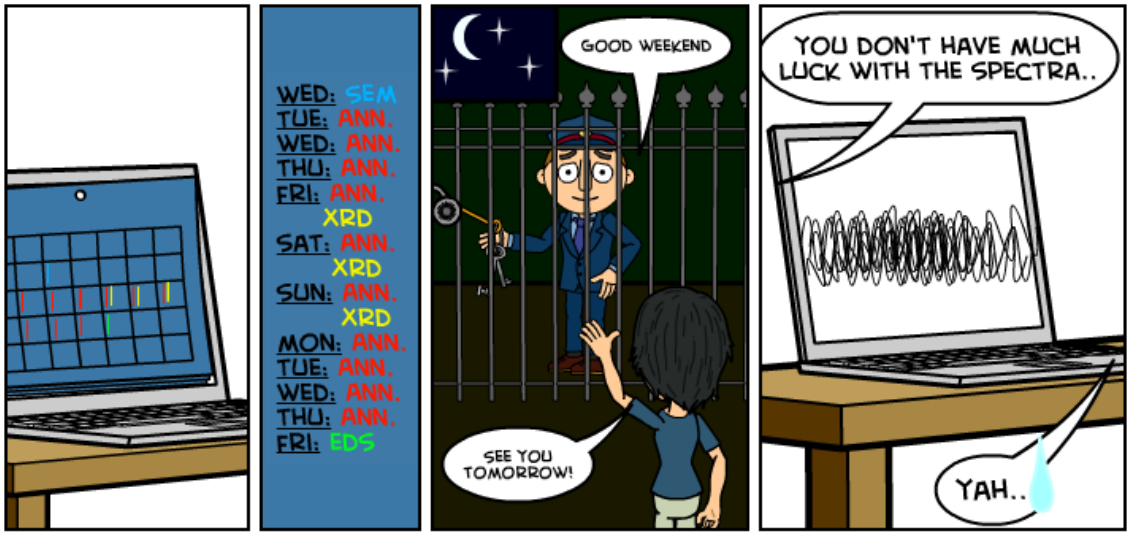

Chapter 2
Experimental Details

2.1 Sample Preparation

2.1.1 Ion Beam Deposition

Ion Beam Deposition (IBD) is an appropriate method for the fabrication of so called out-of plane devices, with the advantage of operating with any material both for target and substrate. As the name suggests, it consists on the sputtering of a target by accelerated (500 - 1500 V) inert ions (in our case Argon) in High Vacuum (HV; base pressure $\sim 5 \times 10^{-7}$ Torr). The HV in the used IBD system is composed by a mechanical, a turbomolecular (assisted by a mechanical pump) and a cryogenic pump. In the deposition gun [Fig. 12(a)], the electrons thermo-ionicaly generated from a tungsten filament (cathode) are accelerated to the anode in an helicoidal trajectory (to increase the Ar ionization probability), due to a magnetic field created by magnets surrounding the anode. These electrons then collide with the Ar gas atoms, ionizing them and creating a plasma. These ions are finally accelerated towards the chamber [Fig. 12(b)] by a potential applied at the grid at the end of the gun, which also focuses the beam and is protected by a previous grid. In the case of dielectric deposition, a neutralizer filament (tungsten) is placed at the end of the gun, so that thermo-ionicaly emitted electrons are distributed to cancel the overall ionic beam's electric charge. The transfer of momentum between the focused beam and the atoms at the surface of the target sputters and directs them towards the substrate where the material is then deposited. Both the chamber, the sample holder and the substrate holder are cooled by a water circuit. For faster cooling after deposition and to prevent oxidation, the chamber is filled with nitrogen gas (N_2) for 1h before being opened. The rotation of the substrate holder improves the thickness uniformity and, by regulating the incidence angle, it is possible to create preferential directional growth. The targets holder bears up to four targets, which allows the deposition of four different materials without disrupting vacuum.

Our devices were grown on one square inch glass substrates using an Ion Beam Sputter Deposition system by Commonwealth Scientific Corporation (IFIMUP). The substrates were successively cleaned using alconox, acetone and ethanol in ultra-sons for 15 minutes. The typical deposition parameters are: base pressure $< 10^{-6}$ Torr, working pressure of 1.6×10^{-4} Torr, a cathode current of 7 A, a discharge current of 2 A, a voltage beam of 993 V, an acceleration voltage of 148.5 V, an Ar flux of 5 sccm, a substrate holder rotation of 70 rpm and, when necessary, a current neutralization of 12 mA.

2.1.2 Electrodeposition and Chemical Routes

A metallic material can be deposited on a conducting substrate using an electrodeposition method, in which the electrochemical reduction of metallic ions present in an electrolyte solution occurs. The electrolyte is an ionic conductor with the metal of interest dissolved into a suitable solvent. The setup used for electrodeposition consists of an electrodeposition cell with three electrodes, being the substrate where the metal is deposited the cathode (working electrode), a Pt mesh the anode (counter electrode) and the reference an Ag/AgCl electrode (Fig. 13).

Ag_2S electrodeposition was performed in a Cu tape substrate using a solution containing 0.055 mol l^{-1} of $AgNO_3$ (99.9 %) and 0.19 mol l^{-1} of elemental sulfur (99.98 %) dissolved in dimethyl sulfoxide (DMSO) [56] as the electrolyte [57]. The general reaction of the electrodeposition procedure may be presented as:

$$2Ag^+ + S + 2e^- = Ag_2S\,, \tag{13}$$

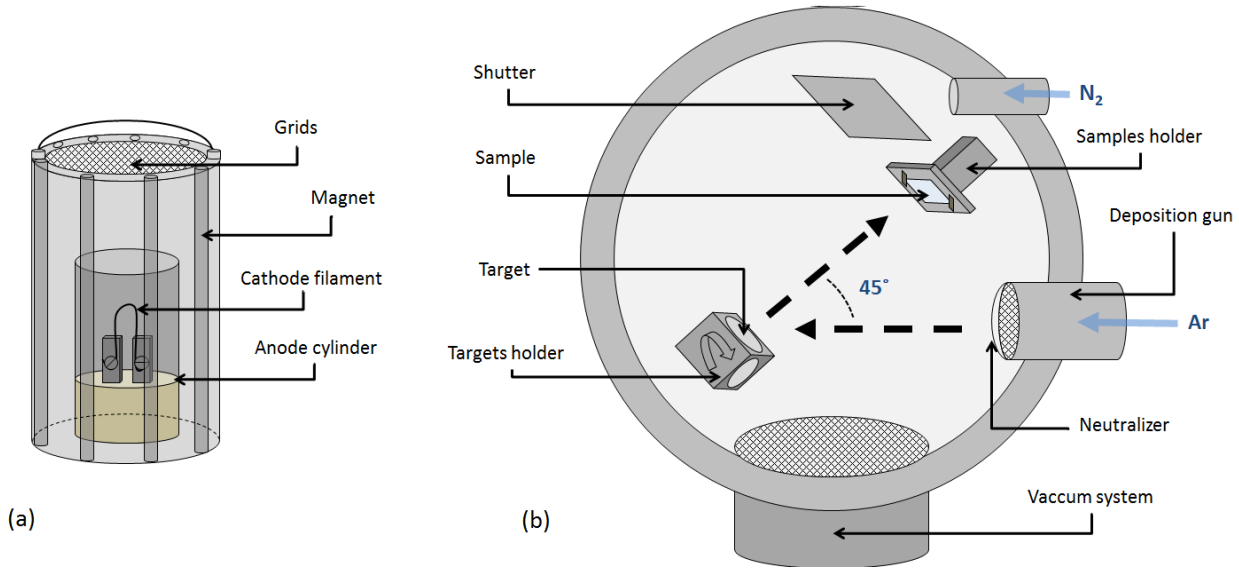

Figure 12: Scheme of the (a) IBD deposition gun and (b) chamber used for electrodeposition.

which may occur via two different routes. In the first, the element sulfur in the solution diffuses and is absorbed by the electrode surface. These atoms are then electrochemical reduced, followed by the reaction with Ag^+:

$$S + 2e^- = S^{2-}\,, \tag{14}$$

$$2Ag^+ + S^{2-} = Ag_2S\,. \tag{15}$$

Such reaction only takes place when the electrode potential reaches the potential for S^{2-} formation (-0.4284 V). The second pathway occurs when the reduction potential of Ag^+ (0.7996 V) is reached [58] and involves the chemical reaction between S and Ag as:

$$Ag^+ + e^- = Ag\,, \tag{16}$$

$$S + 2Ag = Ag_2S\,. \tag{17}$$

The electrodeposition was performed in an appropriate cell at a temperature of around 50 °C with magnetic stirring of 150 rpm. Different applied potentials were used to obtain the intended samples, ranging from -0.8 to -0.4 V (referred to the reference electrode).

The simple dipping of a sample in a solution can unleash chemical reactions between the two. We have therefore also carried out a study of dipping Ag thin films into a DMSO + S solution and probed the dependence of the stoichiometry of the resulting product on dipping time (t), temperature (T) and sulfur concentration (c_S). The experiments were carried out in a beaker on an heating plate, as shown in Fig. 14, and then the samples were cleaned with acetone and deionized water, and dried with N_2 gas. The dissolution of sulfur in DMSO is a very tricky process since agitation must be maintained throughout the whole process, otherwise the S powder attaches to the walls of the beaker; also, the temperature has to be carefully increased for S dissolution to occur without its evaporation. In fact, vapors begin to appear for a solution temperature of 80 °C (that roughly corresponds to 45 °C in the water). Note that the solution temperature depends highly on the depth, and the stated values concern measurements close to the surface.

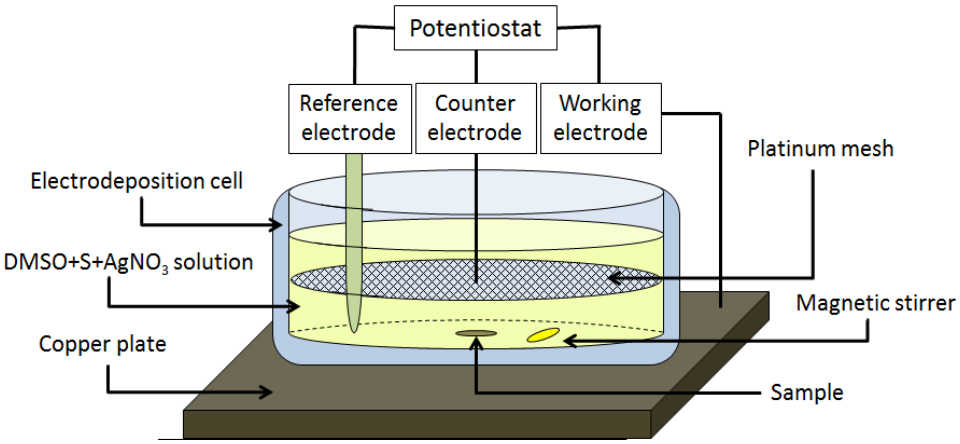

Figure 13: Scheme of the three-electrode setup.

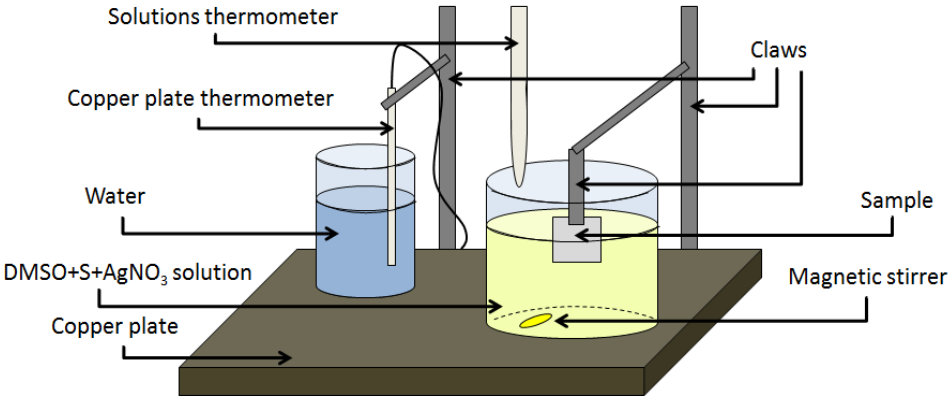

Figure 14: Scheme of the heating and dipping setups.

2.1.3 Sulfurization

Silver (Ag) sulfurization is the conversion of Ag into Ag_2S by its reaction with sulfur (S) vapor,

$$2Ag(s) + S(v) = Ag_2S(s)\,. \tag{18}$$

It is a relatively simple method and was here performed both in vacuum and at atmospheric pressure, at temperatures ranging from room temperature up to approximately 350 °C. Sulfurization starts with the direct reaction of Ag atoms near the surface of the film with the S vapor, forming an Ag_2S layer. At high temperatures the Ag ion mobility is very large, allowing a continuous reaction of the S vapor with the diffusing Ag atoms on the growing surface. Because of the single oxidation state of Ag, the sulfurization of an Ag film usually results in a single phase material (acanthite, the room temperature phase) [45]. After the ion beam deposition of thin films from Ag or Ag_2S targets, followed the synthesis of Ag_2S by sulfurization. The samples, always one of Ag and another of Ag_2S, and the sulfur powder were horizontally loaded into a quartz cylindrical tube of (17.0 ± 0.5) mm internal diameter and (720 ± 0.5) mm long (Fig. 15). Different sulfur powder masses were used, although according to the calculus from the Van der Waal's real gases equation, the necessary mass to balance the equation is unmeasurable and satisfied if used in excess. Once the sulfur and the sample were loaded, the tube was evacuated under vacuum, down to about 10^{-3} Torr to exclude contact with air. The temperature in the tube was then increased to the desirable value under a controlled heating rate using a vertical furnace with a programmable temperature controller. The tube was kept under static vacuum to

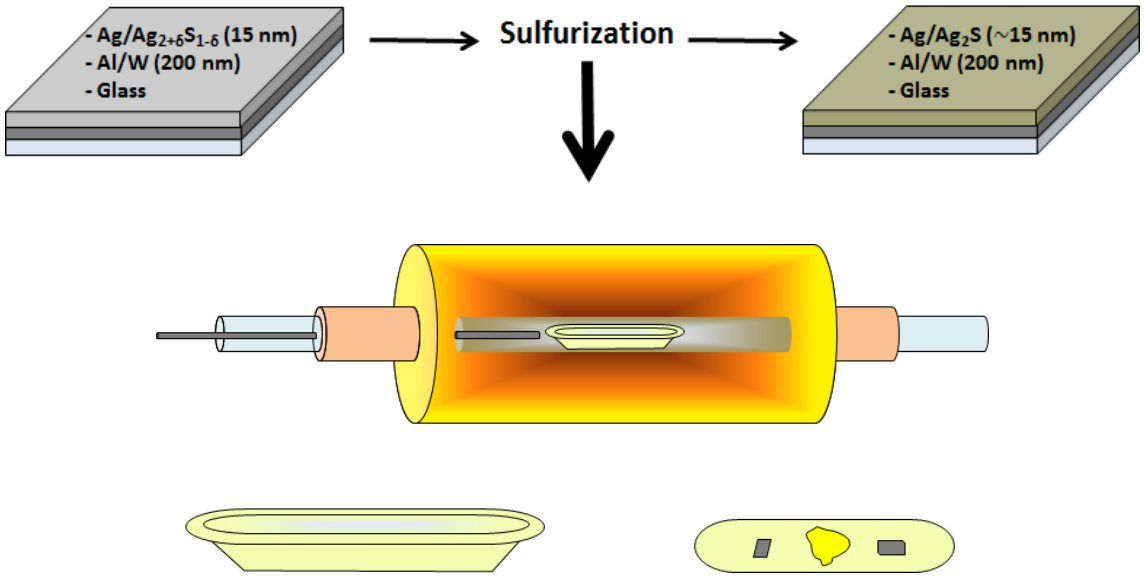

Figure 15: Scheme of the sulfurization steps of the ion beam deposited Ag and Ag_2S thin films by annealing in sulfur atmosphere.

create a sulfur atmosphere, while the temperature remains constant a certain time. After that, the sample was cooled down to room temperature at a controlled rate or natural cooling.

2.1.4 Microfabrication

To obtain the final metal-insulator-metal (MIM) structures having junction areas between 1 - 10 μm^2 for four-contact measurements, the microfabrication includes the deposition of the layers that form the initial stack [Fig. 16(a)] using a relevant technique and mask transfer by photolithography. Each photolithographic step consists in the positive photoresist coating using an automatic setup for the dispense and spinning, to improve the thickness and composition homogeneity, followed by the photo-exposition of a pattern that alters the photoresist molecular boundings and stiffens it. Then, for this case, development using the proper developer removes the non-exposed photoresist, being the areas only protected by the photoresist in the desired pattern. The first pattern [Fig. 16(b)] allows to etch down to the substrate all the structure but the bottom electrodes, bottom leads and the sample's area. After the resist is removed, a new pattern is exposed, protecting the bottom electrodes and the sample [Fig. 16(c)]. A new etching is then performed, that must be stopped at the bottom metallic layer, as to define the bottom leads. The next step is the deposition of a Al_2O_3 passivation layer [Fig. 16(d)] to avoid any electric contact between the bottom and top electrodes. Finally, Fig. 16(e) shows the definition of the top electrodes through Al metal deposition and lift-off processes of the photoresist previously deposited, exposed and revealed, being the final structure defined [Fig. 16(f)].

The layers deposition was performed using an Ion Beam Sputter Deposition system by Commonwealth Scientific Corporation (IFIMUP), while the lithography steps were accomplished in INESC-MN (Lisbon) in a Class 100 clean room area with a Class 10 lithography area. Before patterning, the samples were first prepared in a hexamethyldisilazane (HMDS) vapor prime oven at 130 °C. The first Ion Beam Milling (etching) step and the Al (top electrode) deposition were performed in a Nordiko 3600 while the second etching used a Nordiko 3000. The photolithography was done using a Heidelberg Direct Write Laser Lithography system with a 442 nm HeCd laser and the insulating Al_2O_3 layer deposited in an homemade UHV2 at 2.3×10^{-3} Torr. The photolithographic masks used and the complete process runsheet are presented in Appendix A and B, respectively.

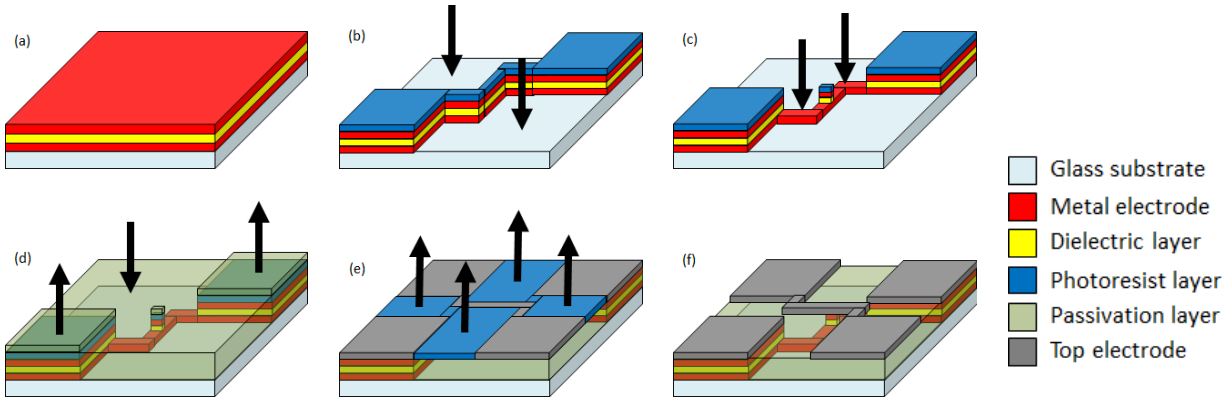

Figure 16: Microfabrication process of a MIM nanostructure. (a) Initial layered structure, (b) first and (c) second lithography steps, (d) passivation layer deposition and lift-off, (e) top electrode deposition and final lift-off and (f) desired structure.

A simpler form to fabricate a top electrode with a few hundred μm^2 is to use a shadow mask. Shadow Masking is a patterning technique which uses a metal plate punched with tiny holes on the micrometer scale as a mask to define portions of the film which will be deposited. In other words, the deposition will only take place in the substrate where the mask does no shadow. A 2-hole macroscopic ($\O \sim 2$ mm) copper shadow mask was used to deposit two 50 nm gold electrodes sputtering using a BOC Edwards Scancoat (IFIMUP).

2.2 Sample Characterization

2.2.1 X-ray Diffraction

X-ray diffraction (XRD) allows the identification and structural characterization of crystalline materials by means of the interaction between X-rays and electrons in atoms. Bragg diffraction occurs since the wavelength of the radiation is of the same order of magnitude as inter-atomic distances, which act as diffraction centers. The diffraction pattern consists of both constructive and destructive interferences, being the former associated with a maximum intensity peak occurring for certain angles, according to:

$$n\lambda = 2d_{hkl}\sin\theta\,, \tag{19}$$

where n is an integer, λ the wavelength of the incident wave, d_{hkl} the distance between planes with the Miller indexes (hkl) and θ the angle between the atomic plane and the incident (or scattered) beam.

The XRD spectra can also give an estimation of the size of sub-micrometer particles, which may be smaller or equal to the grain size, through the broadening of a peak in a diffraction pattern, according to the relation:

$$\tau = \frac{K\lambda}{\triangle(2\theta)\cos\theta}\,, \tag{20}$$

where τ is the mean size of the crystalline domains, K is a dimensionless shape factor, with a typical value of 0.9 (but that depends on the actual particle shape) and $\triangle(2\theta)$ is the line broadening at half the maximum intensity (FWHM), after subtracting the instrumental line broadening.

XRD patterns were taken at room temperature using a Siemens D5000 diffractometer (IFIMUP) in the locked coupled $(\theta - 2\theta)$ geometry and the Cu-K_α line with a wavelength of 1.54 Å. Typical spectra parameters are a scan range from 20° to 65°, in 0.015° steps, and an acquisition time of 14 s *per* step.

2.2.2 Scanning Electron Microscopy

The Scanning Electron Microscopy (SEM) technique consists in the irradiation of the sample with a beam of high energy electrons focused by a set of magnetic lenses in HV. The interaction of the electrons with the sample in the near surface originates the emission of electrons and photons, such as Secondary Electrons (SE), Backscattered Electrons (BSE) and X-rays, used to form the image. Topographic information is given by the SE resulting from ionization, while the atomic number relation is given by the BSE, which are primary (beam) electrons that suffer an elastic backscattering event. Therefore, the number of backscattered electrons provide an image with the distribution of elements, the brighter the higher the atomic number.

Due to the short wavelengths typical of electrons, a high resolution is possible, being SEM an important morphological characterization technique. The surface morphology of our samples was examined by a high resolution FEI Quanta 400FEG scanning electron microscope at CEMUP at an electron beam energy of 15 kV, with a resolution up to 50 nm.

2.2.3 Energy Dispersive Spectroscopy

The information about the chemical elements that form the samples was obtained from Energy Dispersive Spectroscopy (EDS), incorporated in the SEM (CEMUP), that analyzes the emitted X-ray spectrum. The removal of inner shell electrons by the incident beam results in vacancy occupation by an outer electron, which then emits element-specific radiation, and allows qualitative and quantitative analysis on the elements present in the scanned area. The stoichiometry of the samples was probed by EDS analysis, with the spectra taken at 10 kV electron beam energy.

2.2.4 Fourier Transform Infrared Spectroscopy

Many substances can be characterized, identified and also quantified by Infrared (IR) spectroscopy, by measuring the changes that occur in a total internal reflected IR beam when the beam comes into contact with a sample. The technique of Attenuated Total Reflectance (ATR) allows faster sampling, since it is a technique used in conjunction with IR which enables samples to be examined directly in the solid or liquid state without further preparation. An IR beam incident on an optically dense crystal with a high refractive index at a certain angle creates an evanescent wave from the internal reflectance, that extends beyond the surface of the crystal into the sample held in contact with it. The evanescent wave will be attenuated or altered in the IR spectrum regions where the sample absorbs energy. We used a Perkin-Elmer Spectrum 100 Series with ATR, at room temperature in the 650 - 4000 cm^{-1} range over 32 cycles, with 2 cm^{-1} resolution.

2.2.5 Raman Spectroscopy

Raman spectroscopy allows the identification of vibrational modes in a system through the interaction between a (monochromatic) laser beam and the molecular vibrations, phonons or other excitations of the system, giving complementary information to IR spectroscopy. This results in energy transfer (inelastic scattering) with the excitation of the molecule to a virtual energy state and the shift of emitted photons energy to lower (Stokes Raman Scattering) or higher (Anti-Stokes Raman Scattering) frequencies. The unpolarized Raman spectra were obtained with a T64000 Jobin-Yvon triple spectrometer (IFIMUP), coupled to a liquid-nitrogen-cooled charge coupled device with a spectral resolution of 0.15 cm^{-1}. The excitation line was the 514.5 nm of a HeNe laser, with powers of 7 mW (17 A), 15 mW (18 A), 27 mW (19 A) and 38 mW (20 A).

Igor software was used to fit the experimental data according to the sum of independent damped harmonic oscillators:

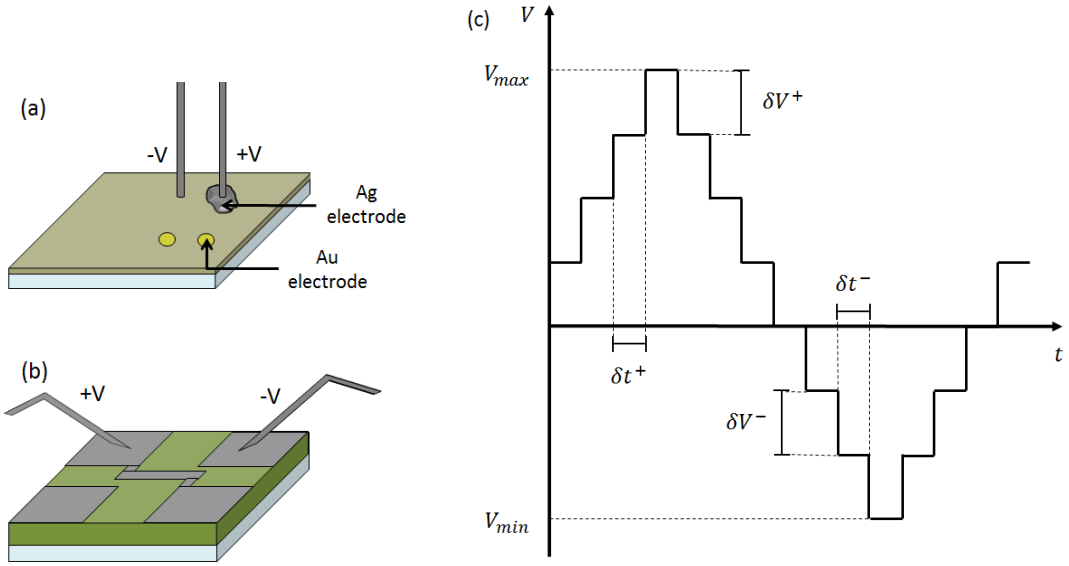

Figure 17: Scheme of the (a) planar and (b) perpendicular measurement setup, and (b) of the applied voltage swept over time.

$$I(w,T) = [1 + n(\omega,T)] \sum_{j=1}^{N} A_{oj} \frac{\omega \Omega_{oj}^2 \Gamma_{oj}}{(\Omega_{oj}^2 - \omega^2)^2 + \omega^2 \Gamma_{oj}^2}\,, \tag{21}$$

where $n(\omega, T)$ is the Bose-Einstein factor, A_{oj}, Ω_{oj} and Γ_{oj} are the oscillator strength, wavenumber and damping coefficient of the jth oscillator, respectively [59].

2.2.6 Transport measurements

The formation of semiconducting Ag_2S was confirmed using electrical transport measurements (current - voltage characteristics). The electrical measurements were performed both in a parallel setup [current in plane configuration; Fig. 17(a)] and also perpendicularly across the Ag_2S layer [current perpendicular to the plane configuration; Fig. 17(b)], using different electrodes. During the measurements, the voltage was swept in the $0 \rightarrow V_{max} \rightarrow 0 \rightarrow V_{min} \rightarrow 0$ sequence (where V_{max} is the maximum positive and V_{min} is the maximum negative applied voltage; allowing asymmetric cycles to be performed), with separately defined voltage steps (δV^+, δV^-) and delay times (δt^+, δt^-) for positive and negative ranges [Fig. 17 (c)]. The delay time is the duration each voltage step is applied. Positive and negative current compliances were established to avoid damaging the sample. Direct Current (DC) measurements were performed at room temperature using a two-probe method with a Keithley SourceMeter 2400 and the positive bias defined for current flowing from the top to the bottom electrode. High resistivity samples were measured with a Keithley PicoamMeter 487 in the planar configuration.

'A THOUGH PATH'

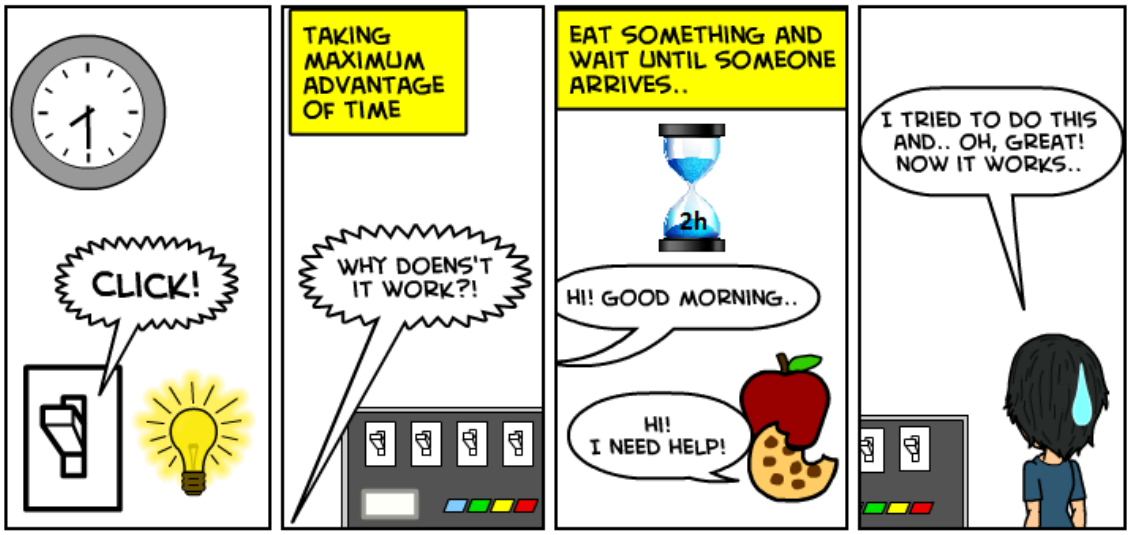

Chapter 3

Fabrication of Ag_2S thin films

3.1 Introduction

Aiming to the intended silver sulfide stoichiometry (Ag-rich Ag_2S), several fabrication methods (both physical and chemical) were followed: electrodeposition, ion beam deposition (IBD) from an Ag_2S target and the controlled annealing of Ag thin films in a sulfur atmosphere. The structural, morphological and chemical characterization of the produced samples, as well as their complementary fabrication for transport measurements are here described. The information bearing Ag/S atomic ratio in silver sulfide was obtained from chemical data.

3.2 Ion Beam Deposited Samples

Ion beam deposition (IBD) was used to fabricate Ag_2S thin films (both from an Ag target or directly from an Ag_2S target) and metal/Ag_2S/metal stacks.

Ag_2S thin films deposited on glass have a poor crystallinity but a 50 nm layer still shows the presence of the less conductive Ag_2S crystalline structure (acanthite) at 34.45º [(-121) direction; Fig. 18(a)]. Also visible is a broad bump between 25º and 35º attributed to the glass substrate. For higher film thickness [81 nm; Fig. 18(b)] the 38.15º Ag peak [(111) direction; mean size of the crystalline domains $\sim 2.2 \times 10^2$ Å] stands, but no clear Ag_2S preferential growth direction is observed. On the other hand, Ag films deposited using IBD are crystalline on top of glass, Ru, Al and W underlayers [Figs. 18(c)-(f)], although with the crystallinity clearly decreasing with decreasing film thickness. For the same Ag thickness (15 nm), the quality of the sample is worse on top of 200 nm Al [Fig. 18(e)] than 10 nm Ru [Fig. 18(d)], despite the overlap with the 38.08º Ru peak [(211) direction], as demonstrated by the higher noise in the first case. Using a 200 nm W underlayer the cristallinity improves but the 38.07º [(002) direction;] and 39.60º [(111) direction; mean size $\sim$ 78 Å] W peaks stand out. The mean size of the crystalline domains was calculated using Eq. 20 and assuming 0.94 for the dimensionless shape factor.

The morphology and composition of the produced IBD samples was also probed using SEM and EDS. The Ag/S atomic percentage ratio in these samples was found to depend on the history of the Ag_2S target (Fig. 19). The stoichiometry of the target starts by being close to 2 of Ag_2S but then increases over time life and remains in an erratic behavior above the ideal. This was expected, since S is highly volatile and Ag in Ag_2S is extremely mobile to redistribute over the surface after each deposition. Therefore, we are not able to produce reproducible Ag_2S thin films and an alternative method to achieve the correct compensation is needed.

The SEM analysis of the morphology of the samples shows that the films deposited from the Ag_2S target have grains at the surface. In the first deposited sample (2.49 Ag/S ratio) these grains are larger and more spaced [Fig. 20(a)], whereas in the second sample (7.68 Ag/S ratio) some change occurred to the target so that, for the same deposition and analysis conditions, the grains are smaller and closer distributed on the surface [Fig. 20(b)]. In the first case, a grain diameter up to 1.5 μm was found, decreasing to 0.5 μm for the second case. The average grain-size was estimated using the ImageJ software and the average radius of 10 random grains in each sample. From the contrast in the BSED image shown in Fig. 20(b) we conclude that the elements in the grains have higher atomic number than the ones on the bottom surface (since they are brighter), which means they are Ag-rich and justify the Ag/S ratio given by EDS analysis. Note also that S is so volatile and Ag so mobile that the attempt to take an EDS spectra of the grains created holes, as highlighted in Fig. 20(a).

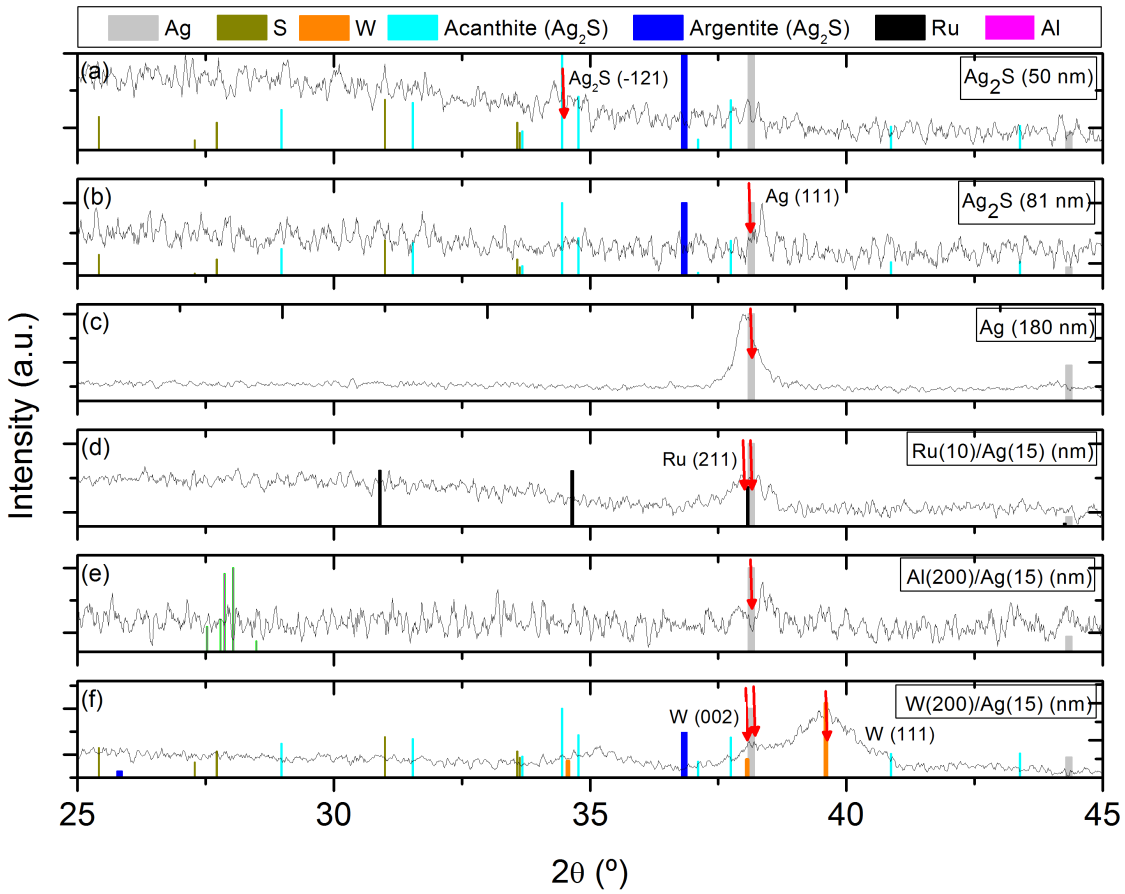

Figure 18: XRD spectra of IBD deposited Ag and Ag_2S samples.

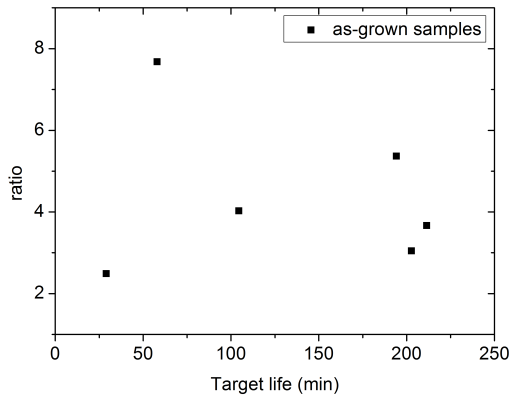

Figure 19: Ag/S % atomic ratio for the samples deposited using IBD from an Ag_2S target at different times.

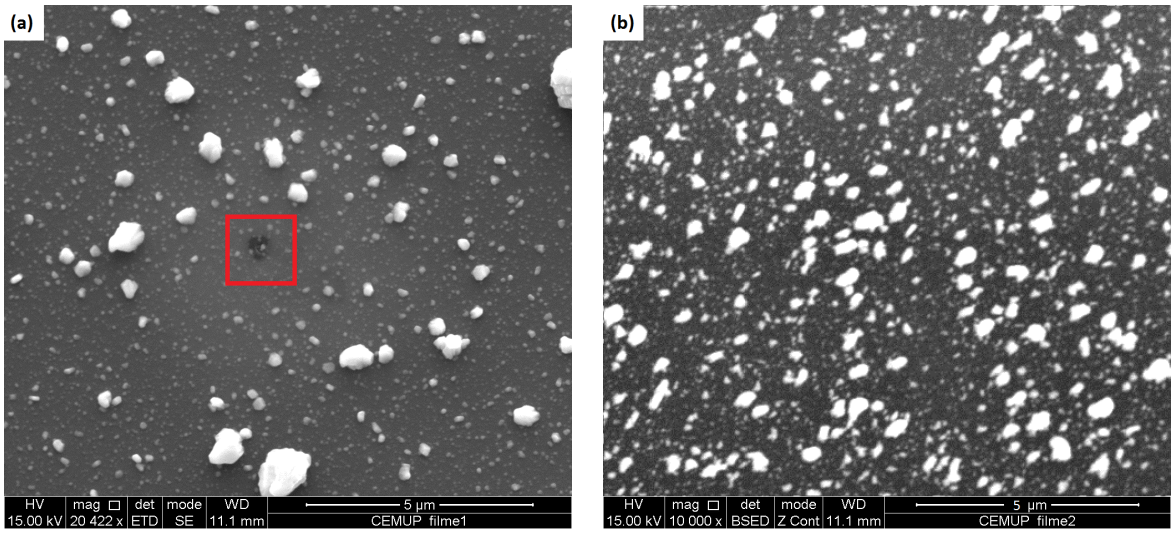

Figure 20: SEM images of the first two IBD samples from the Ag_2S target (a) first (50 nm; the red square highlights the hole left by the inspection) and (b) BSED image of the second Ag_2S (50 nm) sample.

The ion beam deposited samples from the Ag_2S target present a Raman active mode at 244 cm^{-1} [Fig. 21(a)], which was previously reported to be related with Ag_2S (Ag-S stretching modes) [21, 22]. Note that, without a fit, the Raman active mode appears to be at a smaller wavelength due to the overlap with the central peak and the sum of these damped harmonic oscillators contributions. No Ag or S Raman modes were detected. Furthermore, the measurement at higher laser power (38 mW) on these ion beam deposited samples induced no changes in the sample spectra, as seen in Fig. 21(b), indicating that the compound is highly stable. The data analysis of the bands was performed using the Igor software.

The FTIR - ATR technique was also used in the attempt to inquire the existence of chemical bonds between silver and sulfur on these samples. As the inset of Fig. 21(a) reveals, the only absorption peaks measured may be associated with the glass substrate, but we do not know its chemical composition to correctly classify the bands. This difficulty in measuring the Ag_2S absorption may be due to the reduced thickness of the film, making the glass highly noticeable.

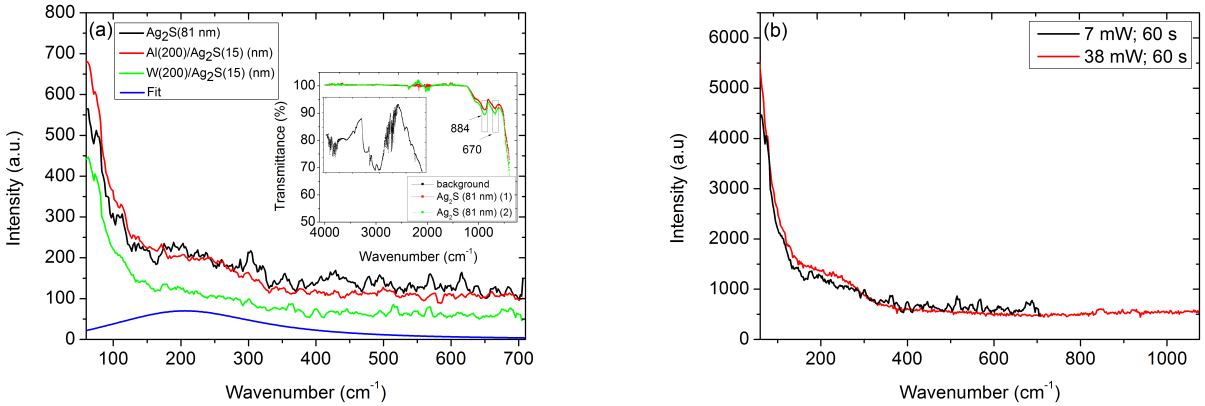

Figure 21: Raman analysis of (a) three Ag_2S ion beam deposited samples measured at 7 mW for 60 s (inset shows the FTIR analysis of a 81 nm Ag_2S sample) and (b) 15 nm of Ag_2S on top of 200 nm of W measured at 7 mW and 38 mW.

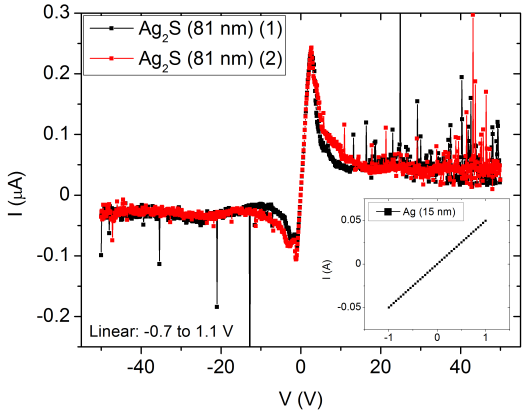

Figure 22: Conductivity (current - voltage) measurements of ion beam deposited Ag_2S samples (inset shows the measurement of Ag sample).

Transport measurements using the two point contact method where performed to estimate the Ag and Ag_2S resistivities. The inset of Fig. 22 shows the expected linear behavior with high conductivity of the 15 nm Ag film, indicative of its metallic nature, and the much lower conductivity of the 81 nm Ag_2S film (4.03 Ag/S ratio). Using the linear range of both measurements, the calculated resistivities are 30 μΩcm and 70 Ωcm for Ag and Ag_2S, respectively. Essentially, this Ag_2S film is 10^6 times more resistive than Ag, even though it is Ag-rich. The value of the Ag_2S resistivity is in agreement with those reported for acanthite (between 10^{-1} and 10^3 Ωcm [19, 60]) and is much higher than that of argentite ($10^{-4} - 10^{-1}$ Ωcm [61]). The obtained Ag resistivity is one order of magnitude higher than the 1.6 μΩcm [62] reported in the literature for bulk samples, since it is in a thin film form. The exponential decaying behavior observed for the Ag_2S sample after the linear range is reproducible, although no reasonable explanation was found.

3.3 Sulfurizations

Since the Ag/S ratio of the Ag_2S target depends on its history, thermal annealings were explored to compensate the S variation and achieve the ideal ratio. Annealing of Ag thin film in a S atmosphere were also performed aiming this goal. Several series of annealings of 15 nm Ag and 15 nm Ag_2S on top of 200 nm Al or W thin films were performed in a constant volume sulfur atmosphere and on vacuum atmosphere.

The XRD spectra of the annealed samples indicates a lack of diffraction peaks and thus that they are either amorphous or nanocrystalline (Fig. 23). From Fig. 23(a) we can see that the annealing in a vacuum atmosphere (without sulfur) at 180° of the 15 nm Ag_2S sample does not provide a preferential direction for Ag_2S. The 38.15° Ag peak [(111) direction] seems to only slightly appear in Fig. 23(b), as well as the 31.54° Ag_2S peak [(-112) direction], which is a sample deposited from the Ag_2S target. The annealing of Ag (15 nm) on top of Al (200 nm) or W (200 nm) also results in non-crystalline samples, independently of the annealing time, as shown in Figs. 23(c) and (d).

The EDS analysis reveals that, for both 15 nm Ag [Fig. 24(a)] and 15 nm Ag_2S samples [Fig. 24(b)], the final Ag/S atomic percentage ratio is inversely proportional to the annealing temperature, having a higher dependence for Ag films than for Ag_2S ones, but mainly independent on the time. In both cases, these trends already develop below the desired ratio, i.e. the produced samples are always S-rich and show the high Ag-S diffusion particularly for the pure Ag samples.

The SEM images of the Al(200)/Ag(15) (nm) annealed samples show a granular surface with round grains

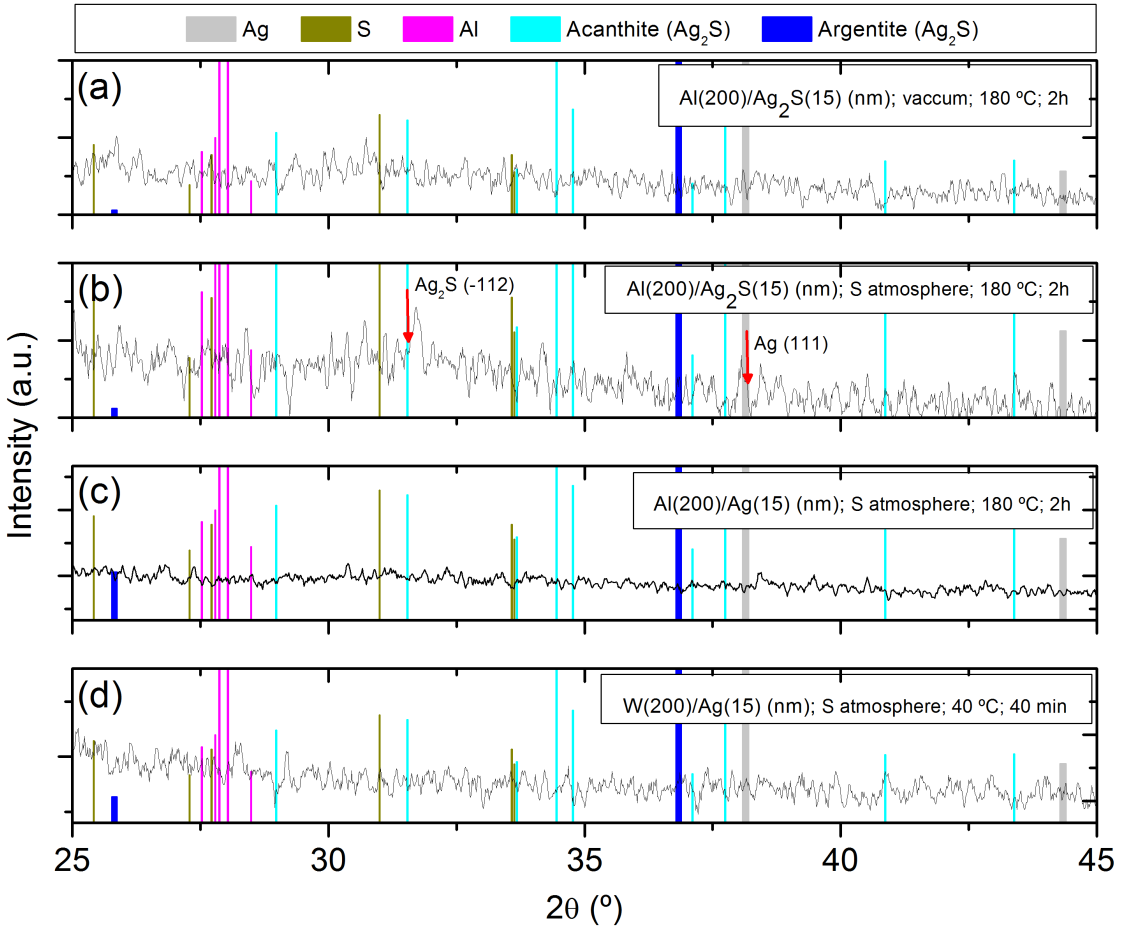

Figure 23: XRD spectra of the annealed samples (the caption indicates the annealing conditions).

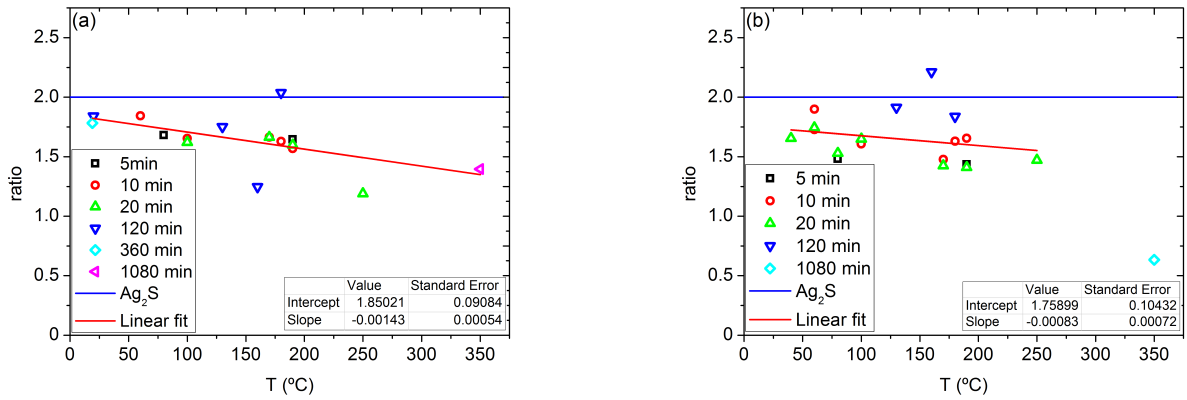

Figure 24: Ag/S % atomic ratio for the (a) 15 nm Ag and (b) 15 nm Ag_2S annealed samples.

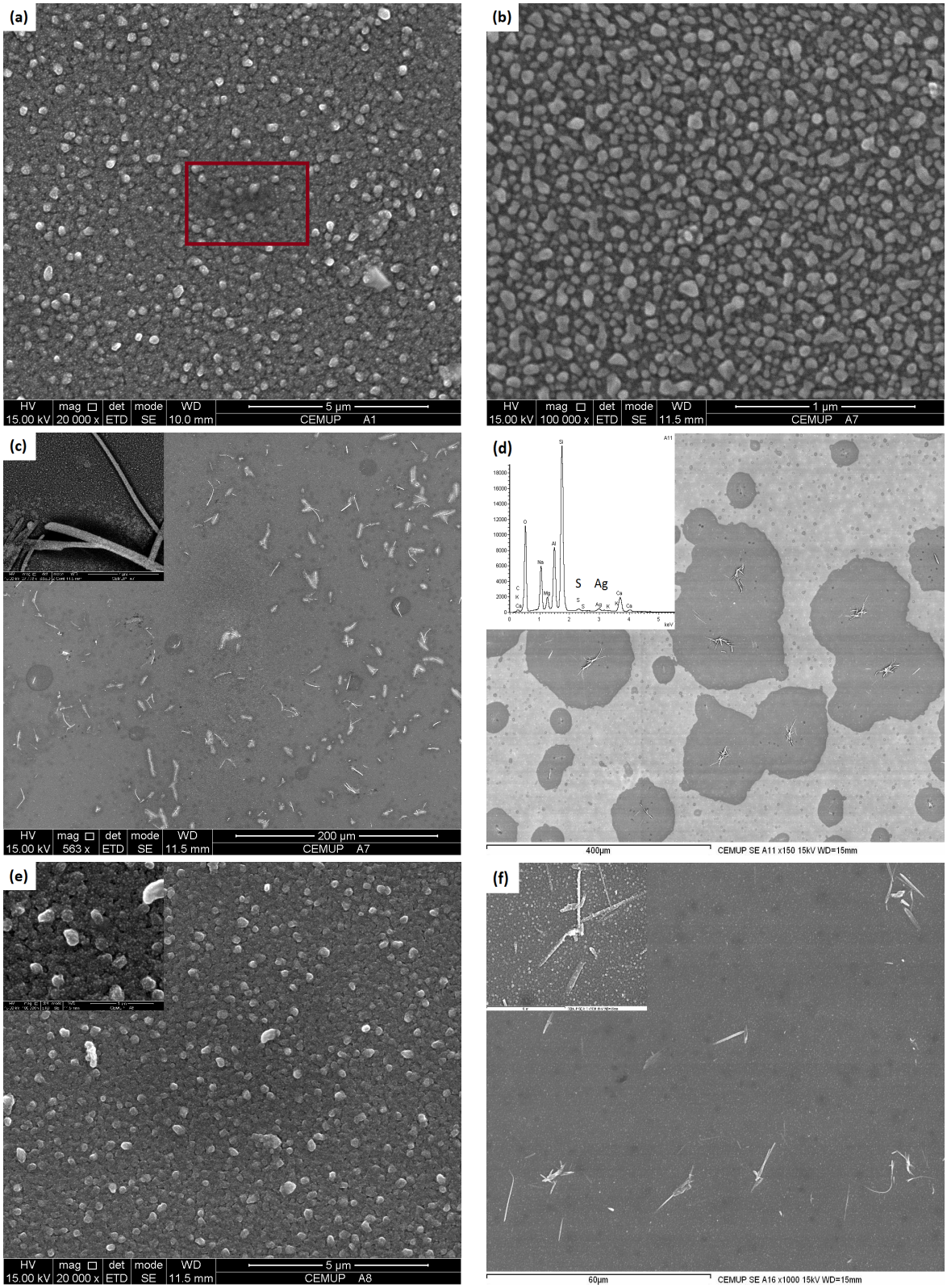

Figure 25: SEM images of the Al(200)/Ag(15) (nm) samples annealed in sulfur atmosphere at (a) 180 °C for 2h (the red square highlights a hole left by the inspection), (b) and (c) 250 °C for 20 min at different magnifications and (d) 350 °C for 18h, and of the Al(200)/Ag_2S (15) (nm) samples annealed in sulfur atmosphere at (e) 250 °C for 20 min and (f) 130 °C for 2h.

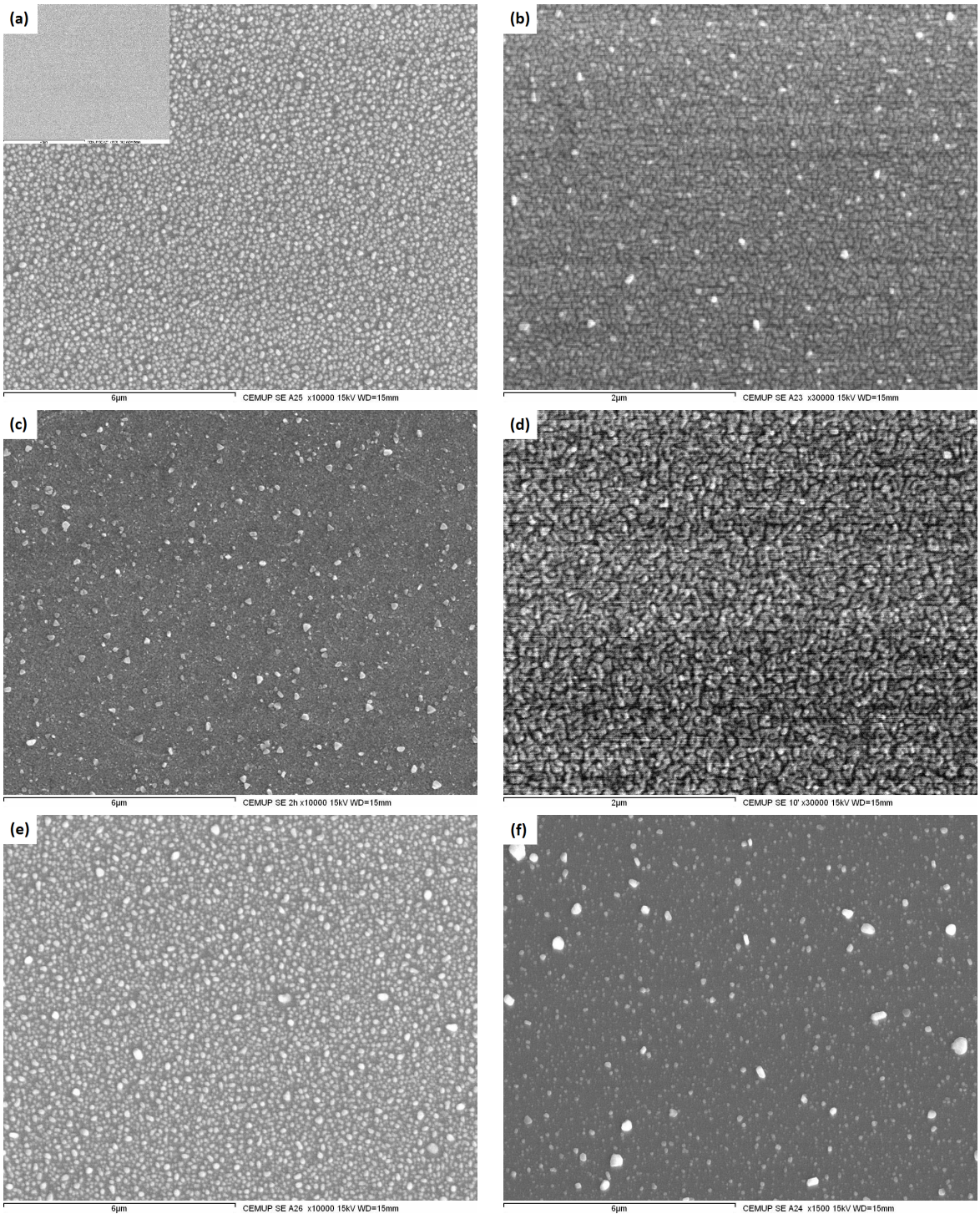

Figure 26: SEM images of the W(200)/Ag(15) (nm) samples annealed in sulfur atmosphere at (a) 190 °C for 10 min and (b) 80 °C for 10 min. Same analysis for an Ag film in direct contact with sulfur powder at room temperature for (c) 2h and (d) 10 min, and of the W(200)/Ag_2S(15) (nm) samples annealed in sulfur atmosphere at (e) 190 °C for 10 min and (f) 80 °C for 10 min.

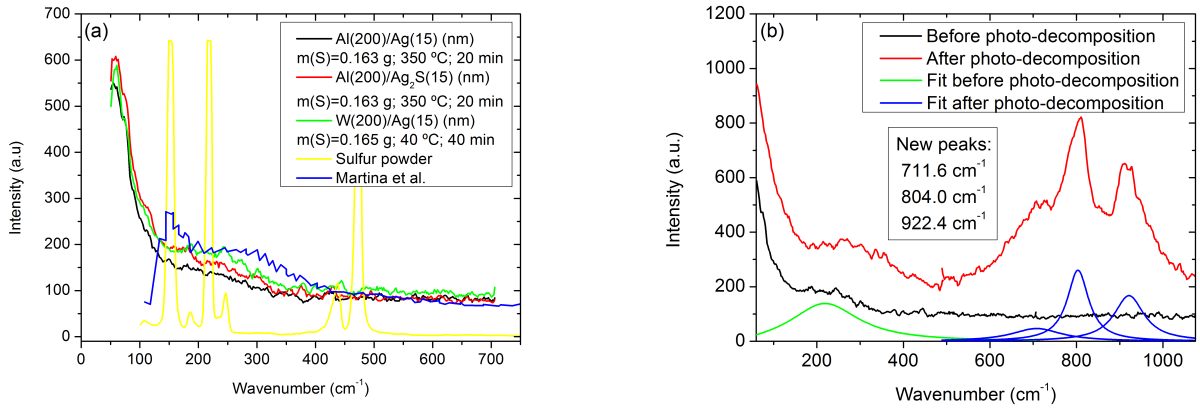

Figure 27: (a) Raman spectra of the annealed samples, including the S powder spectrum and the data from Martina *et al.* [21, 22]. (b) Photo-decomposition of one Ag_2S annealed sample (7 mW; 60 s).

of sizes up to 0.3 μm and 0.1 μm [Figs. 25(a) and (b), respectively] which result in a rough surface. Maybe related with time or temperature, the sample in Fig. 25(a) has a whole granular surface, while in Fig. 25(b) the background seems barely granular. Other samples also present sharp grains (not shown) or needles aggregates on the surface [Fig. 25(c)], with a composition similar to that of the film below, both containing Ag and S. Furthermore, many odd shaped undefined impurities are present and in some cases an odd appearance is revealed [Fig. 25(d)], maybe due to the high annealing temperature and/or time, although the EDS analysis of the two regions give the same elements with roughly the same concentrations. The Al(200)/Ag_2S(15) (nm) annealed samples also show a non-uniform granular surface with grain sizes up to 0.3 μm [Fig. 25(e)]. Once again, needles [Fig. 25(f)] and odd appearance are seen (not shown).

Using a W (200 nm) layer as buffer significantly improved the quality of the surface of the produced samples, as can be seen by comparing Figs. 25 and 26. The surfaces appear smoother with grain sizes up to 0.15 μm [Fig. 26(a)]. For ten minutes annealing, higher temperatures lead to rounder and bigger grains [190 ºC; Fig. 26(a)] than lower ones [80 ºC; Fig. 26(b)]. The SEM analysis also showed that the simple contact of an Ag (15 nm) layer with S powder at room temperature and normal pressure unleashes a reaction between Ag and S that results in the formation of Ag_2S with bigger grains at the surface [Fig. 26(c)]. In fact, as shown in Fig. 26(d), a surface appearance quite similar to that of the annealed sample in Fig. 26(b) is visible. Again, for Ag_2S (15 nm) samples the surface quality improves when a bottom W(200 nm) ion beam deposited layer is used [compare Figs. 25(e) and (f) with 26(e) and (f)]. For the same annealing time, the concentration of grains on the surface is higher at the higher temperature of 190 ºC [Fig. 26(e)]. For this annealing temperature they are also rounder and more homogeneously distributed than at 80 ºC [Fig. 26(f)].

The Raman spectroscopy analysis again revealed the presence of an Ag_2S Raman active mode at around 239 cm^{-1}(Ag-S stretching mode [21]), approximately the same value as for the Ag_2S ion beam deposited samples, in the Al(200)/Ag_2S(15), Al(200)/Ag(15) and W(200)/Ag(15) (nm) annealed samples, but not for the W(200)/Ag_2S(15) (nm) one [Fig. 27(a)]. It is not clear why this occurred but further studies are underway. Nevertheless, a chemical change was achieved, since Ag has no Raman spectrum and the existent bands are not those of S alone (S_8). One further observed the reported photosensitivity of Ag_2S [21, 22] above a certain laser power value (27 mW in our case), by the appearance of new active modes at 400 cm^{-1}, 712 cm^{-1}, 804 $cm^{-1}$and 922 cm^{-1} [Fig. 27(b)]. This phenomenon is irreversible, as measurements at lower laser power after the photo-decomposition still evidence the new bands, indicating the formation of a new compound and showing that the annealed sample is not as stable as the ion beam deposited Ag_2S. This data does not give information

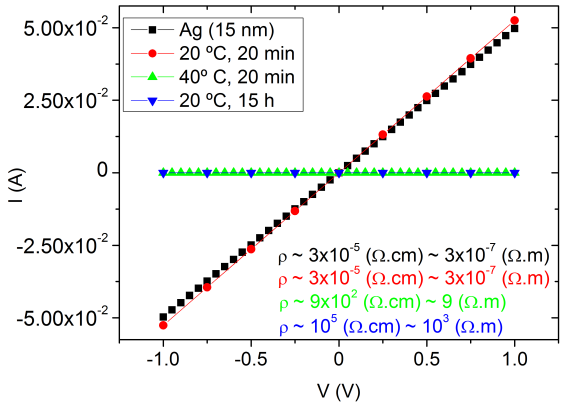

Figure 28: Conductivity measurements of 15 nm Ag annealed samples (glass only).

to classify the new compound and other measurements will be undertaken.

A study on the room temperature conductivity dependence on the annealing temperature was also performed with a 15 nm Ag ion beam deposited film on top of a glass substrate [Fig. 28]. The resistivity of the film remains basically the same after annealing for 20 min at 20 °C (3×10^{-5} Ωcm). An increase of seven orders of magnitude (to 9×10^{2} Ωcm) occurs after one annealing for 20 min at 40 °C. Annealing at room temperature for long times (15 h) resulted in a a highly resistive (10^{5} Ωcm) sample. Kundu *et al.*, reported that the sulfurization of an Ag-rich Ag_2S film resulted in a S-rich film and caused an increase in the resistivity of four orders of magnitude (to $10^{7} - 10^{8}$ Ωcm) [50].

3.4 Electrodeposition and Chemical Routes

As the electrodeposition of thin films is a rather simple and available technique, attempts were performed to use it to obtain Ag_2S thin films. To deposit films of silver sulfide we then explored a non-aqueous DMSO solution containing $AgNO_3$ and elemental S [57]. The graph in Fig. 29(a) shows the electrodeposition curves (current versus time) under different applied constant voltages. The atypical behavior observed indicates that the electrodeposition of Ag_2S on a Cu tape substrate using this solution did not occur. The resulting four samples (two for -0.8 V, one for -0.6 V and other for -0.4 V) showed instead that a reaction between the solution and the Cu tape took place. This was confirmed by just submerging the tape in the $AgNO_3$+S+DMSO solution under zero applied voltage, that led to a change of the Cu tape color (from brown to black), unlike the submersion in DMSO only. Figure 29(b) shows the rough Cu tape surface with some deposits on top, indicating that a chemical reaction is occurring by just submerging the sample on the DMSO + S + $AgNO_3$ solution at room temperature. The S in the solution is likely to be reacting with the Cu to form a copper sulfide compound.

Electrodeposition was then set aside and a solution of DMSO + S only was used to dip Ag and Ag_2S thin film samples, since the $AgNO_3$ appeared to be all precipitated. After the initial tests using a Cu tape, we used Ag_2S(50), Ag (180) and Ru/Ag(15) (nm) to perform a study on the influence of time (t), temperature (T), and sulfur concentration (c_S) on the Ag/S atomic percentage ratio of the dipped films. The Ru bottom layer was needed because the Ag layer lifted from the glass substrate when cleaned under running water at the end of the process.

X-ray diffraction (XRD) measurements were performed to determine the composition and crystallographic structure of the samples. The dipped Ag samples were found to be crystalline [Fig. 30(a)-(c)]. For a small

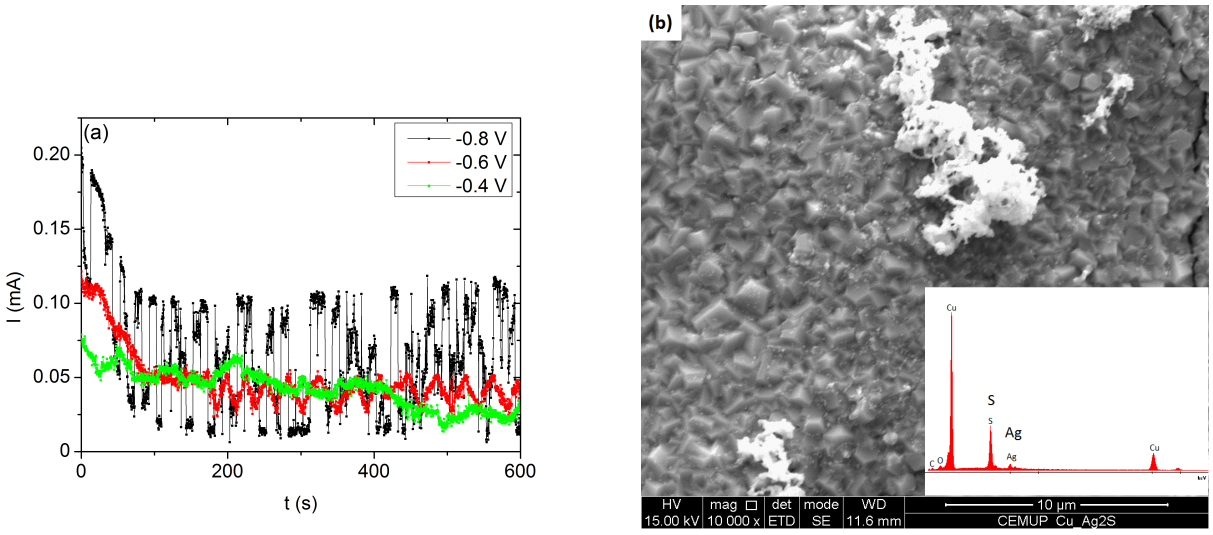

Figure 29: (a) Current - time curves measured during the attempted electrodepositions under applied voltages of -0.8 V, -0.6 V and -0.4 V. (b) SEM image of the Cu tape dipped in DMSO(10mL) + S + $AgNO_3$ + S for 10 min (inset: EDS analysis).

time in the solution [10 s; Fig. 30(a)], the XRD spectrum resembles that of pure Ag [Fig. 18(b)]. As time increases, the 38.15° Ag peak [(111) direction; mean size $\sim$ 2.6x10^2 Å] starts to vanish and a peak at 37.75° attributed to Ag_2S in its most insulating form [acanthite; (-103) direction; mean size $\sim 3.4 \times 10^2$ Å] starts to appear [Fig. 30(b)]. We can see that, with 75 s dipping time [Fig. 30(c)], the 38.15° Ag peak does not completely disappear. However, for higher dipping times the 180 nm Ag layer it lifts from the glass substrate as mentioned, indicating a poor adherence of Ag_2S to glass buffer layers when fabricated using this method. For 75 s and 5 min the 31.54° Ag_2S (acanthite) peak [(-112) direction; mean size $\sim 9.4 \times 10^2$ Å] is noticeable [Figs. 30(b) and (c), respectively]. This indicates the continuous growth of an Ag_2S layer with the progressive vanishing of metallic Ag. However, with a Ru bottom electrode [Figs. 30(d)-(f)] the observed crystallinity of the initial sample is lost after dipping in the solution, as can be seen by comparing with Fig. 18(d) and noticing the disappearance of the 38.15° Ag peak.

EDS was also performed to obtain the variation of the Ag/S atomic percentage ratio with the studied parameters. Relatively to the dipping time, Fig. 31 clearly shows that the concentration of S increases with time, revealing that the reaction continues after the Ag_2S stoichiometry is reached and showing that, for a thinner Ag (15 nm) layer, the process is faster [Fig. 31(a)]. The ratios obtained may explain the lack of peaks in the XRD spectra [Figs. 18(d)-(f)], since the Ag layer below is almost nonexistent [Fig. 31(b)]. As in the case of the Cu tape substrate, 50 nm Ag_2S samples submerged in the DMSO + S solution at temperatures around 80 °C show small needles at the surface on top of a smooth background [Figs. 32(a)], with an overall atomic percentage ratio close to the ideal one, as presented in Table 1. On the other hand, the samples with a Ru bottom layer present no grains at the surface [Figs. 32(b) and (c)], with a general ratio that depends on the dipping time, due to the continue chemical reaction between the 15 nm Ag layer and the S on the solution (see Table 1).

Although one is able to fine tune the S content using this method and achieve an Ag/S ratio close to the ideal, Ag adherence problems occur and bubbles appear after dipping in the solution, which makes microfabrication difficult, also due to the fact that these bubbles are non-stationary during lithography.

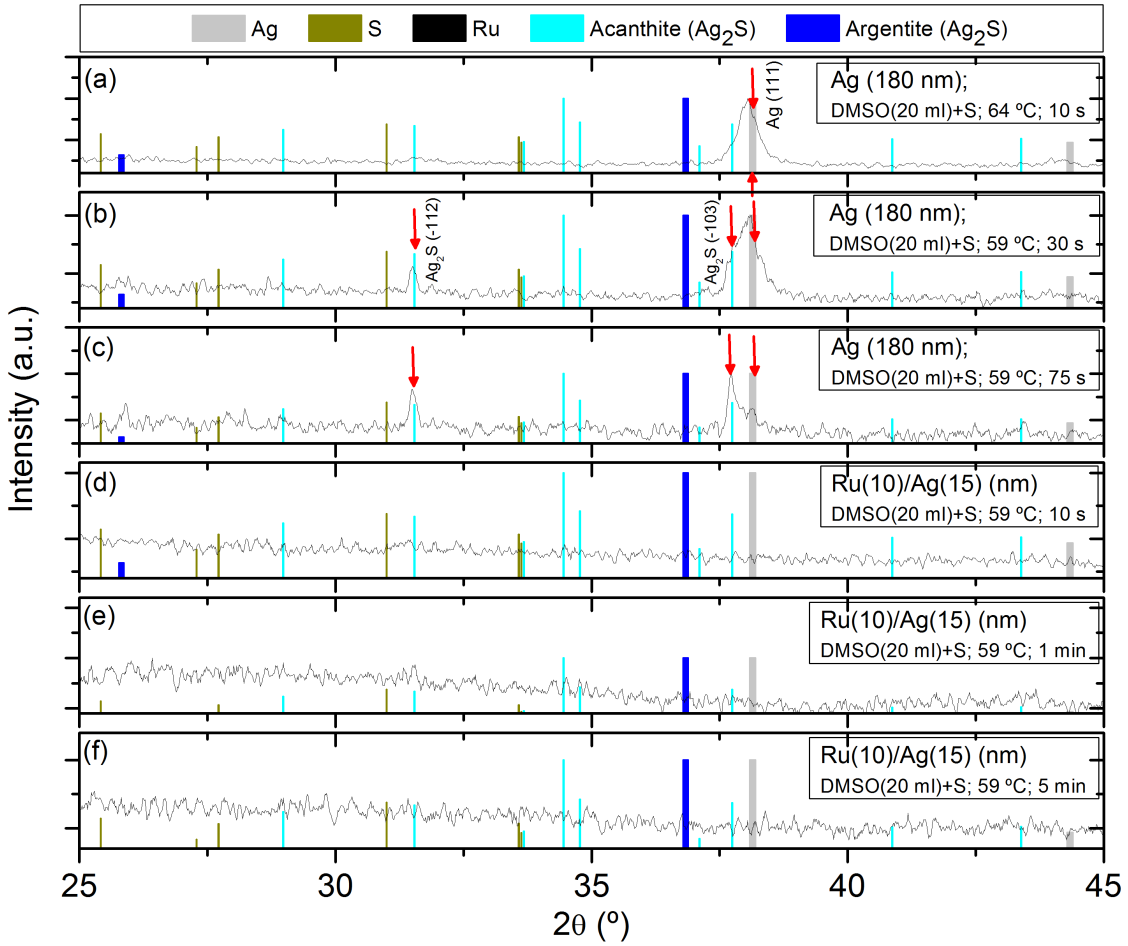

Figure 30: XRD spectra of the samples obtained after dipping an Ag film on DMSO (20 ml) + S (the caption indicates the dipping conditions).

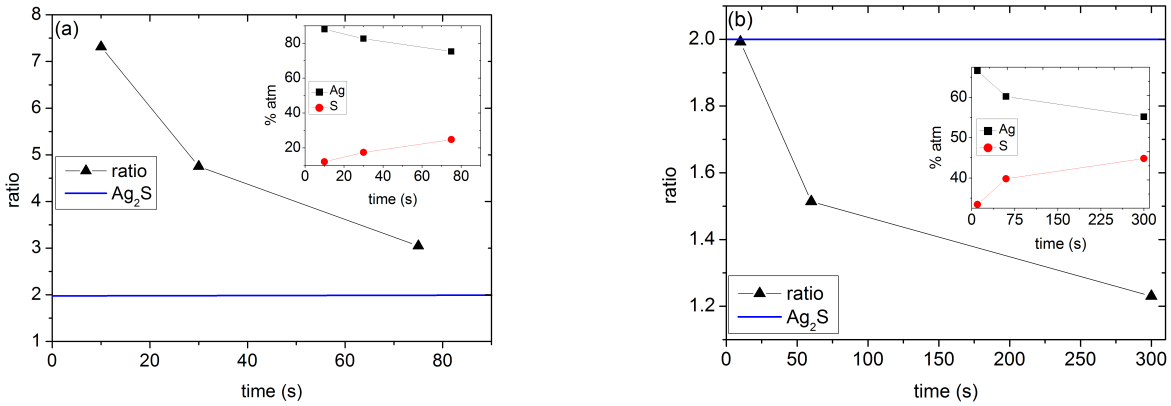

Figure 31: Dependence of the Ag/S atomic percentage ratio on the time the sample stays in the solution (inset shows the dependence of Ag and S atomic percentage on dipping time; the solid lines are guides to the eye) for (a) Ag (180 nm) and (b) Ru(10)/Ag (15) (nm) samples.

Sample	t (s)	T (°C)	DMSO V (ml)	c_S (mol l^{-1})	Ag (% atm)	S (% atm)	ratio
Cu tape	600		10	0.19			0.11
Cu tape	600	51	10	0.19			0.14
Cu tape		81	10	0.19	68.79	31.21	2.20
Ag_2S (50 nm)		81	10	0.19	67.14	32.86	2.04
Ag (180 nm)	10	64	20	0.095	87.97	12.03	7.31
Ag (180 nm)	30	59	20	0.095	82.61	17.39	4.75
Ag (180 nm)	75	59	20	0.095	75.28	24.72	3.05
Ru(10)/Ag(15) (nm)	10	55	20	0.095	66.58	33.42	1.99
Ru(10)/Ag(15) (nm)	60	59	20	0.095	60.22	39.78	1.51
Ru(10)/Ag(15) (nm)	300	59	20	0.095	55.16	44.84	1.23

Table 1: Dependence of the Ag and S atomic percentage and ratio on time (s), temperature (T), solution volume (DMSO V) and sulfur concentration (c_S) dipping conditions.

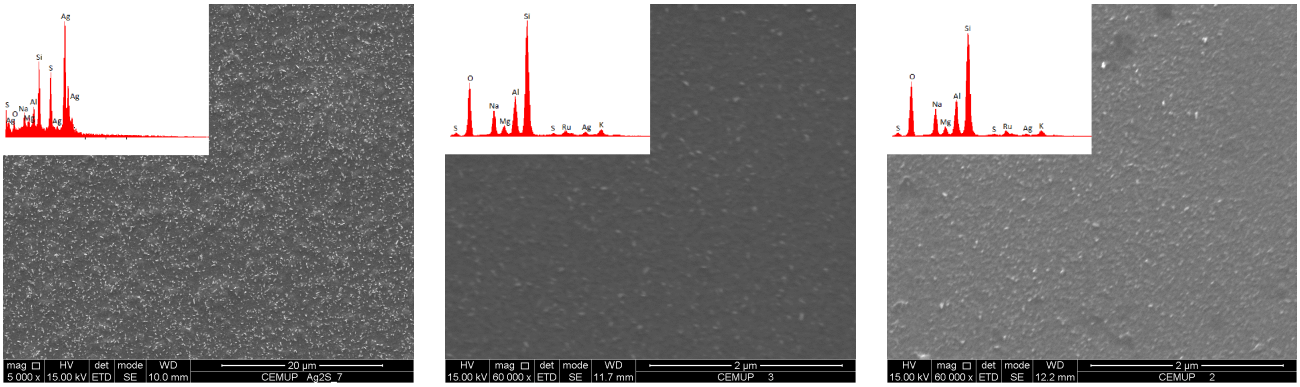

Figure 32: SEM images of the chemically obtained samples (a) Ag_2S (50 nm) in DMSO (10mL) + S at 82 °C, (b) Ru(10)/Ag(15) (nm) in DMSO (20mL) + S at 55 °C for 10 s and (c) Ru(10)/Ag(15) (nm) in DMSO (20mL) + S at 59 °C for 5 min.

3.5 Conclusions

In general, the XRD analysis showed the 38.15° Ag peak [(111) direction] for all the described methods but the preferential growth directions attributed to Ag_2S were less defined. The 34.45° Ag_2S peak [(-121) direction] was the one observed for the ion beam deposited samples, while annealed samples presented the 31.54° Ag_2S peak [(-112) direction]. The last one was also seen for chemical routes but the more noticeable was the 37.75° Ag_2S peak [(-103) direction] with increasing intensity for decreasing Ag peak.

The Ag/S atomic percentage ratio obtained from depositing from an Ag_2S target was above the ideal and uncontrollably dependent on the target life for the as-deposited samples. On the other hand, the annealed samples had a ratio below the ideal, inversely depending on the annealing temperature. The samples obtained through chemical routes present both above (for thicker films) and below (for thinner ones) the ideal Ag/S atomic percentage ratio and are inversely dependent on the dipping time. Therefore, saturation of the ratio was observed for the annealed samples, but not for the ones chemically obtained (Fig. 33).

The grain size of the ion beam deposited samples decreased from 1.5 μm to 0.5 μm with the Ag_2S target life, being the grains of the annealed samples no bigger than 0.3 μm. Samples dipped in the DMSO + S solution presented needles on top of a smooth surface, instead of a granular appearance.

A stable active Raman mode attributed to Ag_2S was also obtained at 244 cm^{-1} for the samples deposited

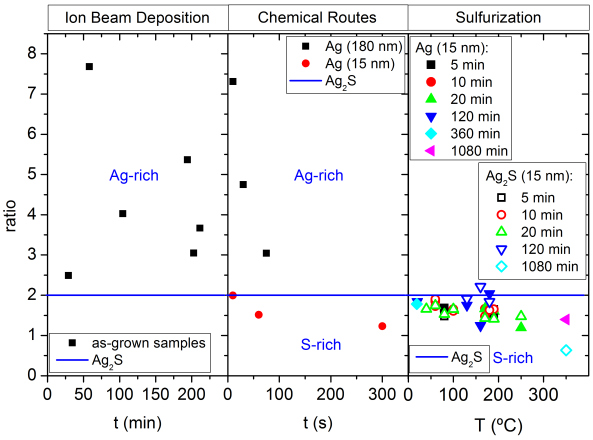

Figure 33: Dependence of the Ag/S atomic % ratio on the target life, dipping time and annealing temperature, for each followed process.

from the Ag_2S target, and at 239 cm^{-1} for the annealed one. However, the appearance of 400 cm^{-1}, 712 cm^{-1}, 804 cm^{-1} and 922 cm^{-1} new peaks at high laser power were seen for the latter.

'TRICKY MEASUREMENTS'

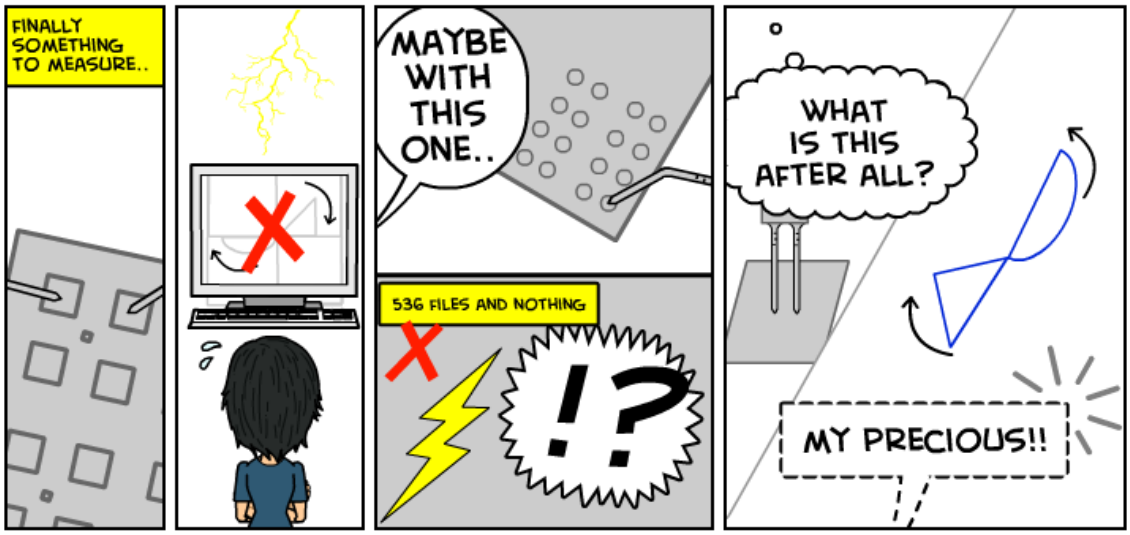

Chapter 4

Electrical characteristics of the $Ag_{2+\delta}S$ Thin Films

4.1 Resistive Switching Properties of Ion Beam Deposited Ag-rich Ag_2S thin films

4.1.1 Current - Voltage Characteristics

The Ag-rich (4.03 Ag/S ratio) ion beam deposited Ag_2S (81 nm) sample was measured in a planar configuration, allowing us to study the transport properties of the film deposited directly from the Ag_2S target without further treatments or lithography.

Resistive Switching. Figure 34(a) shows current-voltage characteristics of the mentioned sample by directly placing two POGO [25J-4; Ø = 41 μm] probe contacts on the thin film surface. With increasing voltage we initially see a linear increase of the current ($R_{ON} \sim 10^7\ \Omega$) until, above a threshold voltage of around 3 V, a negative differential resistance (NDR) region is observed. The device then switches to a higher resistance state ($R_{OFF} \sim 10^9\ \Omega$). The current continues decreasing as the voltage is decreased, passing through zero but revealing hysteresis. For negative voltage, again a linear behavior with approximately the same R_{ON} value ($10^7\ \Omega$) is observed, together with a NDR after -3 V. When the negative voltage is decreased the current also reveals a hysteretic behavior, being a clockwise non-self-crossing 8-loop. In fact, it is important to note that, when crossing zero voltage, there is a radical transition in the slope of the I(V) curve, with a change from the low ($3.8 \times 10^9\ \Omega$; at positive voltages) to the high ($1.6 \times 10^7\ \Omega$; at negative voltages) conductance states. This type of curve is usually called a type II memristor, similar to the I(V) curves of a thermistor [32]. There are very small variations between curves measured at different locations of the sample and, for voltages lower than 1 V, only a linear behavior without hysteresis is obtained. Plotting the same I(V) curve in a log-log scale [inset of Fig. 34(a)], an Ohmic conduction (0.97 slope) was obtained when the voltage increases from 0 V to 3.5 V (ON state), while space-charge-limited conduction (SCLC; 3.02 slope) was observed when decreasing

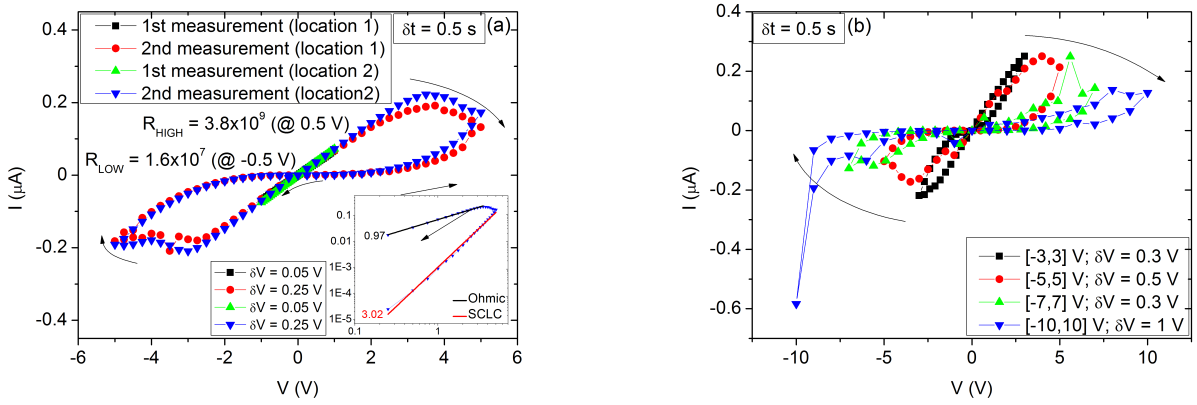

Figure 34: Current - voltage measurements of the 81 nm Ag_2S sample without contacts showing (a) an 8-loop (inset shows I(V) curves in a log-log scale) and (b) sample deterioration for successive measurements.

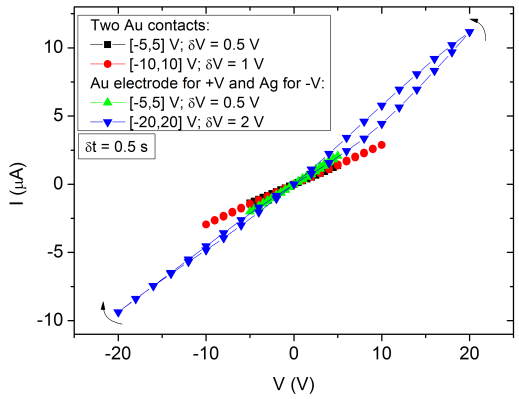

Figure 35: Current - voltage measurements of the 81 nm Ag_2S sample using Au and Ag electrical contacts. The legend shows the maximum positive and negative voltages used in each measurement, the voltage step of the cycle and the time delay.

the voltage from 5 V to 0 V (OFF state) [63]. The conduction mechanisms obtained for negative voltages are the same, Ohmic to the ON state and SCLC to the OFF state. As shown in Fig. 34(b) the sample simply deteriorates when probed directly with the POGO contacts (the 8-loop is lost on repetition).

Au and Ag electrical contacts were then used on top of the Ag_2S thin film. The 50 nm Au contacts were deposited by magnetron sputtering using a BOC Edwards Scancoat (IFIMUP), while the Ag contact was made using silver paint. A larger conductance is measured when two Au contacts are used. The resistance in this conditions is 10^6 Ω, being one order of magnitude smaller than that of the high conductance state measured directly with the POGO contacts. The measurements made with one Ag and one Au electrode (with positive bias defined as the current flowing from the Au to the Ag electrode) revealed the same conductive behavior as for two Au electrodes (Fig. 35). Small hysteresis appears only at very high voltages (about 20 V) with a self-crossing behavior.

With the voltage being applied between one Au or Ag electrode and one POGO probe electrode, both switching from low to high (set) and high to low (reset) conductive states were reproducibly achieved, as shown in Fig. 36(a). As the voltage is increased, the current remains small (around 10^8 Ω resistance), until it starts to rapidly increase at around 0.12 V [point 1 in Fig. 36(a)]. A linear decrease (with $R_{ON} \sim 10^6$ Ω) is then seen as the voltage is decreased. This linear high conductive behavior remains unchanged (point 2) until a negative voltage of around -0.17 V is reached, where an abrupt current decrease occurs (point 3; $R_{OFF} \sim 10^8$ Ω). The curve is now clockwise self-crossing, being denominated a type I memristor. The device presents bipolar resistive switching, since the set and reset voltages have opposite polarities. For higher voltage cycles the low current step before the set is less clear [upper inset of Fig. 36(a)]. The conduction is SCLC (2.47 slope) from 0 V to 0.1 V, then a continuous switching region (0.1 V - 0.25 V) is observed and then Ohmic conduction (1.03 slope) follows from 0.25 V to 0 V [lower inset of Fig. 36(a)]. For negative voltages the conduction remains Ohmic and then changes to SCLC after switching.

For higher maximum applied voltages, a new behavior is usually observed, depending on the polarity of the electrodes. In other words, a high conductive linear trend is always seen when the positive potential refers to the Au or Ag electrode [Fig. 36(b)]. This may indicate the formation of a metallic filament with a switching reset voltage near 0 V. This Ohmic behavior is independent of the polarity order of the cycle, i.e. whether it starts with positive or negative voltages both for Au and Ag. The inset of Figure 36(b) shows that for the same maximum applied positive voltage the conductivity of the linear behavior is slightly higher with a Ag

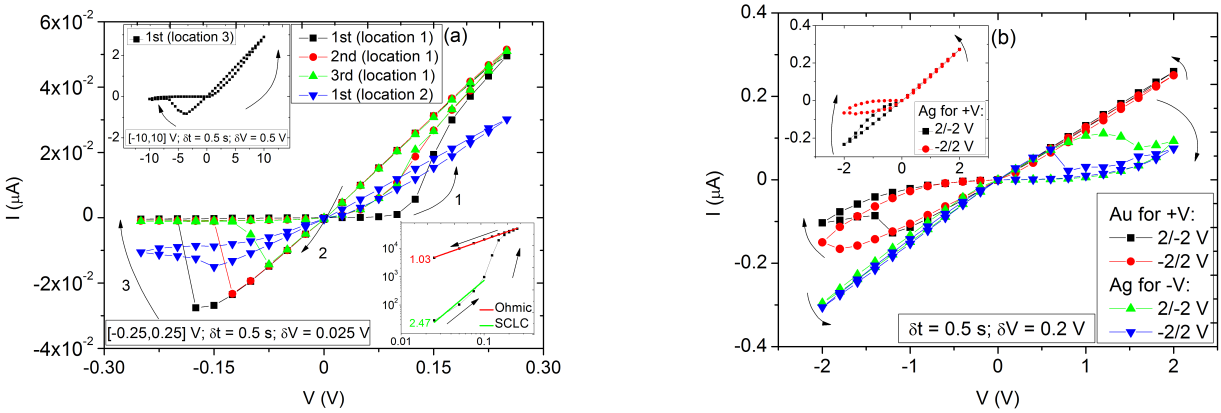

Figure 36: Current - voltage measurements of the 81 nm Ag_2S sample (a) showing both set and reset (the upper inset shows the same curve for higher voltage range; the lower inset shows I(V) in a log-log scale) and (b) one Au and Ag electrode at different sweep directions (the upper inset shows the higher conductivity of Ag than Au for the same polarity).

electrode than with a Au one, which may be attributed to the fact that the Ag work function (4.5 - 4.7 eV) is slightly smaller than that of Au (5.1 - 5.5 eV) [64].

A study on the impact of the maximum applied voltage on the switching properties of this sample was also performed. One observed that the maximum positive voltage that is reached imposes the minimum negative voltage that is necessary for reset [Fig. 37(a)]. A higher maximum positive voltage then difficults the current decrease for negative voltages, being the state formed at positive voltage better defined and presenting a larger area under the I(V) curve. The analysis of this dependency is presented in Fig. 37(b), revealing a linear relation with a 0.44 slope, i.e. the reset voltage is almost half the maximum positive voltage attained in each cycle.

For the same maximum positive voltage (1 V; Fig. 38) a lower positive voltage step, which means a higher cycling time applying less spaced consecutive voltages, also increases the negative voltage needed for reset. So, if one changes δV^+ from 0.1 V to 0.01 V, a *maximum* negative voltage of -1 V is not able to switch the

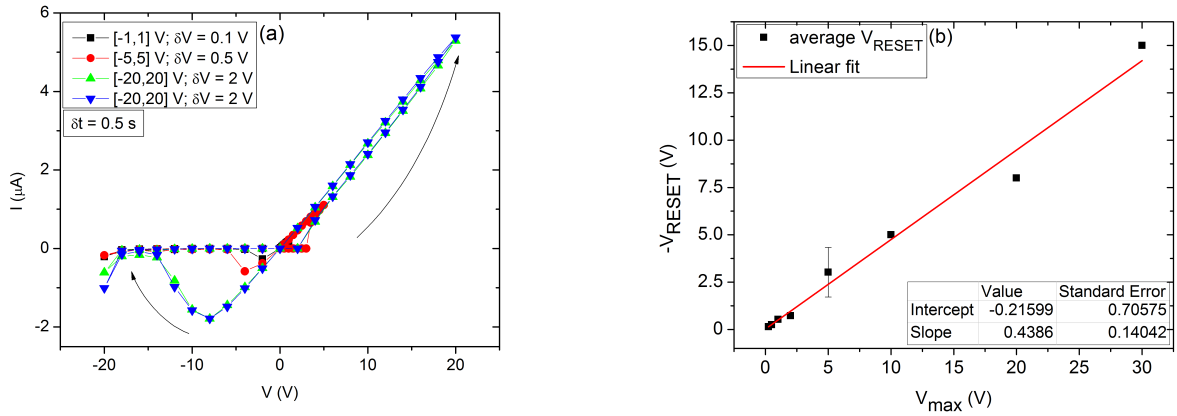

Figure 37: (a) Current - voltage measurements of the 81 nm Ag_2S sample with one Ag electrode at different voltage ranges and (b) reset voltage dependence on the maximum positive voltage.

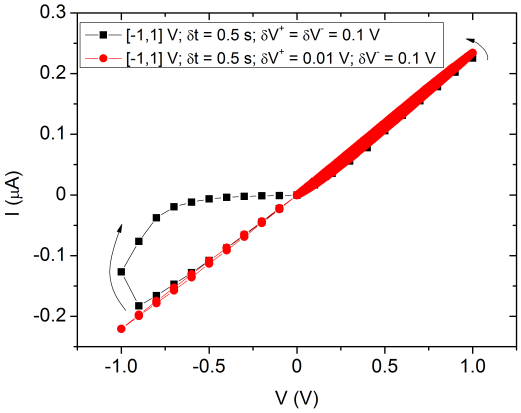

Figure 38: Current - voltage measurements of an Ag_2S sample with one Ag electrode with different positive voltage step.

sample to the high resistance state, as seen by the linear high conductive behavior at negative voltages. This phenomenon must be related with a device memory effect, as if the more it is stimulated (voltage pulses), the larger amount of charge flows through the device and the higher opposite voltage it requires to return to the initial state.

The constant low current state at positive voltage before set is not always observed, but (for the same delay time) it is more stable for cycles with higher voltage step [voltage range up to 1 V, or even 2.5 V; Figs. 39(a) and (b), respectively]. For such small voltage ranges the number of data points in the cycle does not vary much. If the number of data points is increased for the same voltage range (by changing the voltage step) the constant low current state will became smaller or even disappear because of the higher time the positive voltage is being applied. Although the voltage steps are small, the total flux flowing through the sample increases, making the switching to the high conductive state faster [Fig. 39(b)]. On the other hand, the reset process has always a slow-changing I(V) behavior.

Sometimes the repetition of cycles led to the expected degradation of the sample by maximum current decrease. Other times, however, one can see the reinforcement of the state formed at positive voltage, visible

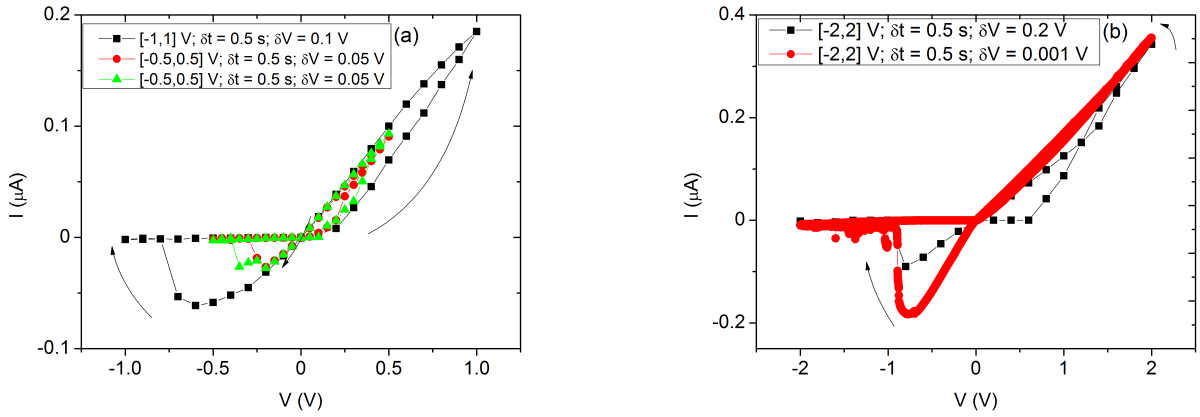

Figure 39: Current - voltage measurements of the 81 nm Ag_2S sample with one Ag electrode and a (a) constant step or (b) lower voltage step.

by the increase of the area under the negative curve with each cycle [Fig. 40(a)]. From the systematic study of several symmetric cycles with different voltage ranges, we estimated that (for 0.5 s delay) the minimum positive voltage to have non-negligible hysteresis with resistance variation when decreasing the voltage at the negative region is 0.2 V [Fig. 40(b)]. Also, the resistance of the two attainable states is highly reproducible, as shown in Fig. 41, with the set switching becoming more visible with the number of cycles measured.

Switching Voltage Statistical Distribution. Making the delay time constant (0.5 s), a systematic study on the reproducibility of the curves was performed with ten straight cycles measured under the same conditions for different voltage ranges (Fig. 42). There are no notorious changes for a maximum positive voltage of 0.5 V [Fig. 42(a)], and at maximum voltages of 10 V [Fig. 42(b)] there are only small (random) changes for negative voltages.

After hundreds of measurements (398), a Python program was developed to study the statistical distribution of the set and reset voltages when they could be determined [i.e. when a resistance switching ratio of at least 100 was observed; 116/398 with set and 110/398 with reset; Fig. 43(a)]. We observed that the majority of set voltages occur at 0.8/1 V and 2 V. The reset voltage is not so well defined since, as stated before, it depends on the maximum positive voltage. Decreasing the R_{ON}/R_{OFF} threshold to 10, Fig. 43(b) shows two Gaussian distributions, one at positive (set; centered at 0.8 V; 81/398) and the other at negative (reset; centered at -0.5 V; 15/398) voltages. Considering only the set voltage, Fig. 43(c) clearly shows the almost instantaneous set at the first positive voltage steps. Note that when the set occurs at the first pulse a set voltage cannot be measured, since we are not able to calculate a R_{ON}/R_{OFF} ratio due to the undefined resistance value at the origin.

Delay Time. Our study with different delay times (i.e. the time each voltage step is applied; varying from 0.1 s to 0.5 s) revealed that, for the same voltage range and voltage step, the higher the delay time, the higher the current obtained at maximum positive voltage [Fig. 44(a)]. This behavior reveals some kind of potentiation of the conductivity of the sample that is increased with the delay time. On the other hand, for the same voltage range and step, the set voltage tends to decrease with increasing delay time [Fig. 44(b)], showing that switching occurs at lower voltage for higher stimulation time [inset of Fig. 44(b)]. Our study for small delay times (from 0.1 to 0.7 s) revealed that already above 0.5 s the set voltage is near 0 V [inset of Fig. 44(b)]. Future studies on the statistical distribution of the set voltage on the delay time are planed.

Activity-Dependent Modifications. To try to observe activity-dependent modifications in the fabricated structure, in the search for common properties with long-term synaptic plasticity in neuromorphic systems, we successively applied half voltage cycles only (positive and then negative) for different maximum voltages. Figure 45 shows the observed activity-dependent modifications. As the maximum positive current continuously increases with each positive voltage cycle for $V_{max} = 10$ V, a potentiation of the connection for consecutive cycles is revealed. On the other hand, the maximum negative current continuously decreases with each negative voltage cycle, corresponding to a depression behavior. The increase of the current towards a constant value suggests the approach to the long-term-memory (LTM) stage of the device, similarly to the synaptic modifications that are dependent on the present synaptic weight where the approach to the limiting conductance is done asymptotically, as reported by Ohno *et al.* [52]. Also, the occurrence of larger steps at the initial voltage sweeps and smaller ones when the number of cycles increases (particularly for negative voltages) supports the idea that updates tend to become smaller as learning progresses.

Type II memristor. Finally, after many measurements, the sample started behaving like a type II memristor [Fig. 46], although with the same hysteresis at negative voltages and reset voltage dependence on maximum

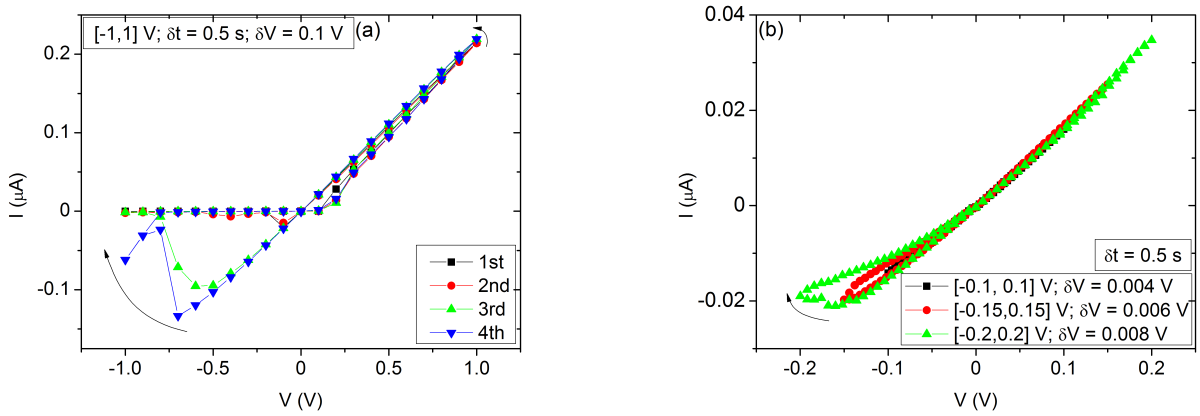

Figure 40: Current - voltage measurements of the 81 nm Ag_2S sample with one Ag electrode (a) showing consecutive area under negative curve increase and (b) minimum positive voltage for negative hysteresis.

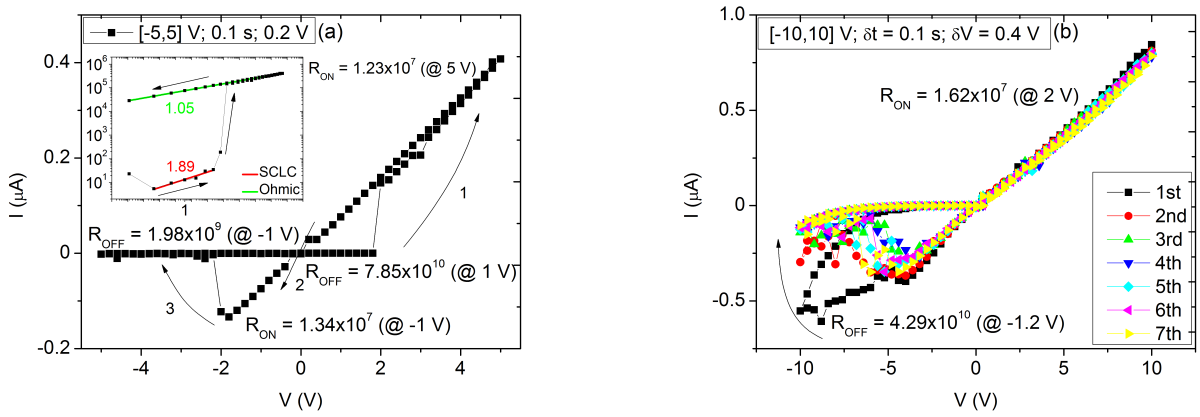

Figure 41: I(V) characteristics of a Ag_2S sample with one Ag electrode including the respective resistances for (a) a visible set (inset shows I(V) in a log-log scale) and (b) repeated measurements.

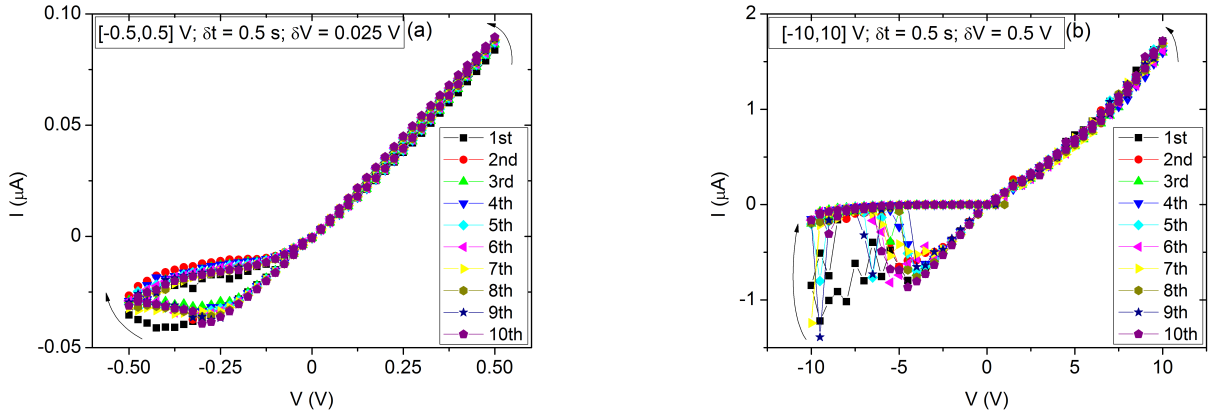

Figure 42: Ten repetition I(V) cycles with 0.5 s delay in the ranges (a) [-0.5, 0.5] V and (b) [-10, 10] V for the 81 nm Ag_2S sample.

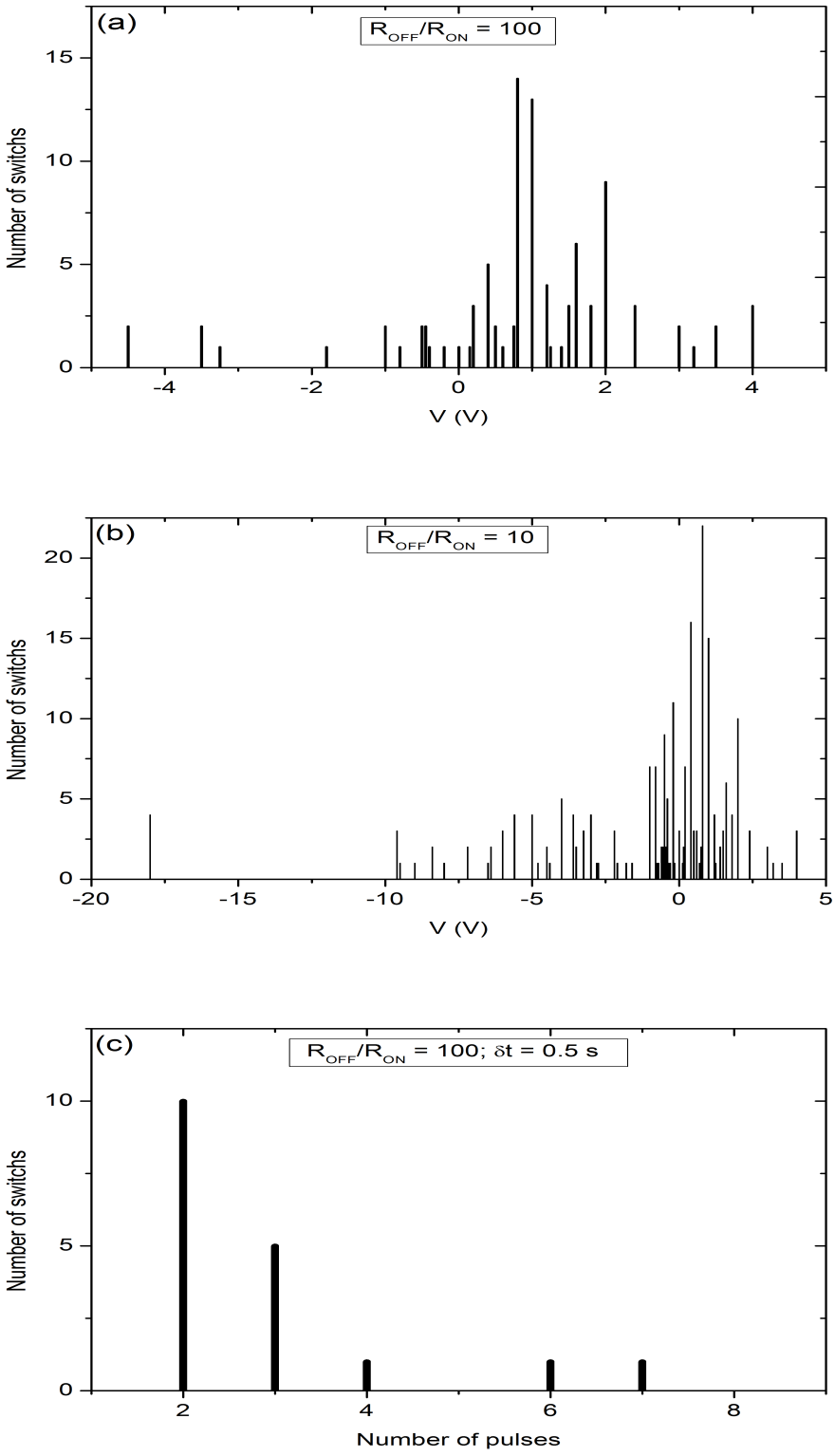

Figure 43: Statistical distribution of the number of switchings as a function of voltage for a resistance ratio of (a) 100, (b) 10 and (c) number of positive applied voltage pulses.

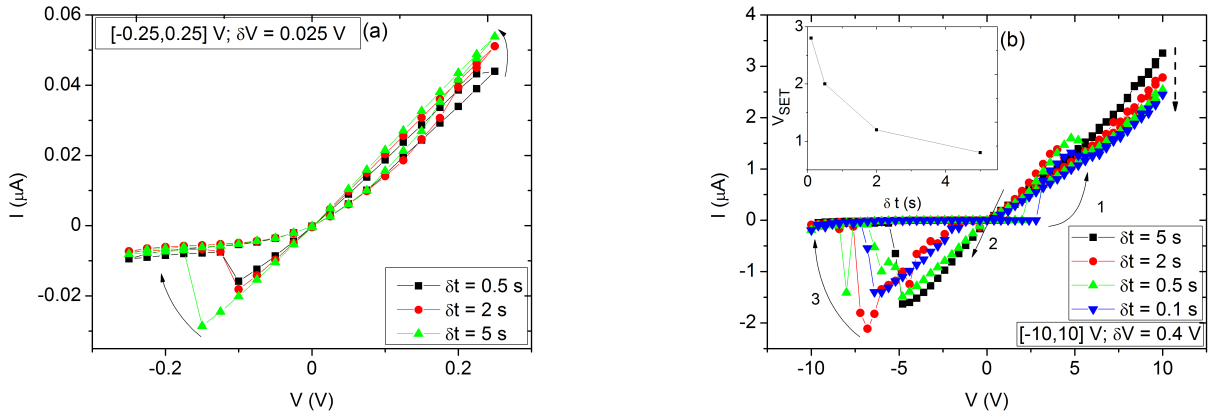

Figure 44: Dependence (a) of the maximum current at positive voltage and (b) of the set voltage on the delay time for the same voltage range and voltage step (inset shows the variation of the set voltage with the delay time; the lines in the inset are guides to the eye).

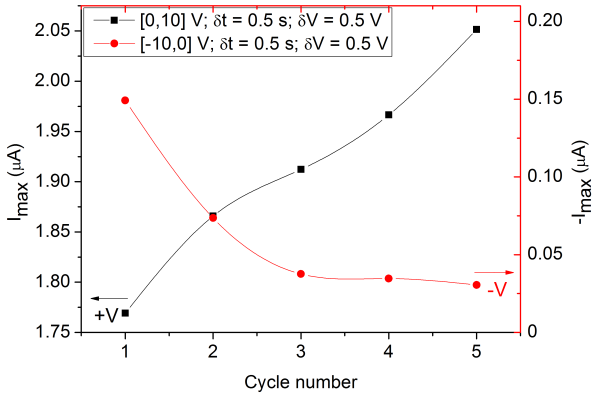

Figure 45: Dependence of the maximum current on the number of cycles on the 81 nm Ag_2S sample for five 10 V and -10 V repeated cycles (lines are just guides to the eye).

positive voltage, as shown in the inset of Fig. 46. Unfortunately, no physical explanation is yet known or discussed in the literature for such crossbar.

4.1.2 Time Dependent Studies

Applying a constant voltage over time allowed us to evaluate the stability of the sample state and to probe further possible activity-dependent modifications. One started by inducing the high resistance OFF state by applying negative sweeps. Then, applying a constant positive voltage of 1 V over time, the switching to the ON state is seen by a clear step as the one in Fig. 47(a). Figure 47(b) shows the current versus time curves obtained under smaller positive voltages. One mostly sees a constant increase of the current over time, indicating that a positive voltage leads to a decrease of the sample's resistance towards the R_{ON} value. One also sees that higher voltages lead to higher current values. Even though different voltage values are being applied, if one calculates the resistance after a constant current is reached, one obtains approximately the same value as reported above for the full I(V) cycles. Assuming the switching time as the time needed for the

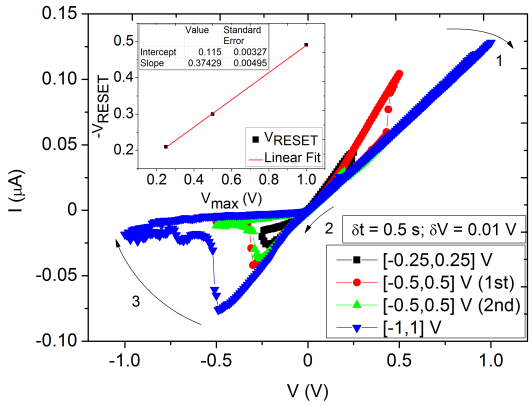

Figure 46: I(V) measurements showing the change to type II memristor of the Ag_2S sample (inset shows the dependence of the V_{RESET} on the maximum positive voltage applied).

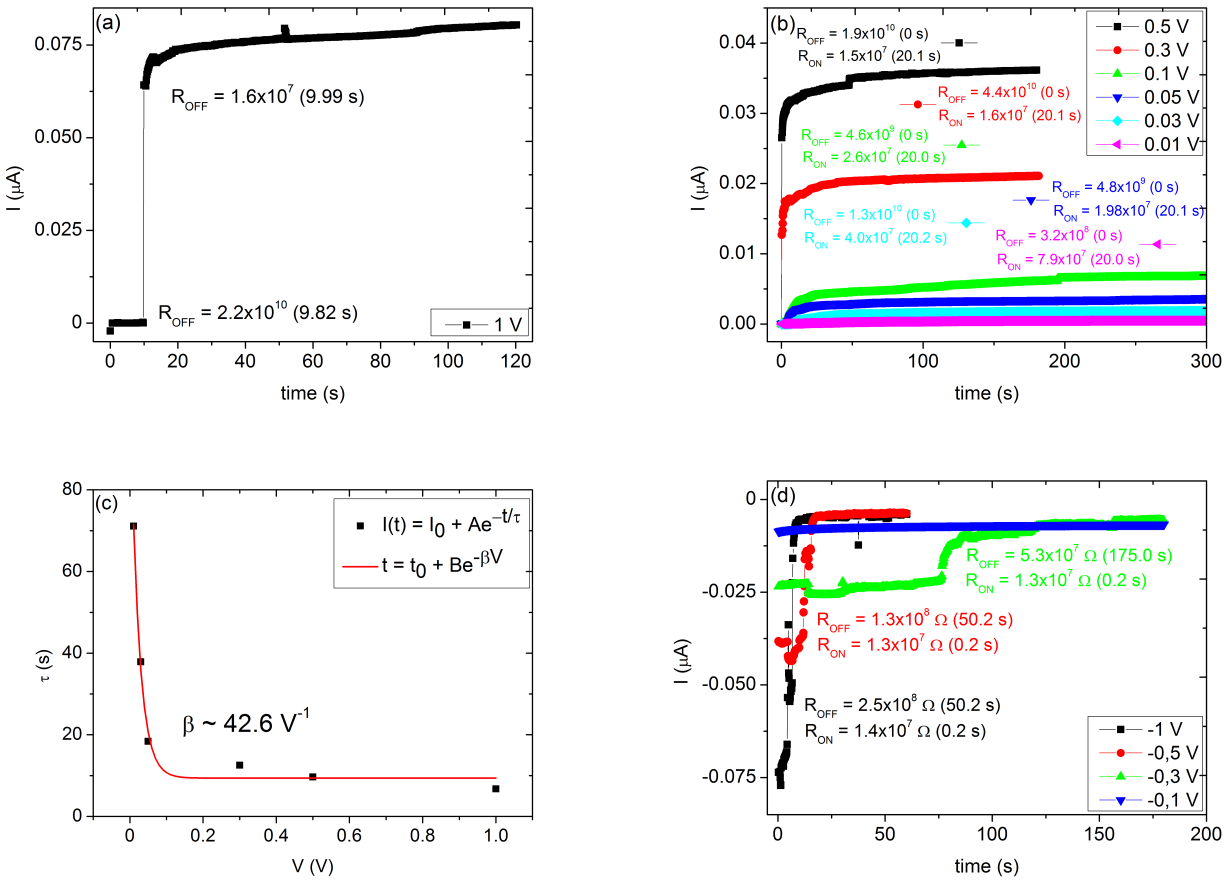

Figure 47: Time dependence measurements of the 81 nm Ag_2S sample with (a) defined set over time for a constant voltage, (b) current - time for different positive voltages, (c) switching time for positive voltages (the caption shows the fitting equations used) and (d) current - time for different negative voltages.

sample to stabilize with a lower resistance a fit to the curves as $I(t) = I_0 + Ae^{-t/\tau}$, where I_0, A and τ are constants, was performed [Fig. 47(c)]. Then, the resulting data was also fitted as $t = t_0 + Be^{-\beta V}$, where t_0, B and β are constants and a time constant was obtained that has an exponential decaying dependence on the applied voltage, proving that it takes exponentially less time to reach the ON state by applying higher positive voltages. The calculated exponential factor ($\beta \sim 42.6$ V^{-1}) is in agreement with the obtained by Nayaka *et al.* (67.7 and 32.9 V^{-1}) [65]. If one applies negative voltages after a set process under positive voltage, reset is also seen to occur after some time [Fig. 47(d)]. One can also see that higher voltages are needed to a complete reset of the device to the original state.

When a constant negative voltage was applied after a complete [-10,10] V cycle (OFF state), the current started to increase (in absolute value) in steps over time [inset of Fig. 48(a)]. This phenomenon may be attributed to the growth of a conductive filament across the sample, thus increasing the conductance in a discrete way. To better study this behavior, we have calculated the conductance (G) over the quantum of conductance ($G_0 = 7.75\times10^{-5}$ Ω^{-1}), as shown in Fig. 48(a). The obtained lower values than G_0 are justified by the fact that the distance between contacts is much larger than the electron mean free path so that we are not in a ballistic regime. These measurements thus cannot distinguish between the existence of a metallic filament shorter than the distance between contacts or a non-metallic, but percolated filament. Also, the applied voltage cycle after each of this measurement present the same single-sided hysteresis behavior as before. When calculating the conductance difference for each step, again a staircase behavior, apparently independent of the applied voltage, is obtained [Fig. 48(b)]. One can note that the conductance difference increases with time but tends asymptotically to zero, which reinforces the filament growth explanation.

4.1.3 Memristor Spice Modeling

It is useful to have computer models of the memristor to compare to experimental results and retrieve physical parameters, as a tool for speeding-up the analysis of its behavior and developing applications of this interesting circuit element via simulation experiments. SPICE (Simulation Program with Integrated Circuit Emphasis) models are the most used for memristor modeling and, consequently, most common in simulations of neuromorphic applications [66]. Many models [24] have been developed to reproduce either a specific physical device or, in a more generalized manner, a wider range of devices.

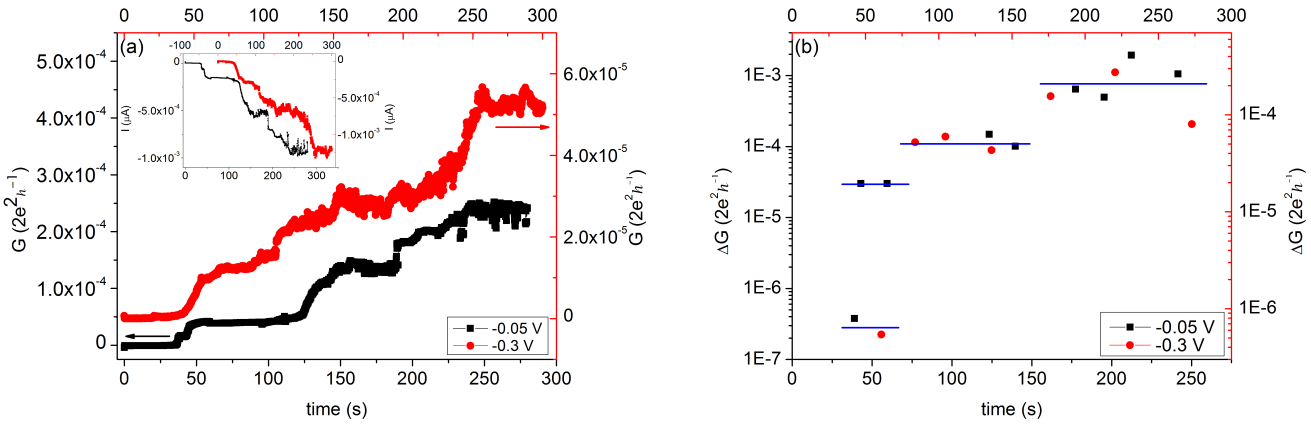

Figure 48: Conductivity study of the 81 nm Ag_2S sample applying a constant negative voltage with (a) conductance time dependence and (b) conductance differential for the current steps (lines are just guides to the eye).

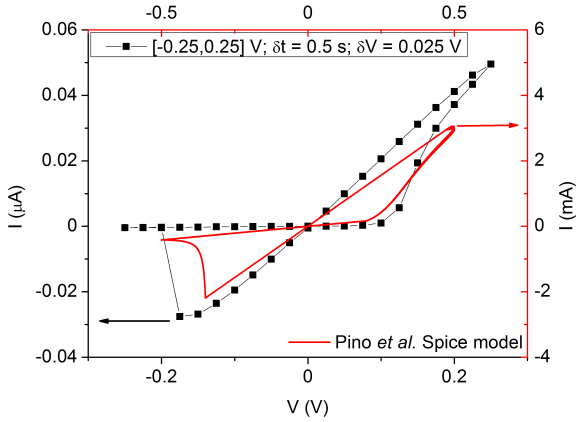

Figure 49: Example of I(V) measurement and memristor Spice model.

Hardware correlated model. Particular models have been developed to fit experimental characterization data, as the model developed by Pino *et al.* at the Air Force Research Lab [67]. Instead of defining a state variable, in this model the rate of change of the resistance is directly defined by differential exponential equations with separated fitting parameters for positive and negative voltages. Our curves [see for example Figs. 36(a) and 39(a)] are similar to those simulated using this empirical chalcogenide compact memristor model (Fig. 49). The careful tuning of this parameters could lead to the perfect adjustment of the model and experimental curves, but since no physical quantities can be extracted from the model, this path was not pursued.

4.1.4 Discussion

The measured Ag-rich Ag_2S sample showed a very strong single-sided hysteresis, i.e. when biased in one direction a large hysteresis is found, while in the opposite direction there is a small or even lack of hysteresis, due to the small set voltage and its strong dependence on the used voltage step and delay time. This behavior correlates very well with the asymmetric structure (multiple dendrites but only one axon) and function of an actual synapse. Furthermore, the obtained asymmetry is necessary to correctly implement STDP in mixed memristor/neuron hybrid systems, since the strengthening/depression only occurs if pre- and post-synaptic spikes demonstrate the correct asymmetric temporal coherence [68]. As attested by the influence of the electrode material on the switching curves type, the two interfaces of the device are the key to both the transport and switching. Particularly the Ag/Ag_2S interface should govern the electric transport of the interface and switching [69].

The high metallic conductance of Ag_2S films after switching has been reported in the literature [8, 70, 71]. In these reports, the linear I(V) curves are interpreted as being due to the formation of a metallic filament which grows due to ionic transport of the reduced Ag^+ ions (at the positive electrode), connecting the electrodes and switching the device to a high conductive state. Switching to the low conductive state is achieved by changing the polarity of the bias voltage, causing the metal atoms to oxidize and dissolve, annihilating the filament. This phenomenon is supported by the observed dependence of the reset voltage on the maximum applied positive voltage, since higher V_{max} values reinforce the filament and difficult its disruption. Furthermore, the dependence of the set voltage on both the voltage step and the delay time shows that, switching depends on the total flux flowing through the sample, the time integral needed to form the filament.

When sweeping the voltage over multiple cycles, we also observed a change in the I(V) curves from the first

to the following curves, which indicates a permanent memory effect in the sample. A possible interpretation is that a structural modification occurs, accompanying the filament growth when the device is switched ON from its virgin state. When the device is switched back OFF, defects remain present and the accumulation of ions at the negative electrode will not be completely undone. This supports the assumption that permanent changes occur in the sample when mass transport of ions initiates [45].

The method of resistive switching in Ag_2S memristive devices may then be attributed to the formation and disruption of nanofilaments within the dielectric layer. Growth of the filaments follows the direction of the applied electric field lines through a process of electromigration from the positive electrode (Ag-probe) toward the negative electrode (probe) with respect to the current flow. This usually yields conically shaped filaments with the base of the cone at the the positive electrode [72].

4.2 Type II Resistive Switching in S-rich Sulfurized Samples

As seen in the previous chapter, the conductivity of a 15 nm Ag film decreases by seven orders of magnitude after an annealing in sulfur atmosphere at 40 °C for 20 min, being an S-rich sample as all the other annealed samples. At this point, current versus voltage measurements were performed. Figure 50 shows typical measurements, where an hysteretic loop is in fact obtained, but of type II, since the loop is non-crossing at zero voltage. Although, with the same conduction mechanisms as before.

An annealing at 40 °C during 40 min of a W(200)/Ag(15) (nm) sample resulted in a S-rich sample (1.91 Ag/S ratio) very close to the ideal. Therefore, this was repeated for other sample, in the same conditions, in order to measure its electrical properties. However, this sample revealed an unknown surface non-uniformity, with a lighter ring on the edge. The first measurements with the two POGO probe contacts were performed between the border and the center of the sample (with positive bias defined as the current flowing from the center to the border of the sample). Figure 51(a) shows that both clockwise (inset), with visible reset ($\sim$ 0.2 V) and set ($\sim$ -0.2 V), and counterclockwise (2nd and 3rd) switchings where obtained with a poor R_{OFF}/R_{ON} ratio ($\sim$ 2) and then a linear behavior started to be observed (R $\sim 10^2$ Ω). For the counterclockwise cycles, an abrupt set occurs when increasing the voltage at around 0.2 V and for negative voltages no switching is observed, being observed the low resistive linear behavior. Note that the absence of hysteresis at one side of the cycle reminds the behavior of the as-deposited 81 nm Ag_2S thin film when probed with an Ag electrode. This may suggest that the border of the sample is somehow Ag-rich in relation to the center. Basically, the

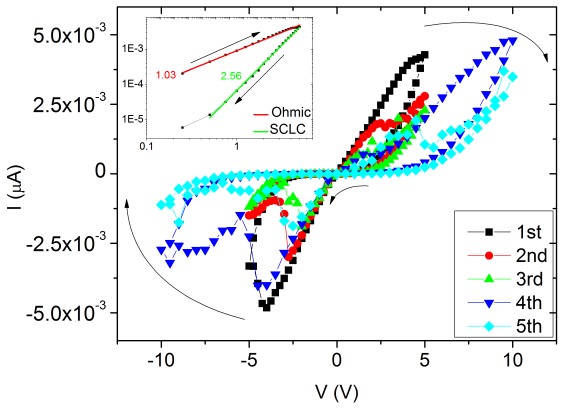

Figure 50: I(V) measurements of the 15 nm Ag sample annealed at 40 °C for 20 min in the [-5,5] V and [-10,10] V ranges with 0.5 s delay (inset shows I(V) in a log-log scale).

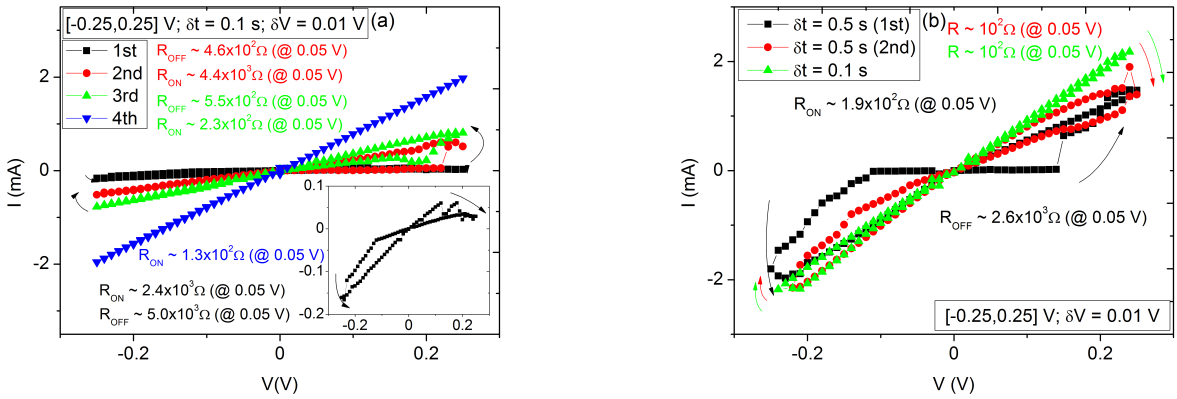

Figure 51: I(V) cycles of the annealed S-rich sample with (a) one tip in the center and the other in the border (inset shows only the first measurement), and (b) one tip in the Ag contact and the other in the center.

sample presented just a few cycles, with low R_{OFF}/R_{ON} ratio and just one or two orders of magnitude lower conductance than the as-deposited 15 nm Ag described above (10^1 to $10^2 - 10^3$ Ω).

An Ag contact was then deposited with silver paint and electrical measurements were performed with the two POGO probe contacts between the border and the Ag electrode (with positive bias defined as the current flowing from the border of the sample to the Ag electrode). The results did not improve, since the abrupt set at around 0.1 V when increasing the voltage leaves the resistance practically unchanged and type II memristive switchings were obtained [Fig. 51(b)].

4.3 Resistive Switching on Chemically Obtained S-rich Samples

To test the functionality of the Ag_2S films prepared by dipping in a DMSO + S solution by transport measurements in a perpendicular configuration, two sets of samples were microfabricated. The difference between the sets of samples is whether they were submersed in the solution (during 1 min at around 60 °C) after the Ag_2S layer deposition or not. One set of samples consisted of a bottom electrode of Al(40)/Ru(5)/Al(50) (nm), while the other had a Pt(100 nm) bottom electrode. The top electrode of the two sets was made of Ag(20)/Ru(5) (nm). The insulator was an as-prepared 15 nm Ag_2S layer deposited from the Ag_2S target. To simplify the following analysis, a identification for these samples is proposed in Table 2.

Identification	Layers (nm)	Solution
Sample 1	Al(40)/Ru(5)/Al(50)/Ag_2S(15)/Ag(20)/Ru(5)	Yes
Sample 2	Al(40)/Ru(5)/Al(50)/Ag_2S(15)/Ag(20)/Ru(5)	No
Sample 3	Pt(100)/Ag_2S(15)/Ag(20)/Ru(5)	Yes
Sample 4	Pt(1000)/Ag_2S(15)/Ag(20)/Ru(5)	No

Table 2: Summary of the properties of the microfabricated samples.

The obtained structures are presented in Fig. 52 for the different lithography steps presented in Section 3, as they were being controlled using optical microscopy. The closeup of the leads for two sample sizes [Figs. 52 (a) and (b)] shows bubbles in the set of samples submersed in the solution, whereas for the other set [Figs. 52 (c) and (d)] the structure is more clear and easily defined.

Unfortunately, sample 4 did not resist all the lithographic process as the glass substrates were too thin and the glass eventually broke. The successfully microfabricated sample 2 was studied in different devices (different

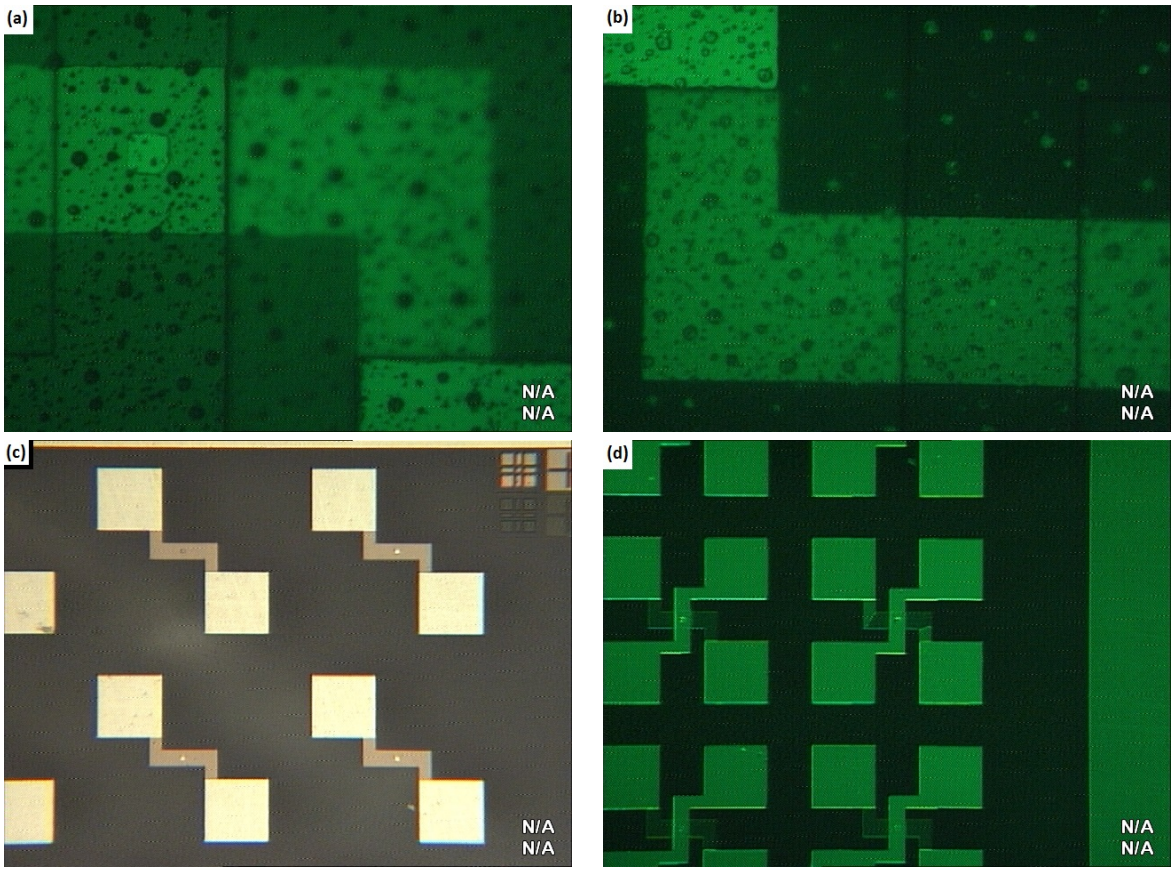

Figure 52: Optical microscope images of relevant microfabrication steps (a) after the second exposition step, (d) after the third lithographic step, (c) after the second and (d) third lift-off step.

sample areas; from 1x1 μm^2 to 10x10 μm^2) and different voltage sweeps. Both set and reset switchings were obtained and probed by successive measurements [Fig. 53(a)]. The sample starts from a low conductive state ($R_{OFF} = 1.52 \times 10^{10}$ Ω) and, at a threshold of 23.5 V, it switchs abruptly to a high conductive state ($R_{ON} = 2.09 \times 10^2$ Ω), reaching the current compliance imposed to avoid device damage. The following positive cycle proves the high conductive state. When applying negative voltages the reset is also abrupt and at a very low voltage (-0.3 V). Figure 53(b), despite some set voltage oscillation, shows that a higher current compliance for the set implies a higher reset voltage, also at higher currents. This may be attributed to the reinforcement of the conductive state by high current flow and filament reinforcement. However, the high to low resistance ratio is still of the order of 10^8. It is important to note that the large difference between the voltage ranges does not stand for the existence of an electroforming step, since the first obtained set was at around 3 V and there is no time relation, just a V_{SET} dispersion. The conduction is SCLC (1.89 slope) from 0 V to 4.3 V [left inset of Fig. 53(b)] and then Ohmic conduction follows as confirmed by the slope at negative voltages (not shown).

It sometimes happened that for the same 1x1 μm^2 sample area that, just by applying negative voltages, the sample switched to ON at negative voltages and held that state [Fig. 54(a)]. For another (7x7 μm^2) sample,

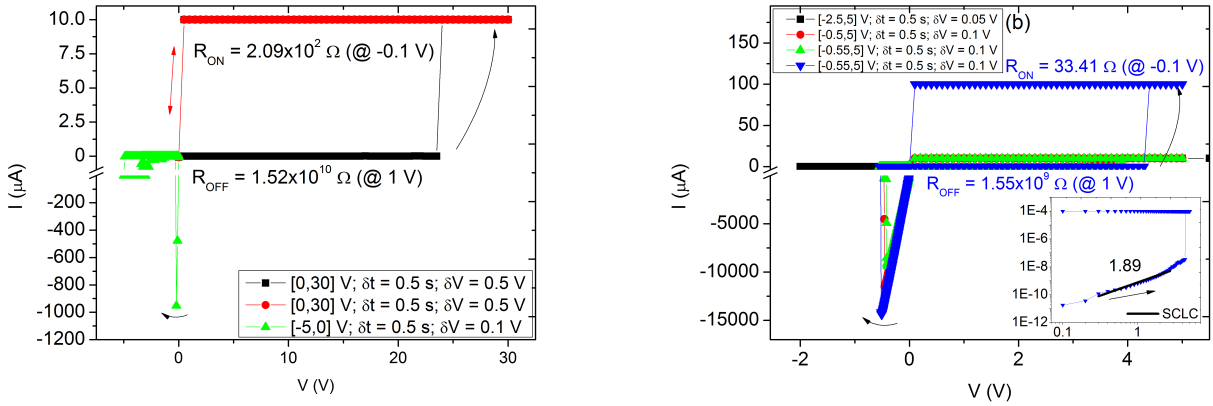

Figure 53: Current - voltage measurements of sample 2 showing (a) a complete bipolar cycle and (b) set and reset voltages oscillation for different current compliances. Both measurements were performed in a 1x1 μm^2 device (inset shows I(V) curves in a log-log scale).

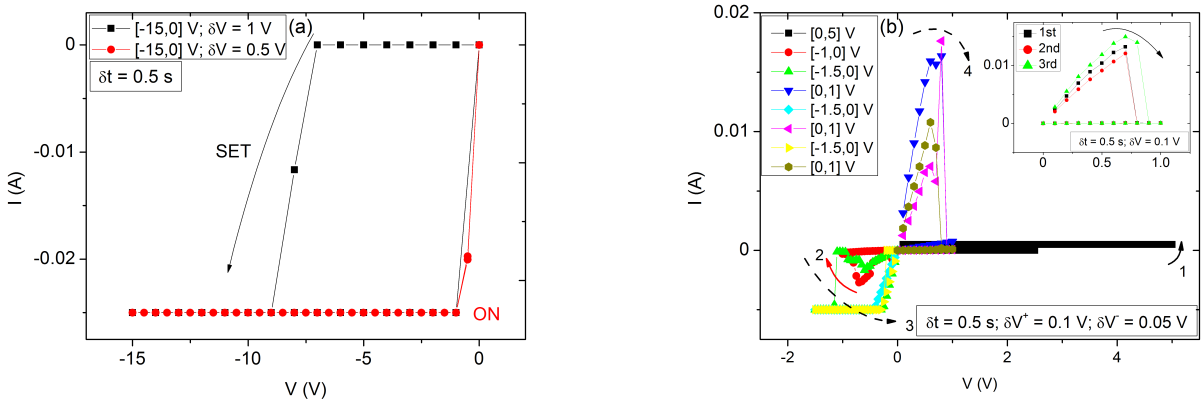

Figure 54: I(V) of sample 2 for (a) 1x1 μm^2 sample area showing non-volatile negative SET and (b) 7x7 μm^2 sample area showing positive and negative set and reset, respectively and reversed (solid arrows are for the first two cycles and dashed ones are for for the remaining; inset shows volatile switchs).

two consecutive reversed cycles were obtained [Fig. 54(b)]: set at positive (point 1) and reset at negative voltage (point 2); set at negative (point 3) and reset at positive voltage (point 4). An even odder behavior was observed when three successive positive cycles revealed three non-volatile resets, as shown in the inset of Fig. 54(b). Normally, most of the devices in sample 2 started with a linear behavior almost metallic at positive voltages (10^{-2} A at 1 V) and only degraded (current decrease) upon applied voltage (not shown).

The same study was performed for sample 1. Generally, the sample starts with a conductive behavior and degrades with cycling [Fig. 55(a)]. Although some samples do make complete cycles [set and reset; Figs. 55(b)-(c)], more commonly only one cycle with noise is seen [Figs. 55(c)].

An annealing at 180 ^{o}C for 1 h was performed in this sample to allow the diffusion of Ag-S in the Ag_2S layer, as a way to stabilize the compound and increase its resistivity. Although sometimes the sample again started in a conductive state and then degraded, the overall behavior improved and a bipolar type I memristive switching was observed, with the possibility of performing more than one cycle [Fig. 56(a)]. However, samples presenting only one complete cycle followed by degradation [Fig. 56(b) and (c)] were still observed. The sets

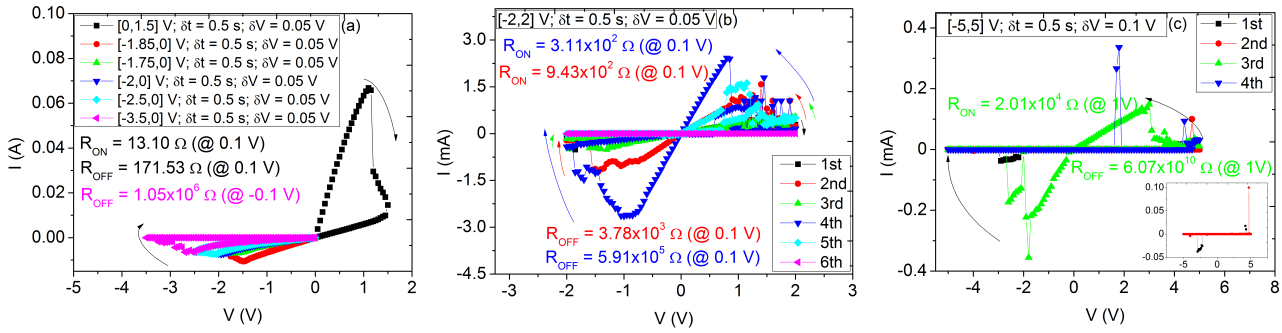

Figure 55: I(V) measurements on sample 1 showing (a) degradation (3x3 μm^2), (b) resistive switching (3x3 μm^2) and (c) current peaks (3x3 μm^2; inset shows only the first and second measurements).

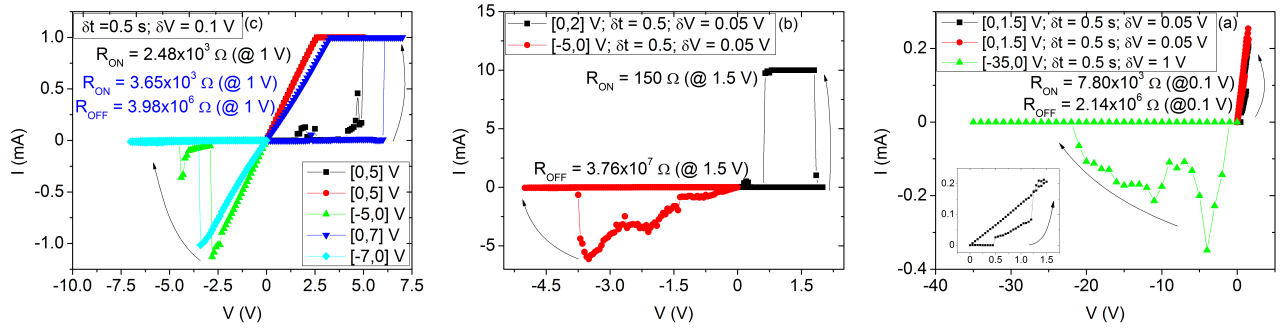

Figure 56: I(V) characteristics of the annealed sample 1 showing (a) two cycles (5x5 μm^2), (b) one cycle (6x6 μm^2) and (c) one cycle (3x3 μm^2; inset shows only the first measurement).

are abrupt at 6 V [Fig. 56(a)], 1.9 V [Fig. 56(b)] and early at around 0.45 V [Fig. 56(c)].

Other different switching behaviors were observed in these devices: memristive type II curve [Fig. 57(a)], unipolar behavior in which both set and reset were seen at negative [Fig. 57(b)] or positive voltages for different cycles [Fig. 57(c)] and complementary resistive switching [Fig. 57(d)]. This last switching behavior is characterized by switching polarity reversal. Usually, a complementary resistive switch is composed of two bipolar memory cells that are connected anti-serially [73, 74]. Here, we have a resistive memory that achieves the complementary switching functionality within a single memory cell. When increasing the voltage the device remains in an high resistive state until a set occurs at around 3.5 V for positive voltages and -12.5 V for negative voltages. This high resistance at low voltages is associated with a drastic reduction of the static power consumption and is considered a potential solution for the sneak path problem in large-scale integration of passive crossbar resistive memory arrays. The low resistive state is kept until 18 V and -18.5 V, respectively, since further voltage increase switchs the device back to the high resistance, again at both polarities. Our set and reset values are not symmetric to positive and negative voltages as usual, which may be attributed to the weak symmetry of the device.

Figure 58(a) shows one device in which switching seemed to fade away with voltage cycles but restarted again at higher positive voltage. Afterwards, one type I and two type II memristor cycles were observed just before the complete deterioration of the sample. This may indicate different behaviors at different voltage ranges, but further studies are necessary to confirm it.

Finally, no relevant results were obtained for sample 3. Unfortunately, since sample 4 was lost, we can not compare and conclude the reason for such lack of switching is related with the use of a Pt bottom layer or of the solution with Pt.

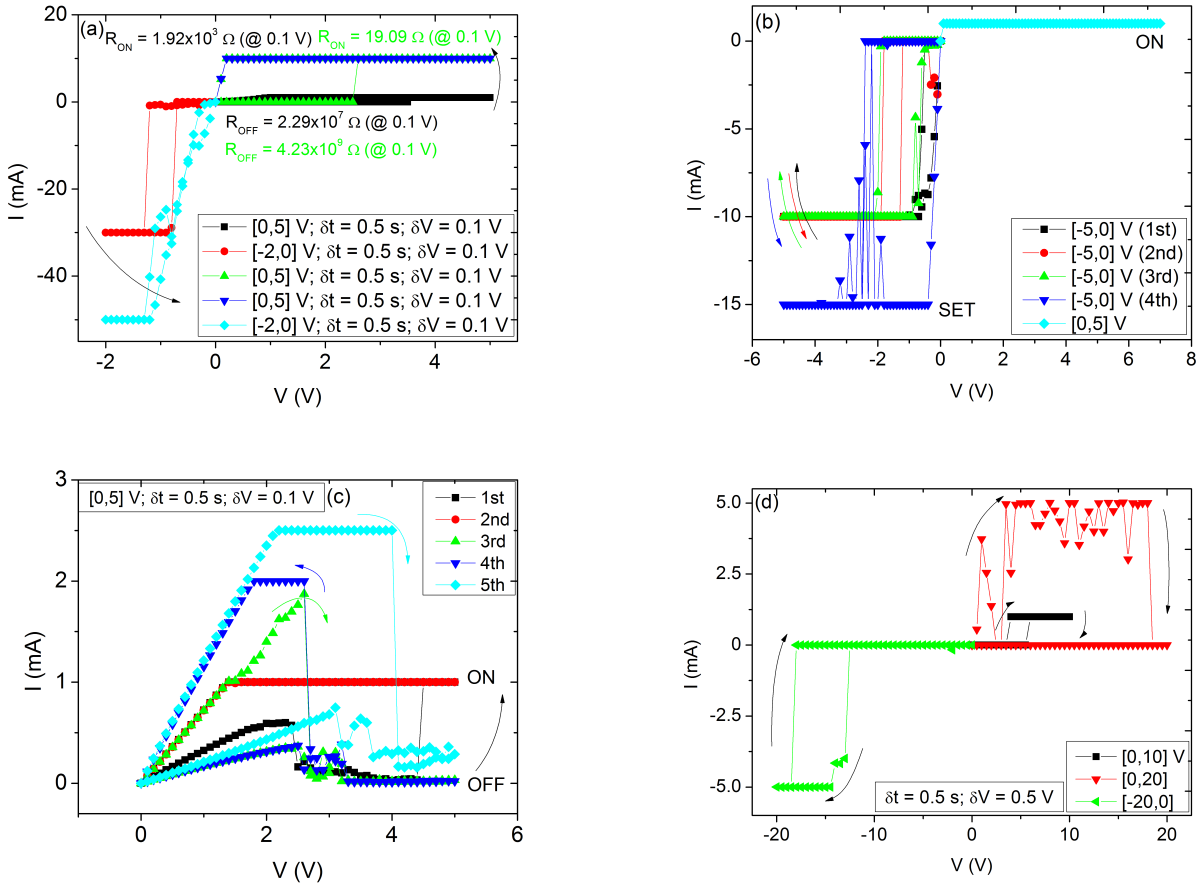

Figure 57: I(V) measurements of the annealed sample 1 showing different switching properties, such as (a) type II (4x4 μm^2), (b) unipolar negative (7x7 μm^2), (c) unipolar positive (10x10 μm^2) and (d) complementary resistive switching (7x7 μm^2).

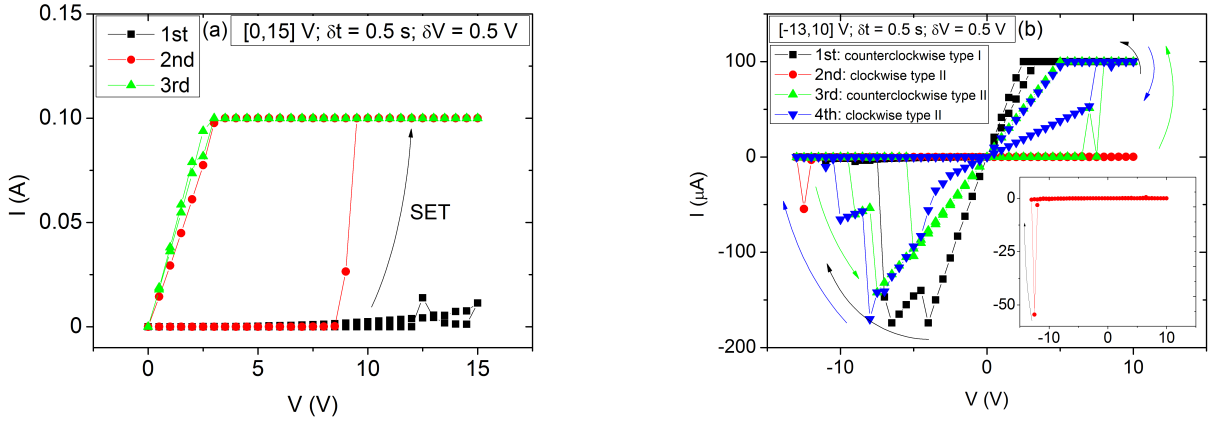

Figure 58: I(V) curves of the annealed sample 1 for 7x7 μm^2 showing (a) reborn and (b) both type I and II switching (inset shows only the second measurement).

4.4 Conclusions

The electrical characterization and switching properties of the fabricated Ag_2S thin films were presented in this chapter. The Ag_2S thin films presented low conductive behavior at low bias voltages, whereas they exhibited reproducible bipolar resistance switching at higher bias voltages, without the need of an electroforming step. The transition between both types of behavior is observed by hysteresis in the I(V) curves, indicating decomposition of the Ag_2S and formation of a conductive path between the electrodes. These metallic channels are confirmed by the observed linear I(V) behavior in the ON state. If we assume a cylindrical Ag conductive filament of 2 nm radius and using Ohm's law, the calculated resistance is of the order of 10^8 Ω for the Ag resistivity obtained in the previous chapter and 10^9 Ω for argentite (assuming a resistivity of 10^{-3}Ωcm [19]). The same calculus for a pure Ag_2S (acanthite) filament gives 10^{15} Ω. This reveals that the OFF state of the samples consists of Ag-rich acanthite, as determined by the XRD analysis developed in the previous chapter, while the ON state filament is likely composed of silver.

The ion beam deposited Ag_2S samples when measured with the shadow masked electrodes presented smooth type I bipolar switchings with very reproducible cycles. However, they showed a type II memristive behavior with degradation upon cycle repetition when measured directly on the sample surface. For the microfabricated samples memristive type I and II curves, bipolar and unipolar behaviors and complementary resistive switching, were different switching behaviors observed. These samples exhibited more abrupt set and reset bipolar switchings and a more conductive behavior than the others (mA instead of μA). The annealed samples only showed type II memristive behavior with degradation upon cycle repetition, even with one Ag electrode. However, when the measurements were performed between the brighter edge and the center of the sample, a half-pinched hysteresis loop similar to the ones of the as-deposited Ag_2S sample was observed.

'POSSIBLE ENDING'

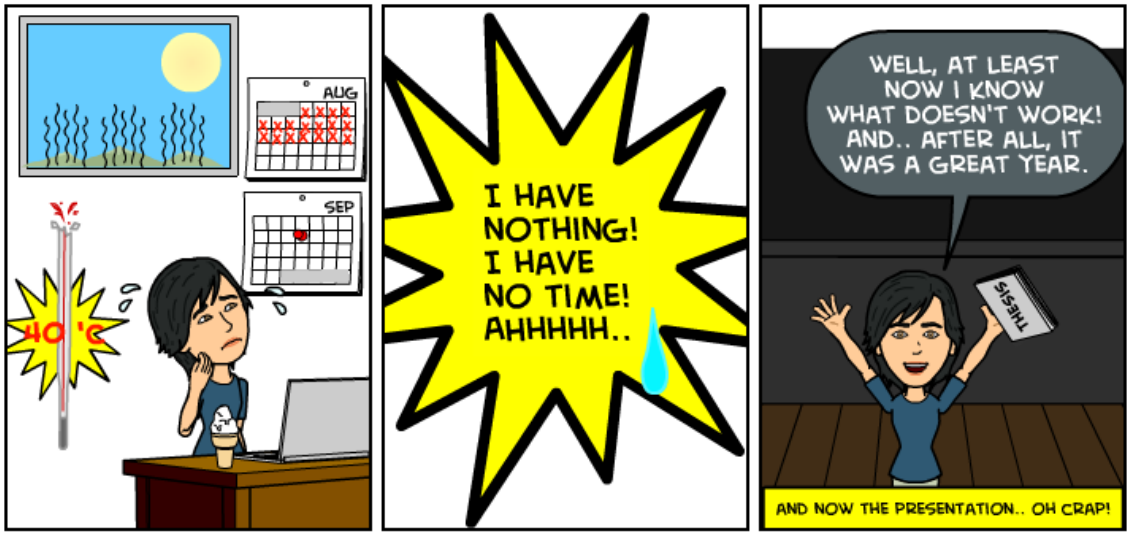

Chapter 5

Conclusions and Outlook

In keeping with the revered tradition in Physics, the existence of an ideal memristor was predicted in 1971 based purely on symmetry arguments. However, its experimental discovery and the accompanying elegant physical picture required the advent of Nanotechnology and thus took another 37 years. Forty years after the first projection regarding the similarity between the resistive switching in a metal/dielectric junction and the axon coupling in a synaptic junction, development of a solid-state electronic device to replicate the functions of the human brain is finally being successful [75].

In an effort to satisfy all the needed performance, endurance, retention, scalability and integration into crossbar arrays for the adaptive memory cells proposed in the literature, a wide set of open questions, materials and design issues are still to explore. Further investigations gathering several fields such as physics, electronics, materials science, chemistry and neuroscience are imperative to overcome forthcoming scientific and technical challenges.

In this work we used Ag_2S as a model system to study resistance switching and activity-dependent modifications. Ag_2S forms an appropriate model system for the understanding of memristive nano-ionic devices and to study the physics of resistive switching. It is also an adequate prototype material for the fabrication of artificial neural networks. It can be fabricated by relatively straightforward techniques that further lead to close to ideal stoichiometry (Chapter 3). In Chapter 4 we presented the electrical switching properties of Ag_2S thin films fabricated by ion beam deposition, chemical routes and sulfurization, either sandwiched between two electrodes or with contacts on top. The electrical I(V) measurements enabled the identification of an initial semiconductor behavior, followed by bipolar switching at higher bias voltages, when a conductive path is formed. Bipolar resistive switching is observed during multiple cycles in most of the samples, provided that the applied voltage is higher than a threshold voltage. Moreover, unipolar and complementary resistive switching, as well as both type I and II memristive behaviors, were also observed. From the behavior of current versus time traces, the filament formation inside the Ag_2S film was inferred. The obtained low writing voltage, although an advantage in terms of low energy operation, is a disadvantage for the definition of the read voltage, since the latter has to be significantly low not to change the state of the device. The modification of the samples properties after several switching cycles is also undesirable in terms of endurance.

As future work, one expects to achieve, in a reproducible and systematic way Ag-rich Ag_2S thin films depositing a thin Ag layer on top of sulfurized Ag_2S (and thus S-rich). Subsequent annealing in vacuum will promote Ag diffusion and balance the content in the samples. To better characterize the variation in the composition of the fabricated samples we will perform X-ray Photoelectron Spectroscopy (XPS), as well as Transmission Electron Microscopy (TEM) to endorse the existence of a conductive filament inside the Ag_2S dielectric layer. Given the photosensitivity of Ag_2S and the substantial associated applications, it would be worth exploring the exposure of a whole sample to the same light characteristics of the Raman spectroscopy and to perform XRD characterization (or other) to identify the compound formed. It would also be interesting to measure *in situ* the variation of the resistance of Ag or Ag_2S thin films during thermal annealing in sulfur atmosphere, to observe in real time the transition from an Ag-rich to an S-rich sample. The deposition of electrodes of different thicknesses and materials having different work functions will allow us to test the persistence of the half-pinched hysteresis loop.

The synthesis of inorganic artificial synapses, with the purpose of building artificial neural networks is remarkably promising. So far, the principles of artificial synapses have been shown only for individual memory cells (synapses). However, one can predict that, in the future, several of the materials and structures studied

for resistive memories will eventually be used in the fabrication of artificial synapses. Thus, the individual memory cells must be integrated into crossbar arrays and our proposed future work includes the simulation and fabrication of artificial networks with optimized devices.

References

[1] L. P. Shi, K. J. Yi, K. Ramanathan, R. Zhao, N. Ning, D. Ding, and T. C. Chong. Artificial cognitive memory - changing from density driven to functionality driven. *Applied Physics A*, **102**, 4 (2011).

[2] Jose M. Cruz-Albrecht, Michael W. Yung, and Narayan Srinivasa. Energy-Efficient Neuron, Synapse and STDP Integrated Circuits. *IEEE Transactions on Biomedical Circuits and Systems*, **6**, 3 (2012).

[3] Carlos Zamarreño Ramos, Luis a Camuñas Mesa, Jose a Pérez-Carrasco, Timothée Masquelier, Teresa Serrano-Gotarredona, and Bernabé Linares-Barranco. On spike-timing-dependent-plasticity, memristive devices, and building a self-learning visual cortex. *Frontiers in neuroscience*, **5** (2011).

[4] Uma R Karmarkar and Dean V Buonomano. A model of spike-timing dependent plasticity: one or two coincidence detectors? *Journal of neurophysiology*, **88**, 1 (2002).

[5] Shimeng Yu, Yi Wu, and Rakesh Jeyasingh. An electronic synapse device based on metal oxide resistive switching memory for neuromorphic computation. *IEEE Transactions on Electron Devices*, **58**, 8 (2011).

[6] Dmitri B Strukov, Gregory S Snider, Duncan R Stewart, and R Stanley Williams. The missing memristor found. *Nature*, **453**, 7191 (2008).

[7] H.-S. Philip Wong, Heng-Yuan Lee, Shimeng Yu, Yu-Sheng Chen, Yi Wu, Pang-Shiu Chen, Byoungil Lee, Frederick T. Chen, and Ming-Jinn Tsai. Metal-Oxide RRAM. *Proceedings of the IEEE*, **100**, 6 (2012).

[8] Rainer Waser and Masakazu Aono. Nanoionics-based resistive switching memories. *Nature materials*, **6**, 11 (2007).

[9] Tsuyoshi Hasegawa, Kazuya Terabe, Tohru Tsuruoka, and Masakazu Aono. Atomic switch: atom/ion movement controlled devices for beyond von-neumann computers. *Advanced materials (Deerfield Beach, Fla.)*, **24**, 2 (2012).

[10] Kyung Min Kim, Doo Seok Jeong, and Cheol Seong Hwang. Nanofilamentary resistive switching in binary oxide system; a review on the present status and outlook. *Nanotechnology*, **22**, 25 (2011).

[11] Sung Hyun Jo, Ting Chang, Idongesit Ebong, Bhavitavya B Bhadviya, Pinaki Mazumder, and Wei Lu. Nanoscale memristor device as synapse in neuromorphic systems. *Nano letters*, **10**, 4 (2010).

[12] Sieu D. Ha and Shriram Ramanathan. Adaptive oxide electronics: A review. *Journal of Applied Physics*, **110**, 7 (2011).

[13] Ting Chang, SungHyun Jo, and Wei Lu. Short-term memory to long-term memory transition in a nanoscale memristor. *ACS nano*, **5**, 9 (2011).

[14] Y. Liu, T. P. Chen, Z. Liu, Y. F. Yu, Q. Yu, P. Li, and S. Fung. Self-learning ability realized with a resistive switching device based on a Ni-rich nickel oxide thin film. *Applied Physics A*, **105**, 4 (2011).

[15] J Joshua Yang, Dmitri B Strukov, and Duncan R Stewart. Memristive devices for computing. *Nature nanotechnology*, **8**, 1 (2013).

[16] Peter N Nirmalraj, Allen T Bellew, Alan P Bell, Jessamyn a Fairfield, Eoin K McCarthy, Curtis O'Kelly, Luiz F C Pereira, Sophie Sorel, Diana Morosan, Jonathan N Coleman, Mauro S Ferreira, and John J Boland. Manipulating connectivity and electrical conductivity in metallic nanowire networks. *Nano letters*, **12**, 11 (2012).

[17] H. Schmalzried. Ag2S - The physical chemistry of an inorganic material. *Progress in Solid State Chemistry*, **13**, 2 (1980).

[18] S Kashida, N Watanabe, T Hasegawa, and H Iida. Electronic structure of Ag2S, band calculation and photoelectron spectroscopy. *Solid State Ionics*, **158**, 1-2 (2003).

[19] Malcolm H. Hebb. Electrical Conductivity of Silver Sulfide. *The Journal of Chemical Physics*, **20**, 1 (1952).

[20] Kazuya Terabe, Tsuyoshi Hasegawa, Changhao Liang, and Masakazu Aono. Control of local ion transport to create unique functional nanodevices based on ionic conductors. *Science and Technology of Advanced Materials*, **8**, 6 (2007).

[21] Irene Martina, Rita Wiesinger, Dubravka Jembrih-Simbürger, and Manfred Schreiner. Micro-Raman Characterisation of Silver Corrosion Products: Instrumental Set Up and Reference Database. *E-Preservation Science*, **9** (2012).

[22] I. Martina, R. Wiesinger, and M. Schreiner. Micro-Raman investigations of early stage silver corrosion products occurring in sulfur containing atmospheres. *Journal of Raman Spectroscopy*, **44**, 5 (2013).

[23] Fernando Corinto, Alon Ascoli, and Marco Gilli. Class of all i-v dynamics for memristive elements in pattern recognition systems. In *International Joint Conference on Neural Networks*, pages 2289–2296 (2011).

[24] Robert Kozma, Robinson E. Pino, and Giovanni E. Pazienza. *Advances in Neuromorphic Memristor Science and Applications*. Springer Publishing Company, Incorporated (2012).

[25] Zhong Qiang Wang, Hai Yang Xu, Xing Hua Li, Hao Yu, Yi Chun Liu, and Xiao Juan Zhu. Synaptic Learning and Memory Functions Achieved Using Oxygen Ion Migration/Diffusion in an Amorphous InGaZnO Memristor. *Advanced Functional Materials*, **22**, 13 (2012).

[26] Sang Jun Choi, Guk-Bae Kim, Kyoobin Lee, Ki-Hong Kim, Woo-Young Yang, Soohaeng Cho, Hyung-Jin Bae, Dong-Seok Seo, Sang-Il Kim, and Kyung-Jin Lee. Synaptic behaviors of a single metal-oxide-metal resistive device. *Applied Physics A*, **102**, 4 (2011).

[27] Kyungah Seo, Insung Kim, Seungjae Jung, Minseok Jo, Sangsu Park, Jubong Park, Jungho Shin, Kuyyadi P Biju, Jaemin Kong, Kwanghee Lee, Byounghun Lee, and Hyunsang Hwang. Analog memory and spike-timing-dependent plasticity characteristics of a nanoscale titanium oxide bilayer resistive switching device. *Nanotechnology*, **22**, 25 (2011).

[28] Takeo Ohno, Tsuyoshi Hasegawa, Tohru Tsuruoka, Kazuya Terabe, James K Gimzewski, and Masakazu Aono. Short-term plasticity and long-term potentiation mimicked in single inorganic synapses. *Nature materials*, **10**, 8 (2011).

[29] Leon Chua. Memristor-the missing circuit element. *IEEE Transactions on Circuit Theory*, **18**, 5 (1971).

[30] LO Chua and SM Kang. Memristive devices and systems. *Proceedings of the IEEE*, **64**, 2 (1976).

[31] Yogesh N Joglekar and Stephen J Wolf. The elusive memristor: properties of basic electrical circuits. *European Journal of Physics*, **30**, 4 (2009).

[32] Yuriy V. Pershin and Massimiliano Di Ventra. Memory effects in complex materials and nanoscale systems. *Advances in Physics*, **60**, 2 (2011).

[33] Tohru Tsuruoka, Tsuyoshi Hasegawa, Kazuya Terabe, and Masakazu Aono. Conductance quantization and synaptic behavior in a Ta2O5-based atomic switch. *Nanotechnology*, **23**, 43 (2012).

[34] An Chen. Ionic Memory Technology. In *Solid State Electrochemistry II: Electrodes, Interfaces and Ceramic Membranes*, chapter 1, pages 1–18. 1st edition (2011).

[35] Carsten Kügeler, Roland Rosezin, Eike Linn, Rainer Bruchhaus, and Rainer Waser. Materials, technologies, and circuit concepts forÂ nanocrossbar-based bipolar RRAM. *Applied Physics A*, **102**, 4 (2011).

[36] Johannes Schemmel and A Grubl. Implementing synaptic plasticity in a VLSI spiking neural network model. In *Neural Networks, International Joint Conference on*, pages 1–6 (2006).

[37] D.B. Strukov and H. Kohlstedt. Resistive switching phenomena in thin films: Materials, devices, and applications. *MRS Bulletin*, **37**, 02 (2012).

[38] Garrett S. Rose, Robinson Pino, and Qing Wu. A low-power memristive neuromorphic circuit utilizing a global/local training mechanism. In *The 2011 International Joint Conference on Neural Networks*, number 1, pages 2080–2086. Ieee (2011).

[39] G S Snider. Self-organized computation with unreliable, memristive nanodevices. *Nanotechnology*, **18**, 36 (2007).

[40] Idongesit E. Ebong and Pinaki Mazumder. CMOS and Memristor-Based Neural Network Design for Position Detection. *Proceedings of the IEEE*, **100**, 6 (2012).

[41] Maheshwar Pd Sah, Changju Yang, Hyongsuk Kim, and Leon Chua. A voltage mode memristor bridge synaptic circuit with memristor emulators. *Sensors*, **12**, 3 (2012).

[42] E Linn, R Rosezin, S Tappertzhofen, U Böttger, and R Waser. Beyond von Neumann–logic operations in passive crossbar arrays alongside memory operations. *Nanotechnology*, **23**, 30 (2012).

[43] D S Jeong, R Thomas, R S Katiyar, J F Scott, H Kohlstedt, A Petraru, and C S Hwang. Emerging memories: resistive switching mechanisms and current status. *Reports on progress in physics*, **75**, 7 (2012).

[44] BR Sankapal, RS Mane, and CD Lokhande. A new chemical method for the preparation of Ag 2 S thin films. *Materials chemistry and physics*, **63**, 3 (1999).

[45] M Morales Masis. Resistive switching in mixed conductors: Ag2S as a model system. (2012).

[46] Beata Bochentyn. Mixed ionic-electronic composite materials: properties and various methods of their investigation.

[47] R.J. Cava, F. Reidinger, and B.J. Wuensch. Single-crystal neutron diffraction study of the fast-ion conductor β-Ag2S between 186 and 325 oC. *Journal of Solid State Chemistry*, **31**, 1 (1980).

[48] Gilles R Bourret and R Bruce Lennox. Electrochemical synthesis of Ag(0)/Ag2S heterojunctions templated on pre-formed Ag2S nanowires. *Nanoscale*, **3**, 4 (2011).

[49] M. Morales-Masis, S. J. van der Molen, T. Hasegawa, and J. M. van Ruitenbeek. Bulk and surface nucleation processes in Ag2S conductance switches. *Physical Review B*, **84**, 11 (2011).

[50] Manisha Kundu, Kazuya Terabe, Tsuyoshi Hasegawa, and Masakazu Aono. Effect of sulfurization conditions and post-deposition annealing treatment on structural and electrical properties of silver sulfide films. *Journal of Applied Physics*, **99**, 10 (2006).

[51] Masakazu Aono and Tsuyoshi Hasegawa. The Atomic Switch. *Proceedings of the IEEE*, **98**, 12 (2010).

[52] Takeo Ohno, Tsuyoshi Hasegawa, Tohru Tsuruoka, Kazuya Terabe, James K Gimzewski, and Masakazu Aono. Short-term plasticity and long-term potentiation mimicked in single inorganic synapses. *Nature materials*, **10**, 8 (2011).

[53] Takeo Ohno, Tsuyoshi Hasegawa, Alpana Nayak, Tohru Tsuruoka, James K. Gimzewski, and Masakazu Aono. Sensory and short-term memory formations observed in a Ag2S gap-type atomic switch. *Applied Physics Letters*, **99**, 20 (2011).

[54] Audrius V Avizienis, Henry O Sillin, Cristina Martin-Olmos, Hsien Hang Shieh, Masakazu Aono, Adam Z Stieg, and James K Gimzewski. Neuromorphic atomic switch networks. *PloS one*, **7**, 8 (2012).

[55] Tsuyoshi Hasegawa, Takeo Ohno, Kazuya Terabe, Tohru Tsuruoka, Tomonobu Nakayama, James K Gimzewski, and Masakazu Aono. Learning abilities achieved by a single solid-state atomic switch. *Advanced materials*, **22**, 16 (2010).

[56] R Vignes. Dimethyl sulfoxide (DMSO). A "new" clean, unique, superior solvent. In *American Chemical Society Annual Meeting*, number 228 (2000).

[57] XS Peng, GW Meng, J Zhang, and XF Wang. Electrochemical fabrication of ordered Ag2S nanowire arrays. *Materials research Bulletin*, **37**, 7 (2002).

[58] David R. Lide. *Handbook of Chemistry and Physics*. Number V (2008).

[59] W Hayes and R Loudon. *Scattering of Light by Crystals*. Wiley-Interscience (1978).

[60] C. I. Pearce. Electrical and Magnetic Properties of Sulfides. *Reviews in Mineralogy and Geochemistry*, **61**, 1 (2006).

[61] F Cardarelli. *Materials handbook: a concise desktop reference* (2008).

[62] C Hillman, J Arnold, S Binfield, and J Seppi. Silver and sulfur: Case studies, physics and possible solutions. In *SMTA International* (2007).

[63] BT Phan, Chulho Jung, Taekjib Choi, and Jaichan Lee. Trap-Controlled Space-Charge-Limited Current Conduction in the Cr-Doped SrTiO3 Thin Films Deposited by Using Pulsed Laser Deposition. *Journal of Korean Physical Society*, **51**, 2 (2007).

[64] Jennifer L. M. Rupp, Patrick Reinhard, Daniele Pergolesi, Thomas Ryll, Rene Tölke, and Enrico Traversa. Electric-field-induced current-voltage characteristics in electronic conducting perovskite thin films. *Applied Physics Letters*, **100**, 1 (2012).

[65] Alpana Nayak, Takuro Tamura, Tohru Tsuruoka, Kazuya Terabe, Sumio Hosaka, Tsuyoshi Hasegawa, and Masakazu Aono. Rate-Limiting Processes Determining the Switching Time in a Ag 2 S Atomic Switch. *The Journal of Physical Chemistry Letters*, **1**, 3 (2010).

[66] Jayawan H B Wijekoon and Piotr Dudek. VLSI circuits implementing computational models of neocortical circuits. *Journal of neuroscience methods*, **210**, 1 (2012).

[67] RE Pino, JW Bohl, and N McDonald. Compact Method for Modeling and Simulation of Memristor Devices. In *Nanoscale Architectures (NANOARCH)*, pages 1–4 (2010).

[68] Adam Williamson, Lars Schumann, Lars Hiller, Frank Klefenz, Ingo Hoerselmann, Peter Husar, and Andreas Schober. Synaptic behavior and STDP of asymmetric nanoscale memristors in biohybrid systems. *Nanoscale*, **5**, 16 (2013).

[69] J. Joshua Yang, Julien Borghetti, David Murphy, Duncan R. Stewart, and R. Stanley Williams. A Family of Electronically Reconfigurable Nanodevices. *Advanced Materials*, **21**, 37 (2009).

[70] K Terabe, T Hasegawa, T Nakayama, and M Aono. Quantized conductance atomic switch. *Nature*, **433**, January (2005).

[71] Changhao Liang, Kazuya Terabe, Tsuyoshi Hasegawa, and Masakazu Aono. Resistance switching of an individual Ag2S/Ag nanowire heterostructure. *Nanotechnology*, **18**, 48 (2007).

[72] Shanshan Peng, Fei Zhuge, Xinxin Chen, Xiaojian Zhu, Benlin Hu, Liang Pan, Bin Chen, and Run-Wei Li. Mechanism for resistive switching in an oxide-based electrochemical metallization memory. *Applied Physics Letters*, **100**, 7 (2012).

[73] Yuchao Yang, Patrick Sheridan, and Wei Lu. Complementary resistive switching in tantalum oxide-based resistive memory devices. *Applied Physics Letters*, **100**, 20 (2012).

[74] Eike Linn, Roland Rosezin, Carsten Kügeler, and Rainer Waser. Complementary resistive switches for passive nanocrossbar memories. *Nature materials*, **9**, 5 (2010).

[75] Hiroyuki Akinaga and Hisashi Shima. Resistive Random Access Memory (ReRAM) Based on Metal Oxides. *Proceedings of the IEEE*, **98**, 12 (2010).

A Masks Design

B Runsheet

Memristors microfabrication

Responsible: João Pereira Project: / Run:

Process Start : 18 /03 /2013 **Process Finish :** 27 /03 /2013

STEP 1: deposition
Ion Beam Sputter Deposition system by Commonwealth Scientific Corporation (IFIMUP) Glass Subtract

C8: Glass/Al(50)/Ru(5)/Al(40)/Ag2S(15)*/Ag(20)/Ru(5)
C9: Glass/Al(50)/Ru(5)/Al(40)/Ag2S(15)/Ag(20)/Ru(5)
C10: Glass/Pt(100)/Ag2S(15)*/Ag(15)/Ru(5)
C12: Glass/Pt(100)/Ag2S(15)/Ag(15)/Ru(5)
***HV deposition stopped for dipping the sample in a DMSO + S solution**

STEP 2: 1st Exposure - Bottom contacts definition

Date: 19/03/2013 **Operator**: Jo
Equipment: **SVG Photoresist track, DWL**

Vapor prime, 30 min (Recipe – 0)
Purge oven for 25 min at 130ºC in N_2 atmosphere at 10Torr;
Bake with surfactant for 5 min at 130ºC and 5 Torr pressure; Surfactant: hexadimethylsilane

Photoresist coating, 1.5 µm PR (Recipe 6/2)
Type: Positive photoresist PFR7790G 2cP *JSR Electronics*
Sample heating for 60s at 110ºC; Cool down for 30s;
Photoresist spinning for 40s at 2500 rpm (1.5 µm photoresist); Baking for 60s at 85ºC

Direct laser write exposure Start:_____ finish: _____ (Total time ~ 9 min each)
Masks: `MemRBot4` (inverted) Map: AMSION Die size: X = 10754, Y = 10002

Energy: 80 Focus: 60 Power:_____
Align mark positions:

X=168.5; Y=9948	X=5378.5; Y=9948	X=10700.5; Y=9948
X=168.5; Y=5081	X=5378.5; Y=5081	X=10700.5; Y=5081
X=168.5; Y=54	X=5378.5; Y=54	X=10700.5; Y=54

Photoresist developing, (Recipe 6/2);
Sample heating for 60s at 110ºC
Cool down for 30s
Developing for 60s(+10s): (C8, C12)

e.a.

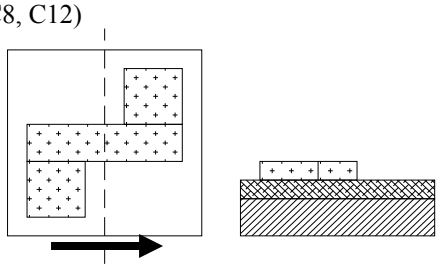

Comments:

mask in

STEP 3: Ion Beam Milling (IBM) – Etch 1954,1Å

Date: 19/03/2013 **Operator**:
Equipment: **Nordiko 3600**

Conditions
Batch: junction_etch
wafer #

Base Pressure
Etch time:

Etch rate:
P_{dep} ~ Torr; Target #

Assist Gun	Power [W_{RF}]	V+ [V]	I+ [mA]	V- [V]	I- [ma]	Ar Flux [sccm]
Set Values						
Read	65	735	105	320		10

Neutralizer	Voltage [V]	Current [ma]	Gas (Ar) [sccm]
Set Values	-		
Read			

Substrate	Rotation [%]	Pan [deg]
Set Values		
Read	30	60

Comments: The photoresist in the samples of thin glass burned.

STEP 4: 1º Protective Layer Deposition – Al_2O_3 Deposition

Date: 19-20/03/2013 **Operator**:
Equipment: **UHV2**
RF Sputtering deposition (PVD)
B. P.: Torr

Material	P [W_{RF}]	Pdep [Torr]	Ar [sccm]	Thickness	R [A/min]	T [min]
Al_2O_3	200	3.1E-3	44.9	**1150Å**	12	98

Observations:

Comments:

STEP 5: 1st Photoresist stripping

Date: 20.03.2013 **Operator**:
Start: Finished:
Equipment: Wet bench in gray area
Total time in Acetone: overnight Ultrasonic Time: 2h5min

Stripping
Ultrasounds
Rinse with IPA + DI water + dry N_2
Cleaning
IPA rinse; DI water rinse; Dry with N2 gun
(mechanical cleaning with a swab)

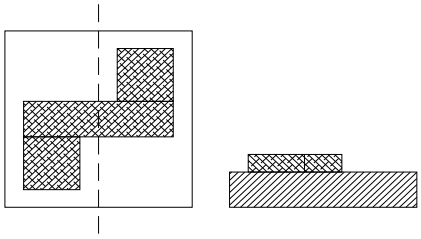

Comments:
C8: bubbles; L01C01, L01C02, L02C01 – short circuit
C9: L03C20, L06C20 – not revealed; L08C09, L09C09 – scratched
C10: L01C19 in short circuit with L01C20

STEP 4: 2nd Exposure - Junction and Bottom contacts definition

Date: 21.03.2013 **Operator**:
Equipment: **SVG Photoresist track, DWL**

Photoresist coating, 1.5 µm PR (Recipe 6/2)
Type: Positive photoresist PFR7790G 2cP *JSR Electronics*
Sample heating for 60s at 110ºC; Cool down for 30s;
Photoresist spinning for 40s at 2500 rpm (1.5 µm photoresist); Baking for 60s at 85ºC

Direct laser write exposure Start:_____ finish: _____ (Total time ~ ____ h)
Masks: `MemRMid4` (inverted) Map: AMSION Die size: X = 10754, Y = 10002

Energy:_____ Focus: ____ Power:_____
Align mark positions:

X=168.5; Y=9948	X=5378.5; Y=9948	X=10700.5; Y=9948
X=168.5; Y=5081	X=5378.5; Y=5081	X=10700.5; Y=5081
X=168.5; Y=54	X=5378.5; Y=54	X=10700.5; Y=54

Photoresist developing, (Recipe 6/2);
Sample heating for 60s at 110ºC (+10s): (C8)
Cool down for 30s
Developing for 60s:

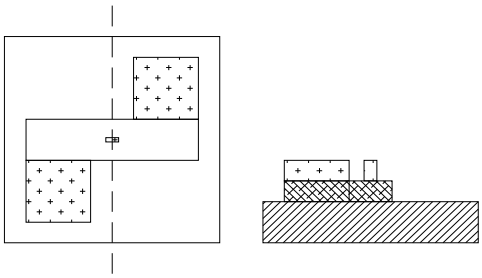

Comments:

Mask in
C9: L03C20, L06C20 – not revealed; L20C13, L05C01, L07C11, L06C11 – defects
C10: because of the bubbles (solution) is difficult to know whether the 1x1 um^2 samples exist or not; in column 11 I have serious doubts that they exist.
C8: L12C08 – damaged; L16C09 – not revealed; again it is difficult to see the 1x1 um^2 samples, for the same reason, and in column 11 they do not seem to exist.

STEP 5: Ion Beam Milling - Junction and Bottom contacts etch, (2nd etch)

Date: 21.03.2013 **Operator**:
Equipment: **Nordiko 3000**

Conditions
Batch: junction_etch
wafer #1:
Base Pressure (Torr): _____
Etch time: 300s (calibration sample transparent: 400 Å depth)

Etch rate:
Etch **pan 60º (____s) + pan 30º (____s)** (Process Steps)
P_{dep} ~ _____ Torr; Target # _____

Assist Gun	Power [W_{RF}]	V+ [V]	I+ [mA]	V- [V]	I- [ma]	Ar Flux [sccm]
Set Values						
Read	55	487.5	30,3	-193.3	(1.7)	07-09-13

Neutralizer	Voltage [V]	Current [ma]	Gas (Ar) [sccm]
Set Values	-		
Read 60			
Read 30			

Substrate	Rotation [%]	Pan [deg]
Set Values		
Read	40	70

Note:
C9: 588/727 Å (perfilometer)
C10: cracked when taking off the duct tape
C8: 516 Å (perfilometer)

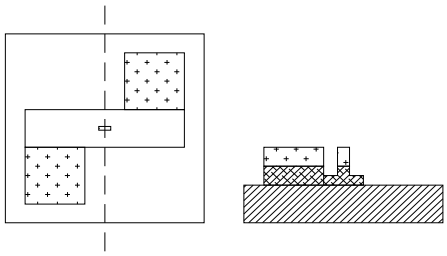

Comments:
Sensor dimensions: (40 of each)
Squares:1*1 um
Squares:2*2 um
Squares:3*3 um
Squares:4*4 um
Squares:5*5 um
Squares:6*6 um
Squares:7*7 um
Squares:8*8 um
Squares:9*9 um
Squares:10*10 um

STEP 6: Protective Layer Deposition – Al_2O_3 Deposition

Date: 22.03.2013 **Operator**:
Equipment: **UHV2**
RF Sputtering deposition (PVD)
B. P.: $17.3x10^{-4}$ Torr

Material	P [W_{RF}]	Pdep [Torr]	Ar [sccm]	Thickness	R [A/min]	T [min]
Al_2O_3	200	2.3 mTorr	45	**600 A**	13,2	45'

Observations:
Calibration sample: 604 Å, 594 Å, 479 Å

Comments:

STEP 7: Al_2O_3 Lift-Off

Date: 22/25.03.2013 **Operator**:
Start: Finished:
Equipment: Wet bench in gray area
Total time in Acetone: 2h(+2h); 2 days clean in between Ultrasonic Time: 2h(+2h) - (except C8)

Stripping
Ultrasounds
Rinse with IPA + DI water + dry N_2

Cleaning
IPA rinse; DI water rinse; Dry with N2 gun

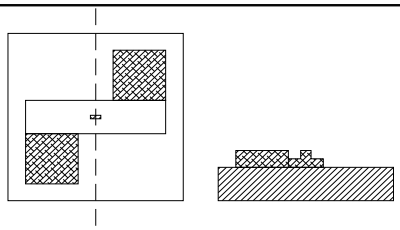

Comments:
Some samples were lost, principally the smaller ones.
C11: lacks revelation – many leads from the first to columns disappeared.

STEP 8: 3rd Exposure – Top Contacts definition

Date: 26.03.2013 **Operator**:
Equipment: **SVG Photoresist track, DWL**

Photoresist coating, 1.5 µm PR (Recipe 6/2)
Type: Positive photoresist PFR7790G 2cP *JSR Electronics*
Sample heating for 60s at 110ºC; Cool down for 30s;
Photoresist spinning for 40s at 2500 rpm (1.5 µm photoresist); Baking for 60s at 85ºC

Direct laser write exposure Start:_____ finish: _____ (Total time ~ ____ h)
Masks: `MemRTop4` (non-inverted) Map: AMSION Die size: X = 10754, Y = 10002

Energy:_____ Focus: ____ Power:_____
Align mark positions:

X=168.5; Y=9948	X=5378.5; Y=9948	X=10700.5; Y=9948
X=168.5; Y=5081	X=5378.5; Y=5081	X=10700.5; Y=5081
X=168.5; Y=54	X=5378.5; Y=54	X=10700.5; Y=54

Photoresist developing, (Recipe 6/2);
Sample heating for 30s at 110ºC
Cool down for 30s+5s
Developing for 60s+5s+30:

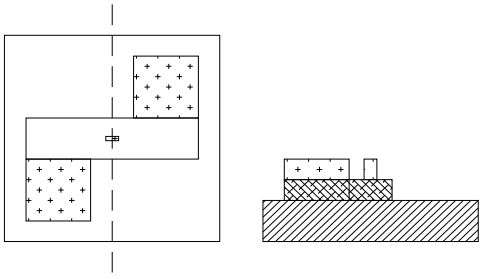

Comments:

Mask in
Some have visible resist on top from the previous lift off (sample not white on top)
C10: smaller samples were gone, the others are fine
C8: well revelead
C9: L19-18(left) – gradation marks from previous processes; few 1x1 um^2 samples, more in the upper half of column 11.

STEP 9: Al 3000Å and TiW(N_2) 300 Å Deposition

Date: 26.03.2013 **Operator**:
Equipment: **Nordiko 3600**

Conditions
170 W/ 171 mA/ V1 = 1200 V/ V2 = -275 V/ V3 = -50 V/ 4sccm Xe/ 30 rpm
Assit gun with V2 = -100 V

Observations:
Receip: 2# Al_metalization_2: 3x1000" Al; 2xcooldown 200"

Comments:

STEP 10: Al Lift-Off

Date: 26.03.2013 **Operator**:
Start: Finished:
Equipment: Wet bench in gray area
Total time in Acetone: overnight Ultrasonic Time: 2h30
(mechanical cleaning with swab on 27.03.2013)

Stripping
Ultrasounds
Rinse with IPA + DI water + dry N_2
Cleaning
IPA rinse; DI water rinse; Dry with N2 gun

Comments:
top Ru/Ag/Ag_2S reacts with remover

```
MemRBot4- bottom contact
MemRMid4- tunnel junction
MemRTop4- top contact
```

Die dimensions:

X = 10754, Y = 10002

Alignment marks:

Sensor dimensions: (40 of each)
Squares:1*1 um
Squares:2*2 um
Squares:3*3 um
Squares:4*4 um
Squares:5*5 um
Squares:6*6 um
Squares:7*7 um
Squares:8*8 um
Squares:9*9 um
Squares:10*10 um